[11C]MODAG 005 – a novel PET tracer targeting alpha-synuclein aggregates in the brain

Ran Sing Saw
Eberhard Karls University Tuebingen, Department of Preclinical Imaging and Radiopharmacy
Sabrina Buss
Eberhard Karls University Tuebingen, Department of Preclinical Imaging and Radiopharmacy
Felix Schmidt
MODAG GmbH
Sergey Ryazanov
Max Planck Institute for Multidisciplinary Sciences, Department of NMR-based Structural Biology
Andrei Leonov
Max Planck Institute for Multidisciplinary Sciences, Department of NMR-based Structural Biology
Laura Kuebler
Eberhard Karls University Tuebingen, Department of Preclinical Imaging and Radiopharmacy
Daniel Bleher
Eberhard Karls University Tuebingen, Department of Preclinical Imaging and Radiopharmacy
https://orcid.org/0000-0002-2216-2524
Ioannis Papadopoulos
Eberhard Karls University Tuebingen
Benjamin Roeben
Department of Neurology, Eberhard Karls University Tuebingen, 72076 Tuebingen, Germany
Fabian Schmidt
Werner Siemens Imaging Center, Department of Preclinical Imaging and Radiopharmacy, Eberhard Karls University Tuebingen, 72076 Tuebingen, Germany
Matthias Reimold
Nuclear Medicine and Clinical Molecular Imaging, Department of Radiology, Universityhospital Tuebingen, 72076 Tuebingen, Germany
Federica Bonanno
Eberhard Karls University Tuebingen, Department of Preclinical Imaging and Radiopharmacy
Ann-Kathrin Grotegerd
Eberhard Karls University Tuebingen
Viktoria Ruf
Ludwig Maximilians University, Center for Neuropathology and Prion Research
Bernadette Dahl
Eberhard Karls University Tuebingen

Christine Sandiego
Invicro
Kelly Henry
Invicro
Birgit Fehrenbacher
Eberhard Karls University Tuebingen
Martin Schaller
Eberhard Karls University Tuebingen
Philipp Kahle
Eberhard Karls University Tuebingen
Thomas Gasser
Department of Neurology, Eberhard Karls University Tuebingen, 72076 Tuebingen, Germany
Kathrin Brockmann
Department of Neurology, Eberhard Karls University Tuebingen, 72076 Tuebingen, Germany
Gerald Reischl
Werner Siemens Imaging Center, Department of Preclinical Imaging and Radiopharmacy, Eberhard Karls University Tuebingen, 72076 Tuebingen, Germany
Christian la Fougère
Nuclear Medicine and Clinical Molecular Imaging, Department of Radiology, Universityhospital Tuebingen, 72076 Tuebingen, Germany
Bernd Pichler
University of Tübingen https://orcid.org/0000-0001-6784-5524
Andreas Maurer
Eberhard Karls University Tuebingen https://orcid.org/0000-0003-2412-5361
Christian Griesinger
Max Planck Institute for Multidisciplinary Sciences, Department of NMR-based Structural Biology
Armin Giese
MODAG GmbH
Kristina Herfert
kristina.herfert@med.uni-tuebingen.de

Eberhard Karls University Tuebingen https://orcid.org/0000-0003-0231-7717

Article

Keywords:

Posted Date: March 21st, 2024

DOI: https://doi.org/10.21203/rs.3.rs-2189800/v1

Additional Declarations: Yes there is potential Competing Interest. A patent has been filed (PCT/EP2020/082778). Armin Giese, Felix Schmidt, Andrei Leonov and Sergey Ryazanov are employed by MODAG GmbH, which retains ownership of MODAG-005, Armin Giese and Christian Griesinger are shareholders of MODAG GmbH.

[^{11}C]MODAG-005 – a novel PET tracer targeting alpha-synuclein aggregates in the brain

Ran Sing Saw[1&], Sabrina Haas[1&], Felix Schmidt[2&], Sergey Ryazanov[3,2&], Andrei Leonov[3,2&], Laura Kuebler[1], Daniel Bleher[1], Ioannis Papadopoulos[1], Benjamin Roeben[4,7,8], Fabian Schmidt[1,5], Matthias Reimold[5], Federica Bonanno[1], Ann-Kathrin Grotegerd[1], Viktoria C. Ruf[6], Bernadette Dahl[7,8,9], Christine M. Sandiego[10], Kelly E. Henry[10], Birgit Fehrenbacher[11], Martin Schaller[11], Philipp J. Kahle[7,8], Thomas Gasser[4,7], Kathrin Brockmann[4,7,8], Gerald Reischl[1,12], Christian la Fougère[5,12], Bernd J. Pichler[1,12], Andreas Maurer[1,12], Christian Griesinger[3,13*], Armin Giese[2*], Kristina Herfert[1*]

[1]Werner Siemens Imaging Center, Department of Preclinical Imaging and Radiopharmacy, Eberhard Karls University Tuebingen, 72076 Tuebingen, Germany
[2]MODAG GmbH, 55234 Wendelsheim, Germany
[3]Department of NMR-based Structural Biology, Max Planck Institute for Multidisciplinary Sciences, 37077 Goettingen, Germany
[4] Department of Neurology, Eberhard Karls University Tuebingen, 72076 Tuebingen, Germany
[5] Nuclear Medicine and Clinical Molecular Imaging, Department of Radiology, Universityhospital Tuebingen, 72076 Tuebingen, Germany
[6] Ludwig Maximilians University, Center for Neuropathology and Prion Research, 81377 Munich, Germany
[7]Hertie Institute for Clinical Brain Research, Department of Neurodegenerative Diseases, Eberhard Karls University Tuebingen, 72076 Tuebingen, Germany
[8]German Center for Neurodegenerative Diseases, 72076 Tuebingen, Germany
[9]Graduate School of Cellular and Molecular Neuroscience, Eberhard Karls University Tuebingen, 72076 Tuebingen, Germany
[10]Invicro, LLC, 119 4th Avenue, Needham, MA 02494, United States of America
[11]Department of Dermatology, Eberhard Karls University Tuebingen, 72076 Tuebingen, Germany
[12]Cluster of Excellence iFIT (EXC 2180) "Image-Guided and Functionally Instructed Tumor Therapies", Eberhard Karls University Tuebingen, 72076 Tuebingen, Germany
[13]Cluster of Excellence “Multiscale Bioimaging: From Molecular Machines to Networks of Excitable Cells” (MBExC), University of Goettingen, 37075 Goettingen, Germany

[&]These authors contributed equally
*Corresponding authors, kristina.herfert@med.uni-tuebingen.de; giese@modag.net; cigr@mpinat.mpg.de

Synucleinopathies are neurodegenerative diseases characterized by the presence of brain inclusions containing the pathologically aggregated protein α-synuclein (αSYN). The development of a positron emission tomography tracer to detect aggregates of misfolded αSYN would revolutionize early diagnosis, disease monitoring and the evaluation of therapeutic efficacy. Here we present the development and preclinical *in vitro* and *in vivo* validation of [^{11}C]MODAG-005. *In vitro* binding experiments demonstrate subnanomolar binding affinity to recombinant αSYN fibrils as well as to αSYN inclusions in human brain tissue. Specific binding in multiple system atrophy (MSA) brain tissue was detected using autoradiography and microautoradiography, and was validated through immunostaining. *In vivo*, [^{11}C]MODAG-005 shows good brain penetration, rapid clearance from brain tissue and low metabolite formation in rodents and non-human primates. In addition, a pronounced binding and a good signal-to-noise ratio were achieved in an αSYN fibril-injected rat model and in an αSYN(A30P) transgenic mouse model in correlation to the pathological load. To validate its value for therapy development, we show target engagement of the drug candidate anle138b in the brain tissues from αSYN(A30P) mouse and MSA as well as *in vivo* in αSYN fibril-injected rats. Finally, our translational approach in a first-in-human patient with clinically established MSA, revealed a marked tracer binding in regions affected by αSYN pathology, particularly in the striatum, where the pattern corresponded with the neurodegeneration shown by dopamine transporter single-photon emission computed tomography.

Synucleinopathies, such as Parkinson’s disease (PD), dementia with Lewy bodies (DLB), and multiple system atrophy (MSA), are neurodegenerative diseases that pose a substantial threat to our aging society. A definitive diagnosis is currently only possible by post-mortem autopsy [1]. Their shared neuropathological hallmark is the presence of misfolded αSYN, which appears with a spatial distribution in the brain that depends on the stage and type of disease. The accumulation of pathological αSYN begins years before the onset of the first (motor) symptoms and would therefore be an excellent biomarker for early detection and monitoring of disease progression [2].

Positron emission tomography (PET) is a non-invasive imaging technology that traces a radioactively labelled molecule designed for a certain biological target *in vivo* [3]. In Alzheimer’s disease (AD), the

development of PET tracers targeting amyloid-β (Aβ) and tau aggregates has greatly advanced our understanding of the time course of aggregation and the regional spread of pathology, revolutionizing the early diagnosis of AD and the assessment of therapeutic effects. Several small molecules targeting αSYN aggregates have been developed over the past decade, with two of them being studied in human subjects [4-7]. Nonetheless, none of these molecules has been translated into clinical applications so far. Compared to Aβ and tau, researchers have encountered considerable challenges in their search for an αSYN PET tracer. This is mainly due to the low availability of the target in tissue, which requires a highly specific molecule with little to no background binding. In addition, misfolded αSYN contains β-sheet secondary structural elements that resemble those of other misfolded peptides and proteins, such as Aβ or tau, which are also found as co-pathologies. Fibril polymorphism is another challenge that further complicates the development of a specific and selective radiotracer due to the multiple conformations of αSYN fibrils, resulting in different morphologies and structures with altered stability and toxicity [8, 9]. Furthermore, since αSYN aggregates are, in contrast to Aβ, located intracellularly, a molecule that penetrates both, the blood–brain barrier and the cell membrane, is required. In addition, the highly complex structure of Lewy bodies, consisting of lipophilic organelles and membrane fragments, presents an additional barrier to αSYN fibril binding [10].

We have developed two prior radiolabeled αSYN-targeting tracers that are structurally derived from the lead compound anle138b (**Extended Data Fig. 1a**) [11]: anle253b (**Extended Data Fig. 1b**) and its successor MODAG-001 (**Extended Data Fig. 1c**) [12, 13]. We have also demonstrated from *in vitro* saturation binding assays that MODAG-001 exhibited high affinity for αSYN fibrils, showed a favorable *in vivo* pharmacokinetic profile, and was able to detect injected recombinant αSYN fibrils in rats [12]. In pigs, (d_3)-[^{11}C]MODAG-001 possessed excellent brain kinetics and a confirmed specific binding in an αSYN pig model *in vivo* [14]. However, in human brain tissue, no to very low binding was observed which is due to its high non-specific binding, lowering the signal-to-noise ratio (SNR) in the target tissue. Nonetheless, its high affinity and promising pharmacokinetic properties formed the basis for the development and testing of next-generation compounds with reduced non-specific binding.

Here, we report the development, preclinical evaluation and first-in-human study of an αSYN PET tracer candidate, [^{11}C]MODAG-005, the de-methylated form of [^{11}C]MODAG-001 (**Extended Data Fig. 1d**).

Results

In vitro fibril binding assays

A competition binding assay using [^{3}H]MODAG-001 as the reference compound was performed to evaluate the binding affinity of MODAG-005 towards αSYN fibrils and revealed a high binding affinity (K_i = 0.4 nM) for MODAG-005 (**Fig. 1a**).

In vitro binding affinity of [^{3}H]MODAG-005 to αSYN fibrils and selectivity over tau and $A\beta_{1-42}$ fibrils were determined using saturation binding assays (n = 3). Specific binding was highest towards αSYN fibrils (B_{max} = 6.6 ± 0.7 pmol/nmol total αSYN) compared to tau (B_{max} = 1.2 ± 0.2 pmol/nmol total tau) and $A\beta_{1-42}$ fibrils (B_{max} = 0.11 ± 0.03 pmol/nmol total $A\beta_{1-42}$) (**Fig. 1b**). [^{3}H]MODAG-005 showed a very high affinity towards αSYN fibrils (K_d = 0.2 ± 0.03 nM) with low non-specific binding (**Fig. 1c**). A 36-fold and >100-fold lower affinity was observed towards tau (K_d = 7.1 ± 0.7 nM) and $A\beta_{1-42}$ (K_d = 21 ± 7.7 nM) fibrils, respectively (**Fig. 1d,e**). MODAG-005 was further tested for off-target binding in a Cerep panel. Specific focus was put on monoamine oxidase B (MAO-B) as this was reported to be overexpressed in several proteinopathies [15]. The IC_{50} value for MAO-B was 0.8 µM.

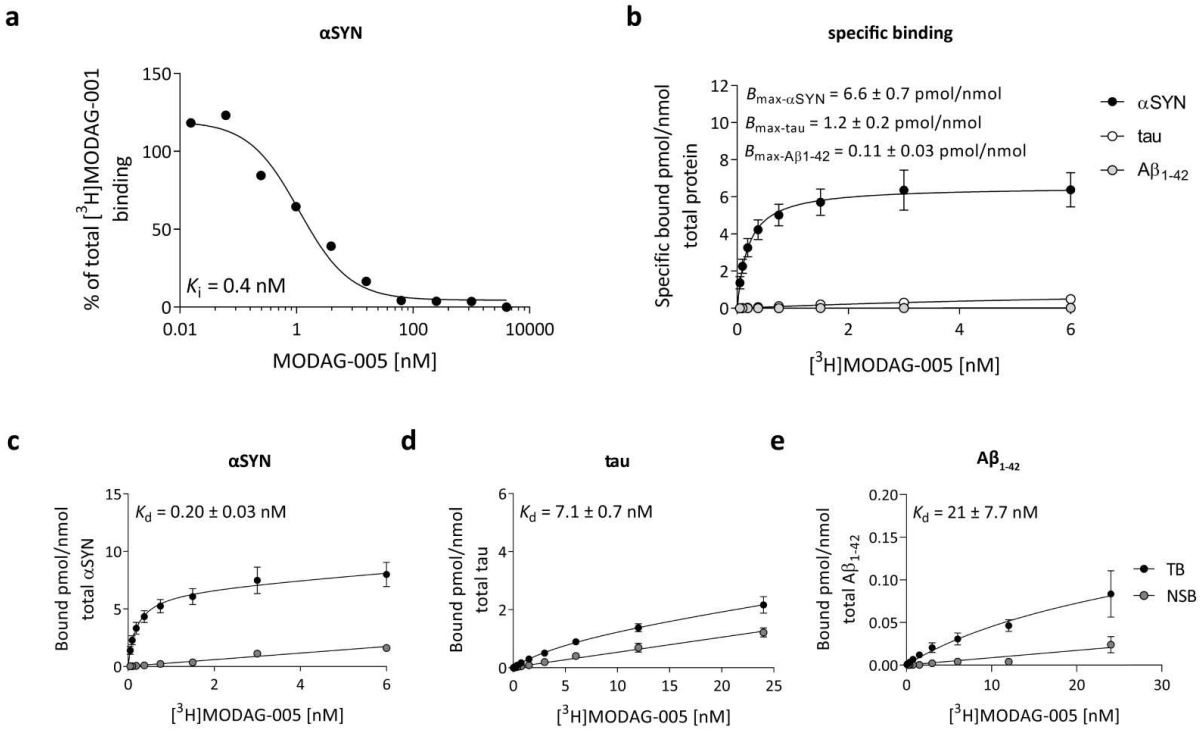

Fig. 1: [^{3}H]MODAG-005 in vitro binding experiments on recombinant human αSYN, tau, and synthetic human Aβ$_{1-42}$ fibrils. a, Competition binding experiment (n = 1, no replicates) with [^{3}H]MODAG-001 showed increased affinity of MODAG-005 to αSYN fibrils. **b**, Saturation binding experiments (n = 3, each in triplicates on the same fibril batch) revealed high binding specificity of [^{3}H]MODAG-005 to αSYN fibrils compared to tau and Aβ$_{1-42}$. **c**, **d**, and **e**, Non-linear regression of TB and NSB revealed a very high affinity towards αSYN fibrils (**c**), moderate affinity towards tau (**d**), and low affinity for Aβ$_{1-42}$ (**e**). Aβ$_{1-42}$, β-amyloid$_{1-42}$; αSYN, α-synuclein; NSB, non-specific binding; SB, specific binding; TB, total binding. The points in **b**, **c**, **d,** and **e** are represented as mean ± s.d..

Binding of [^{3}H]MODAG-005 in human and mouse brain tissue

Fig. 2 and **Extended Data Fig. 2** show [^{3}H]MODAG-005 autoradiography and αSYN pSer129 immunofluorescence microscopy images of the cerebellar cortex of two MSA cases and two control cases. In macroscopic autoradiography, both MSA cases showed a clear specific binding of [^{3}H]MODAG-005 in the white matter of the cerebellum and cerebellar nuclei, which was blocked by an excess of unlabeled MODAG-005 (**Fig. 2a, Extended Data Fig. 2a**). [^{3}H]MODAG-005 binding to αSYN pathology was confirmed by αSYN pSer129 immunofluorescence microscopy. For microscopic verification of [^{3}H]MODAG-005 binding to αSYN aggregates, microautoradiography and subsequent immunofluorescence microscopy were performed on the same brain section of MSA case 1. An extensive presence of silver grains was detected in the cerebellar white matter, indicating the binding of [^{3}H]MODAG-005. These silver grains colocalized with the αSYN pSer129 immunofluorescence signal, with similar distribution and size as αSYN pathology in the white matter. No specific binding, immunofluorescent signal and intense silver grains were observed in the control case (**Fig. 2b, Extended Data Fig. 2b**). Quantitative analysis of MSA and control cases showed increased specific binding in the cerebellar white matter of MSA (3.6 ± 1.4 pmol/mg, n = 2) compared to control (0.6 ± 0.2 pmol/mg, n = 2) (**Fig. 2c**).

To determine the binding affinity on MSA brain tissue sections, saturation binding autoradiography was performed. The Scatchard plot revealed one high- and one low-affinity binding site of [^{3}H]MODAG-005 (**Fig. 2d**). A K_d of 0.25 nM was determined for the high-affinity binding site (**Fig. 2e**), which is consistent with K_d values determined on recombinant human fibrils (**Fig. 1c**). The high-affinity binding site of [^{3}H]MODAG-005 remained after pre-blocking with selegiline (K_d = 1.3 nM) (**Extended Data Fig. 2c** and **d**). To confirm the absence of co-pathology in both MSA cases, pTau and Aβ staining was performed in addition to αSYN pSer129 (**Extended Data Fig. 3**).

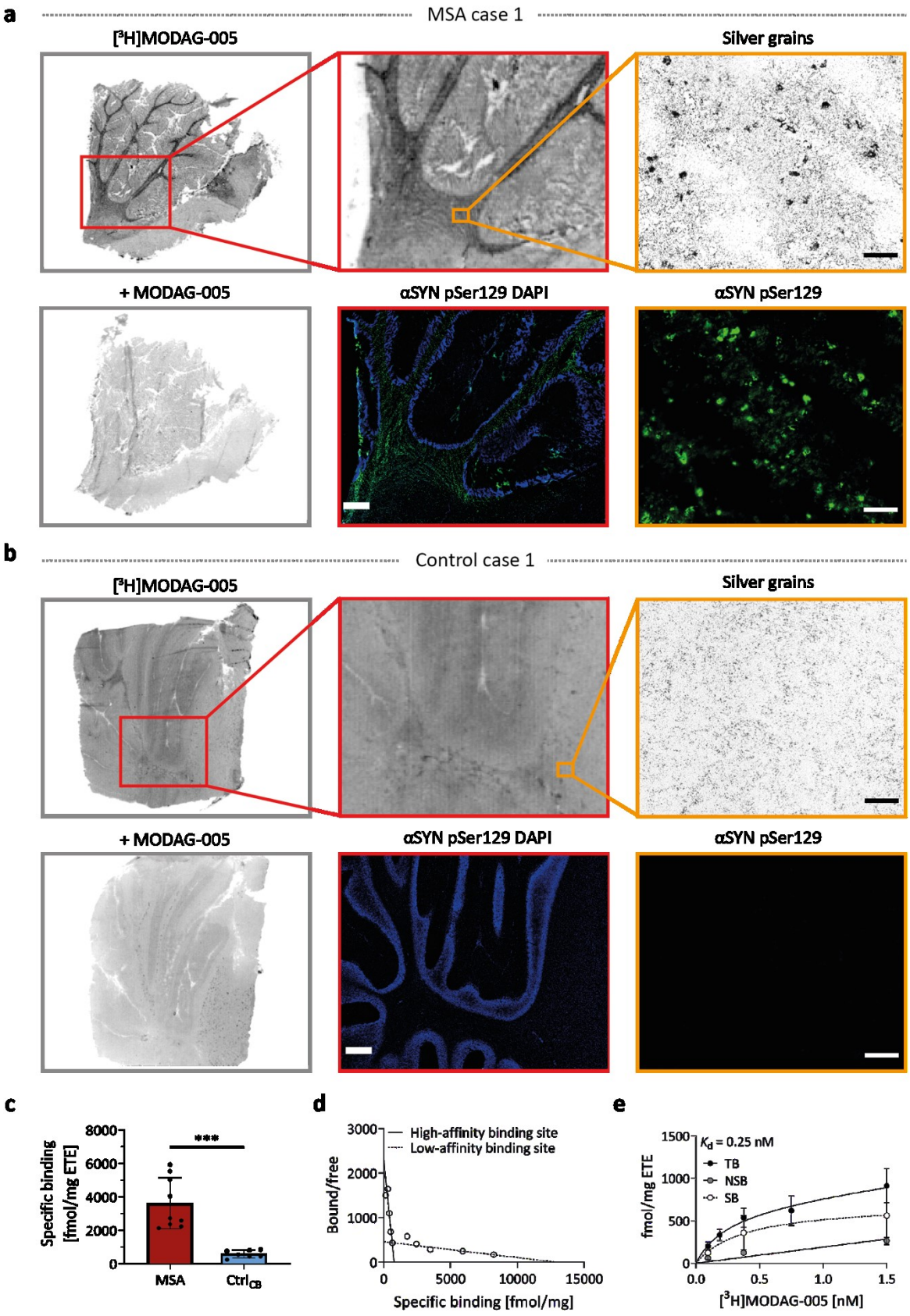

Fig. 2: [^{3}H]MODAG-005 binding to αSYN pathology in MSA brain tissue. a and **b**, Macroscopic autoradiography (3 nM [^{3}H]MODAG-005, with the addition of 3 µM unlabeled MODAG-005 for blocking), microautoradiography (30 nM [^{3}H]MODAG-005) and immunofluorescence microscopy verification of pathology in post-mortem human brain tissues of one exemplary MSA (**a**) and one exemplary healthy control case (**b**). Red boxes show higher magnification and immunofluorescence microscopy images of αSYN pSer129 (green) and DAPI (blue). Scale bars, 1 mm. Microautoradiography (silver grains) and subsequent

immunofluorescence microscopy of αSYN pSer129 (green) are shown in orange boxes. Scale bars, 50 µm. **c**, Quantification shows high specific binding of 3 nM [^{3}H]MODAG-005 in MSA compared to controls (p = 0.0003, n = 2 biological replicates, repeated measurements in each sample). **d** and **e**, Saturation binding autoradiography in MSA brain tissue revealed two binding sites (**d**) with a high affinity binding site (K_d = 0.25 nM) (**e**) in agreement with fibril binding assays (n = 1, repeated measurements in each sample) A K_d value of 31.9 nM was obtained for the low-affinity binding site. αSYN, α-synuclein; DAPI, 4′,6-diamidino-2-phenylindole; ETE, estimated tissue equivalent; MSA, multiple system atrophy; NSB, non-specific binding; SB, specific binding; TB, total binding. Data in **c** and **e** are represented as mean ± s.d.. In **c**, Shapiro-Wilk test indicated normal distribution and a two-way unpaired t-test with Welch's correction was used for the comparisons.

Furthermore, target engagement of the potential therapeutic compound anle138b was examined on human MSA brain tissues (**Fig. 3**). In macroscopic autoradiography, anle138b was able to block [^{3}H]MODAG-005 binding to αSYN pathology in the white matter of MSA tissue (**Fig. 3a**) with a K_i value of 25 nM as revealed by a competition experiment (**Fig. 3b**). Binding specificity of [^{3}H]MODAG-005 was further demonstrated by microautoradiography showing the colocalization of [^{3}H]MODAG-005 signals with αSYN aggregates as well as successful blocking by unlabeled MODAG-005 and anle138b (**Fig. 3c**). Furthermore, both the lack of colocalization between silver grains and MAO-B staining and the inability of selegiline to block tracer signal indicated that the detected signal of [^{3}H]MODAG-005 in MSA tissue was mainly specific and not due to MAO-B binding (**Fig. 3c**).

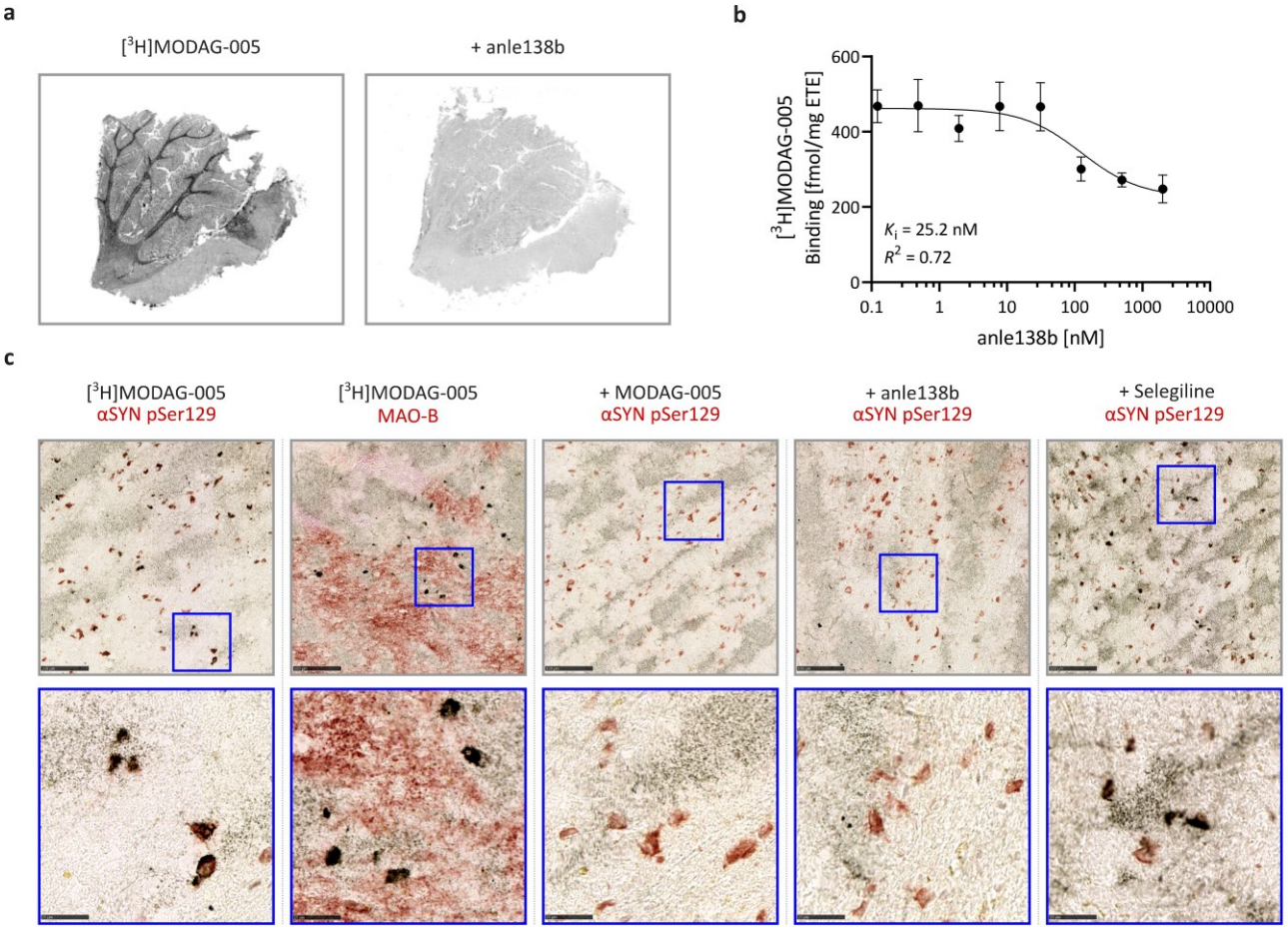

Fig. 3: [^{3}H]MODAG-005 autoradiography and microautoradiography demonstrated binding specificity and target engagement of anle138b in human MSA tissue. a, Autoradiography images show total binding of 3 nM [^{3}H]MODAG-005 (left) and non-specific binding after blocking with 3 µM anle138b (right) in human MSA case 1 brain tissue. **b**, Competition binding with anle138b in human MSA case 1 tissue revealed a K_i value of 25 nM (n = 1, repeated measurements in each sample). The K_i value was calculated based on the K_d value of [^{3}H]MODAG-005 at the high-affinity, low-capacity binding site. **c**, [^{3}H]MODAG-005 microautoradiography (60 nM) (silver grains) with αSYN pSer129 or MAO-B immunohistochemistry (red) shows the colocalization of tracer binding with αSYN pathology, but no colocalization with MAO-B expression. Tracer binding to αSYN aggregates was specific, as indicated by successful blocking (30 µM) with unlabeled MODAG-005 and anle138b, but not with selegiline. Images were taken from the white matter

of MSA case 1 and are shown in grey boxes (scale bar, 100 µm), further magnified images are shown in blue boxes (scale bar, 25 µm). αSYN, α-synuclein; ETE, estimated tissue equivalent; MAO-B, monoamine oxidase B; MSA, multiple system atrophy. Points in **b** are represented by mean ± s.d..

Fig. 4a shows [^{3}H]MODAG-005 autoradiography in the frontal cortex of one PD, one AD, one PSP, and one control case. Increased binding values for the PD (3.8 ± 0.3 pmol/mg), AD (4.0 ± 0.6 pmol/mg) and PSP (1.5 ± 0.8 pmol/mg) case compared to the control case (cortical grey matter: 1.1 ± 0.3 pmol/mg, subcortical white matter 0.1 ± 0.1 pmol/mg) are shown in **Fig. 4b**. Immunofluorescence microscopy images after staining for αSYN pSer129, tau and Aβ are shown in **Extended Data Fig. 4** and **Extended Data Table 1**. To examine the binding of [^{3}H]MODAG-005 to αSYN aggregates in PD, correlation analysis of autoradiography binding and αSYN pSer129 immunofluorescence microscopy was performed. The result indicated a moderate and significant correlation between the two signals (r = 0.56, p < 0.0001) (**Fig. 4c**). Off-target binding in AD brain tissue was further investigated using saturation binding autoradiography, which revealed two binding sites with K_d values of 2 nM and > 500 nM (**Supplementary Item 2**).

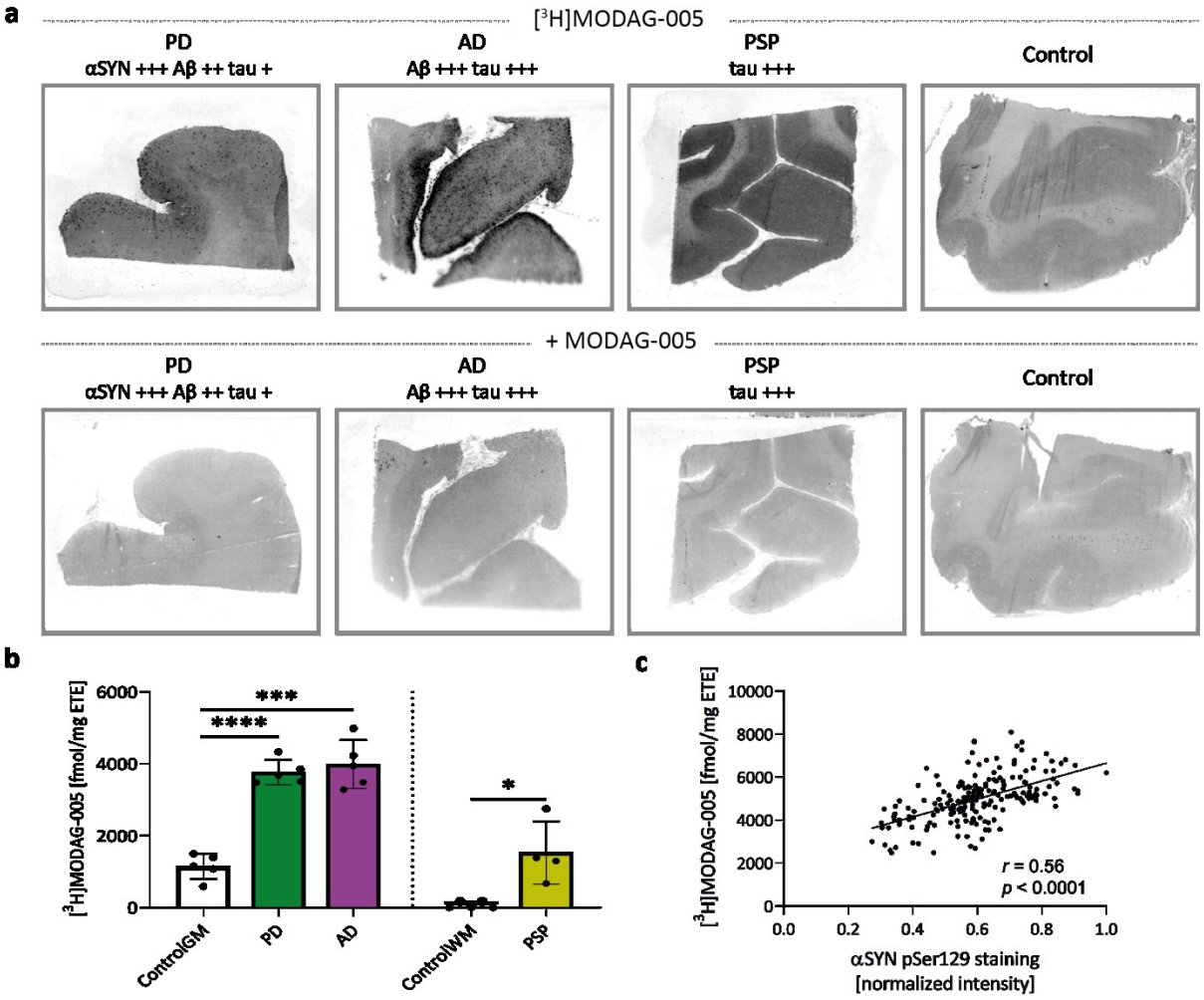

Fig. 4: [^{3}H]MODAG-005 binding in post-mortem human brain tissues of PD, AD and PSP cases. Autoradiography was performed with 3 nM [^{3}H]MODAG-005 and 3 µM unlabeled MODAG-005 for blocking. **a**, Autoradiography images of total binding (upper row) and non-specific binding after blocking with unlabeled MODAG-005 (lower row) in the frontal cortex of PD, AD, PSP, and control brain tissue. **b**, Quantification shows high binding in PD, AD, and PSP brain tissues compared to controls. **c**, In PD tissue, a moderate correlation was observed between [^{3}H]MODAG-005 binding and αSYN pSer129 immunofluorescence microscopy. The number of "+" symbols indicates an increasing degree of pathology. AD, Alzheimer's disease, αSYN, α-synuclein; ETE, estimated tissue equivalent; GM, grey matter; PD, Parkinson's disease; PSP, progressive supranuclear palsy; WM, white matter. Data in **b** are represented as mean ± s.d.. Data in **b** and **c** are from repeated measurements in each sample (n = 1). In **b**, Shapiro-Wilk test indicated normal distribution, Brown-Forsythe and Welch ANOVA with Dunnett's T3 multiple comparisons were used to compare ControlGM with PD and AD, and a two-way unpaired t-test with Welch's correction was used to

compare ControlWM with PSP. In **c**, the αSYN pSer129 staining intensity was normalized by the maximum intensity.

The binding of [^{3}H]MODAG-005 as well as target engagement of anle138b was further determined on brain tissue sections of the αSYN(A30P) mouse model of PD and age-matched wild-type mice (**Fig. 5a**). Quantitative analysis in brain regions (**Supplementary Item 3**) with positive αSYN pSer129 immunofluorescence signals revealed higher binding in the midbrain (2.0 ± 0.7 pmol/mg vs. 0.3 ± 0.5 pmol/mg), brainstem (1.2 ± 0.4 pmol/mg vs. 0.2 ± 0.5 pmol/mg), zona incerta (1.9 ± 0.5 pmol/mg vs. 0.2 ± 0.4 pmol/mg) and cerebellum (0.5 ± 0.7 pmol/mg vs. -0.1 ± 0.4 pmol/mg) compared to the age-matched control (**Fig. 5b**). In the cortex, no differences were observed (0.7 ± 0.5 pmol/mg vs. 0.6 ± 0.4 pmol/mg).

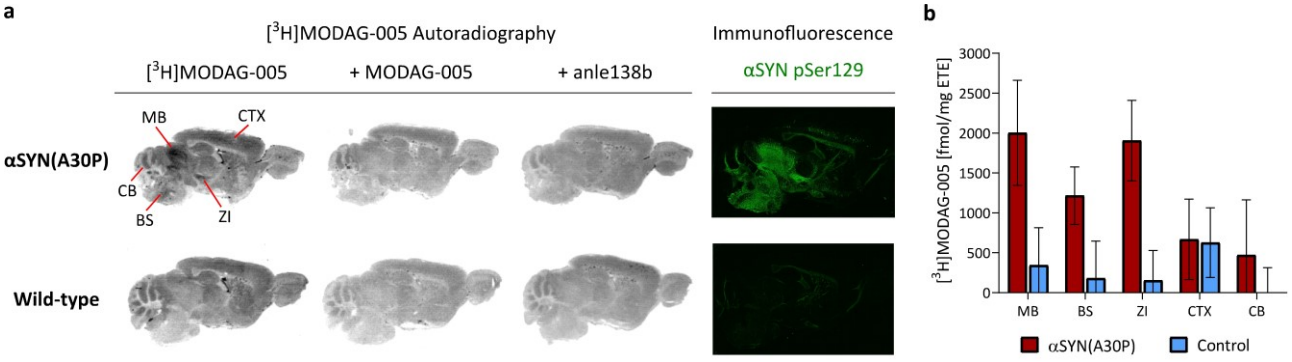

Fig. 5: [^{3}H]MODAG-005 binding and anle138b target engagement in the αSYN(A30P) mouse model of PD. Autoradiography was performed with 3 nM [^{3}H]MODAG-005 and 3 µM unlabeled MODAG-005 or anle138b for blocking. **a**, [^{3}H]MODAG-005 total binding, self-blocking and anle138b blocking in brain sections of an αSYN(A30P) mouse and an age-matched wild-type mouse is shown. Distribution of αSYN pathology was confirmed via immunofluorescence staining of αSYN pSer129 (green). **b**, Quantification (total binding minus self-blocking) revealed increased tracer binding in regions with αSYN pathology compared to the corresponding brain regions of age-matched wild-type mouse. αSYN, α-synuclein; BS, brainstem; CB, cerebellum; CTX, cortex; ETE, estimated tissue equivalent; MB, midbrain; ZI, *zona incerta.* Data in **b** are presented as mean ± s.d., obtained from repeated measurements in technical replicates (3 for [^{3}H]MODAG-005 and 2 [^{3}H]MODAG-005 + MODAG-005 for NSB). No statistical test was performed.

These findings led us to label MODAG-005 with carbon-11 to study its *in vivo* pharmacokinetics and radio-metabolite formation. The results of the radiolabeling are provided in the **Supplementary Item 4**.

Pharmacokinetic and metabolic profile in rodents

After the successful synthesis of [^{11}C]MODAG-005 (**Fig. 6a**), dynamic PET scans were performed in mice and rats. **Fig. 6b,c** shows whole body sagittal [^{11}C]MODAG-005 PET/MRI images and time-activity curves (TACs) of selected brain regions and peripheral organs from one exemplary mouse over time. Rapid brain uptake with a peak standardized uptake value (SUV) of 1.9 and a fast wash-out from the brain with clearance half-lives ranging from 5.5 to 6.7 minutes in the selected brain regions was observed. TACs of selected brain regions from one rat after injection of [^{11}C]MODAG-005 revealed SUVs up to 3.2 (**Extended Data Fig. 5a**) and a fast wash-out from the brain with clearance half-lives ranging from 3.1 to 6.1 minutes. [^{11}C]MODAG-005 radio-metabolite formation in the brain and plasma of mice (n = 3 per time-point) (**Fig. 6d**) and rats (n = 1 per time-point) (**Extended Data Fig. 5b**) was determined at 5 and 15 minutes after tracer injection. Quantitative analysis revealed one metabolite in the brain with 96 ± 1.1% and 79 ± 3.1% of the parent compound remaining at 5 minutes and 15 minutes after tracer injection, respectively. Analysis of the rats revealed one metabolite in the brain with 91% and 64% of the parent compound remaining at 5 minutes and 15 minutes after injection, respectively. **Extended Data Table 2** summarizes quantitative values of all radio-metabolites obtained in plasma and brain.

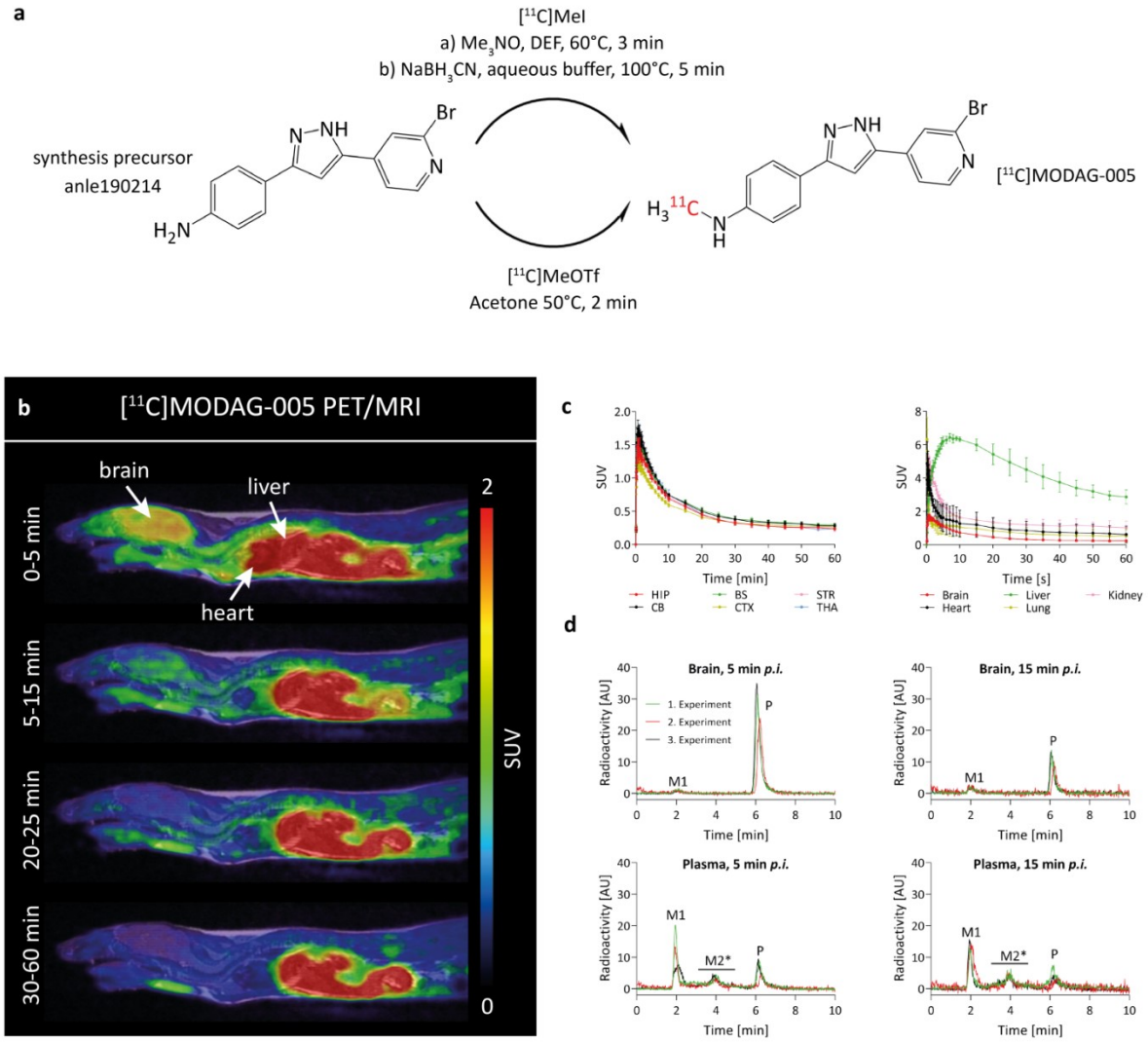

Fig. 6: Radiolabeling and *in vivo* characterization of [^{11}C]MODAG-005 in healthy mice. a, Radiolabeling of [^{11}C]MODAG-005 was performed by reductive methylation or direct methylation and resulted in radiochemical yields of 12.0 ± 2.2% or 11.8 ± 2.7% and molar activities of 49.2 ± 11.2 GBq/µmol or 209 ± 44 GBq/µmol (end of synthesis), respectively. **b**,**c left**, Exemplary whole body [^{11}C]MODAG-005 PET/MR images over time (n = 1) and mean TACs (n = 3) show high brain uptake (max. SUV = 1.9) and a fast washout from the brain in mice. **c right**, *In vivo* biodistribution in different organs is shown. **d**, Radio-metabolite analysis (n = 3) revealed one metabolite present in the brain with 96 ± 1% and 79 ± 3% of the parent compound remaining at 5 and 15 minutes post tracer injection, respectively. In the blood plasma, additional metabolites M2* were detected. AU, arbitrary units; BS, brainstem; CB, cerebellum; CTX, cortex; HIP, hippocampus; MRI, magnetic resonance imaging; M1, metabolite 1; M2*, metabolite 2*; P, parent compound; PET, positron emission tomography; p.i., post injection; STR, striatum; SUV, standardized uptake value; TACs, time-activity curves; THA, thalamus. The points in **c** are represented as mean ± s.d..

Verification of binding to injected αSYN fibrils

To investigate whether we can detect [^{11}C]MODAG-005 binding to αSYN fibrils *in vivo*, rats were injected with αSYN fibrils into the right striatum; sham injection with buffer was performed on the contralateral side. Four days post injection, [^{11}C]MODAG-005 PET images were acquired, and brains were surgically extracted to confirm αSYN fibril location using thioflavin S staining and [^{3}H]MODAG-005 autoradiography. In addition, [^{11}C]MODAG-005 PET images were acquired from non-injected wild-type animals to exclude the possible contribution of blood–brain barrier leakage to increased tracer uptake because of intracranial injections. **7a** shows exemplary brain [^{11}C]MODAG-005 PET images of one αSYN fibril-injected rat and one non-injected rat summed up from 2.5 to 60 minutes. Increased tracer accumulation is seen at the αSYN fibril injection site. αSYN fibril location is confirmed by thioflavin S staining and *in vitro* [^{3}H]MODAG-005 autoradiography. Elevated tracer retention in the fibril-injected striatum compared to the sham-injected striatum was detected in TACs as well as in time-SUVR curves calculated using the cerebellum as the reference region (**Extended Data Fig. 6a, Fig. 7b**). Average SUVR showed increased tracer binding in the fibril-injected compared to the

sham-injected striatum of αSYN fibril-injected rats (1.18 ± 0.059 vs. 0.967 ± 0.041, $p = 0.0003$), but no difference between the right and left striatum of non-injected rats (0.97 ± 0.043 vs. 0.99 ± 0.071, $p = 0.542$) (**Fig. 7c**). Furthermore, **Extended Data Fig. 7** shows the improved SNR by a direct comparison of d_3-[^{11}C]MODAG-001 and [^{11}C]MODAG-005 PET images of αSYN fibril-injected rats at four days post injection.

To investigate and exclude that the elevated tracer binding was due to an inflammatory process and/or possible MAO-B binding, we performed immunohistochemistry of glial fibrillary acidic protein (GFAP) as a surrogate marker of astrogliosis and MAO-B. While stronger signals were observed in the fibril-injected striatum compared to the sham-injected striatum for both staining, the strongest astrogliosis and MAO-B expression were found in the cortex in both brain hemispheres (**Extended Data Fig. 6b**). In comparison, images from *in vivo* [^{11}C]MODAG-005 PET and *in vitro* [^{3}H]MODAG-005 autoradiography displayed a different pattern compared to the findings from GFAP and MAO-B immunohistochemistry, with no strong tracer binding in the areas surrounding the injection trajectory, where an inflammatory response and MAO-B upregulation were the highest (**Fig. 7a**).

In addition, PET data was further analyzed using different approaches to define the volumes of interest and an alternative reference region. **Extended Data Fig. 6c** shows the PET analysis performed using volumes of interest based on isocontour automatic detection set to 70% to include only the region with expected fibril localization. TACs and time-SUVR curves, as well as average SUVR, collectively illustrated a higher tracer retention in the fibril-injected striatum compared to the non-injected striatum (average SUVR = 1.66 ± 0.137 vs. 0.98 ± 0.163, $p = 0.0021$). Using the left, sham-injected striatum as the reference region, elevated tracer retention was detected in the fibril-injected striatum compared to the non-injected striatum (average SUVR = 1.24 ± 0.018 vs. 0.99 ± 0.054, $p = 0.003$) (**Fig. 7d**).

To determine the binding specificity of [^{11}C]MODAG-005 and to study the *in vivo* target engagement of anle138b in fibril-injected rats, two PET scans consisting of a baseline measurement with vehicle injection and a blocking measurement with anle138b administration were performed between three to four days after fibril injection in rats. Five minutes before tracer injection, vehicle or anle138b (1 mg/kg dose in the vehicle) was administered intravenously as a single bolus. Administration of anle138b successfully blocked tracer binding (average SUVR = 1.24 ± 0.018 at baseline vs. 0.99 ± 0.054 at blocking, $p = 0.028$, sham-injected striatum as reference region) (**Fig. 7e**). Similar results were obtained using the cerebellum as the reference region (**Extended Data Fig. 6d** and **e**): Average SUVR indicated a successful blocking by anle138b, which reduced tracer binding from 1.23 ± 0.01 to 1.15 ± 0.02 ($p = 0.04$) in the fibril-injected striatum (**Extended Data Fig. 6e**). In contrast, anle138b increased tracer signal in the sham-injected striatum from 0.96 ± 0.04 to 1.08 ± 0.03 ($p = 0.02$) (**Extended Data Fig. 6e**).

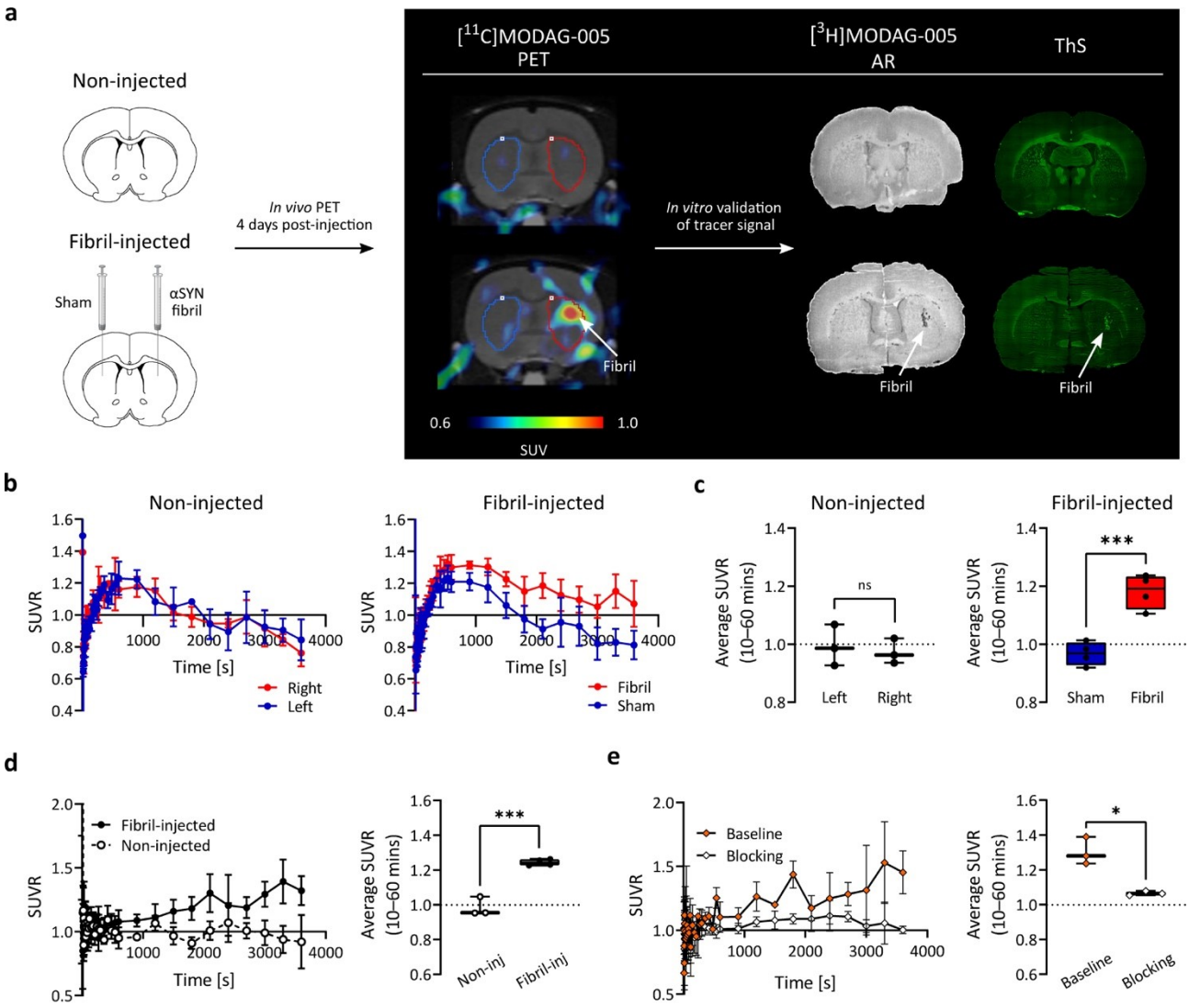

Fig. 7: *In vivo* characterization of [^{11}C]MODAG-005 in fibril-injected rats. a, Brain [^{11}C]MODAG-005 PET images (sum of 2.5 to 60 min) of one exemplary non-injected and one unilateral αSYN-fibril injected rat scanned four days post injection are shown. Increased tracer accumulation was observed in the fibril-injected right striatum, but not in the vehicle-injected left striatum and non-injected rat. The location of αSYN fibrils was confirmed by [^{3}H]MODAG-005 autoradiography and thioflavin S staining. **b**, **c**, PET analysis using the cerebellum as reference region for SUVR calculation. **b**, SUVR values over time did not differ in the striatum of non-injected rats, whereas they were increased in the right, αSYN fibril-injected striatum compared to the left, sham-injected striatum. **c**, A comparison of the average SUVR between the right and left striatum of non-injected rats (0.97 ± 0.043 vs. 0.99 ± 0.071, p = 0.542) and between the fibril- and sham-injected striatum of αSYN fibril-injected rats (1.18 ± 0.059 vs. 0.97 ± 0.041, p = 0.0003) is shown. **d**, **e**, PET analysis using the sham-injected, left striatum as the reference region for SUVR calculation. **d**, Time-SUVR curves and average SUVR showed increased tracer retention in the fibril-injected striatum compared to non-injected striatum (average SUVR = 1.24 ± 0.018 vs. 0.99 ± 0.054, p = 0.003). **e**, Time-SUVR curves and average SUVR showed a decreased tracer retention in the fibril-injected striatum with anle138b blocking compared to baseline (average SUVR = 1.24 ± 0.018 vs. 0.99 ± 0.054, p = 0.028). AR, autoradiography; αSYN, α-synuclein; fibril-inj, fibril-injected; non-inj, non-injected; PET, positron emission tomography; SUV, standardized uptake value; SUVR, standardized uptake value ratio; ThS, thioflavin S. Data are presented as mean ± s.d.. Box plots extend from the 25th to 75th percentiles with the median indicated in the middle of the box and the minimum to maximum values shown by the whiskers. An unpaired two-tailed t-test was used for comparisons. In **b** and **c**, n = 3 for non-injected rats and n = 4 for fibril-injected rats. In **d** and **e**, fibril-injected rats underwent both baseline and blocking scans (n = 3).

Evaluation of [^{11}C]MODAG-005 in αSYN(A30P) transgenic mouse model of PD

To study the ability of [^{11}C]MODAG-005 to detect intracellular αSYN aggregates *in vivo*, we performed PET imaging in the αSYN(A30P) transgenic mouse model of PD and age-matched wild-type mice (**Fig. 8**,

Extended Data Fig. 8). The presence and distribution of αSYN pathology were verified by immunohistochemistry of αSYN pSer129, which revealed the strongest pathology in the brainstem, midbrain and hypothalamic areas in αSYN(A30P) mice (**Fig. 8a**, **Extended Data Fig. 8a**). Immunohistochemistry further revealed a heterogeneity in the pathology load among αSYN(A30P) mice. **Extended Data Fig. 8b** shows in the x-axis the percentage of positive αSYN pSer129 immunohistochemistry in the brainstem of αSYN(A30P) mice with a large interindividual variation, which ranged from 0.2% to 12.4%. αSYN(A30P) mice with less than 1% positive staining signal were excluded from the main PET analysis shown in **Fig. 8b** and **Extended Data Fig. 8c**.

[^{11}C]MODAG-005 binding in individual brain regions was consistent with the αSYN pathology distribution. Elevated time-SUVR curves and average SUVR values reflected increased tracer retention in αSYN(A30P) compared to wild-type mice in the brainstem (1.16 ± 0.06 vs. 1.07 ± 0.07, $p = 0.004$), midbrain (0.94 ± 0.04 vs. 0.88 ± 0.06, $p = 0.03$) and hypothalamus (1.28 ± 0.13 vs. 1.15 ± 0.10, $p = 0.008$) (**Fig. 8b**). A moderate positive correlation was indicated between αSYN pSer129 immunohistochemistry and [^{11}C]MODAG-005 PET binding in the brainstem ($r = 0.47$, $p = 0.043$) (**Extended Data Fig. 8b**). On the other hand, no enhanced tracer binding was detected in the amygdala ($p = 0.20$), striatum ($p = 0.08$), thalamus ($p = 0.10$) and cerebellum ($p = 0.31$) (**Extended Data Fig. 8c**), where lower αSYN pathology load was detected (**Extended Data Fig. 8a**).

To investigate and exclude that the elevated tracer binding was due to potential off-target binding to MAO-B, we further performed immunohistochemistry and a qualitative scoring of MAO-B expression in the brainstem, midbrain, and hypothalamus (score 0–3, where 0 indicates no staining and 3 indicates relatively abundant staining) (**Extended Data Fig. 9**). Example of MAO-B immunohistochemistry images with their respective given score, as well as a larger magnification of the staining are displayed in **Extended Data Fig. 9a** and **b**, respectively. Our analysis revealed comparable average scores of MAO-B staining, ranging from 0 to 2 for all groups of αSYN(A30P) and wild-type mice, indicating no difference in MAO-B expression between the animal groups.

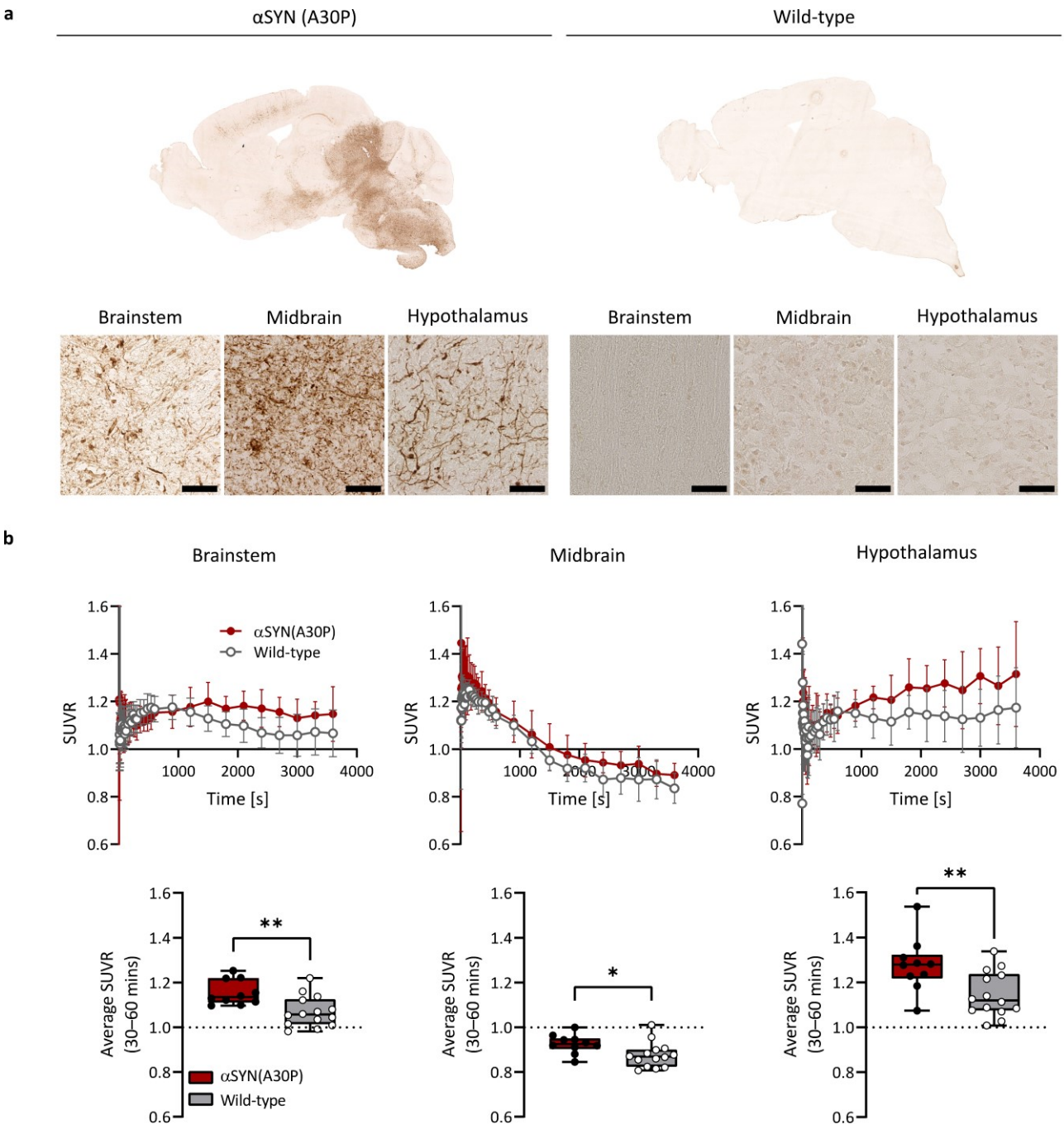

Fig. 8: *In vivo* characterization of [^{11}C]MODAG-005 in the αSYN(A30P) transgenic mouse model. a, Immunohistochemistry of αSYN pS129 in αSYN(A30P) and wild-type mouse brain. Exemplary whole-brain images as well as magnified images in brain regions with high pathology load such as the brainstem, midbrain, and hypothalamus are shown. Scale bar, 50 µm. **b**, [^{11}C]MODAG-005 PET time-SUVR curves and average SUVR comparison between αSYN(A30P) mice (n = 10) and wild-type mice (n = 14) are shown. SUVR values were calculated using the cortex as the reference region and averaged from 30 to 60 minutes. Time-SUVR curves showed higher tracer retention in αSYN(A30P) mice. Comparing the average SUVR values, increased tracer binding was detected in αSYN(A30P) mice compared to wild-type mice in the brainstem (1.16 ± 0.06 vs. 1.07 ± 0.07, p = 0.004), midbrain (0.94 ± 0.04 vs. 0.88 ± 0.06, p = 0.03) and hypothalamus (1.28 ± 0.13 vs. 1.15 ± 0.10, p = 0.008). Data points in time-SUVR curves are presented as mean ± s.d.. Box plots extend from the 25th to 75th percentiles with the median indicated in the middle of the box and the minimum to maximum values shown by the whiskers. Shapiro-Wilk test was used to test for a normal distribution. An unpaired two-tailed t-test was performed to compare the average SUVR values between both animal groups. αSYN, α-synuclein; SUVR, standardized uptake value ratio.

Characterization of [^{11}C]MODAG-005 in non-human primate brain

To evaluate the tracer characteristics in wild-type non-human primates (NHPs) without αSYN pathology, we performed dynamic *in vivo* PET imaging and plasma radio-metabolite analysis in two cynomolgus monkeys (NHP 1 and NHP 2). **Fig. 9a,b** and **Extended Data Fig. 10a,b** show a macaque MRI image as well as baseline and competition [^{11}C]MODAG-005 PET images of the brain summed up from 0–10 minutes and 90–120 minutes with respective TACs of selected brain regions over time. For visualization, images and TACs in units of kBq/cm^3 were converted to SUV in units of g/mL. At baseline, rapid brain uptake with a peak SUV of 3.7 and 6.1 for NHP 1 and NHP 2, respectively, and a fast wash-out from the brain with a clearance half-life of approximately 12 minutes (one-phase decay model from the peak) was identified (**Fig. 9b** and **Extended Data Fig. 10b**). After blocking with MODAG-005, we saw similar pharmacokinetic profile with peak SUVs of 4.7 and 4.2 for NHP 1 and NHP 2, respectively, and a clearance half-life of approximately 16 minutes. Total volume of distribution (V_T) and K_1 were estimated using a 2-tissue compartment model [16]. V_T is the activity ratio between tissue and plasma at equilibrium, and K_1 is the rate of tracer delivery from plasma to brain tissue. In the whole brain, V_T and K_1 were estimated to be 6.89 ± 1.58 mL/cm^3 and 0.49 ± 0.12 mL/cm^3/min, respectively. V_T at baseline and competition were compared, revealing little differences in NHP 1 (5.11–6.15 mL/cm^3 vs. 4.87–6.07 mL/cm^3) and some degree of lowered V_T in NHP 2 (7.76–9.81 mL/cm^3 vs. 5.03–6.58 mL/cm^3) (**Fig. 9c** and **Extended Data Fig. 10c**). On the other hand, little changes between K_1 at baseline and competition were noted for both NHP 1 (0.30–0.45 mL/cm^3/min vs. 0.36–0.63 mL/cm^3/min) and NHP 2 (0.49–0.89 mL/cm^3/min vs. 0.51–0.78 mL/cm^3/min) (**Fig. 9d** and **Extended Data Fig. 10d**).

[^{11}C]MODAG-005 radio-metabolite formation in the plasma of NHP 1 and NHP 2 was determined 5, 15, 30, 45, and 60 minutes after tracer injection (**Fig. 9e** and **Extended Data Table 3**). Quantitative analysis revealed two metabolites in the plasma with 74 ± 1.3%, 29 ± 0.3%, 18 ± 1.7%, 14 ± 1.0%, and 8.6 ± 1.0% of the parent compound remaining at 5, 15, 30, 45, and 60 minutes after tracer injection, respectively. Heart rate (BPM), body temperature, expired CO_2, respiration/min, pulse O_2%, % anesthetic gas, and oxygen (L/min) throughout the scans are summarized in **Supplementary Item 5**.

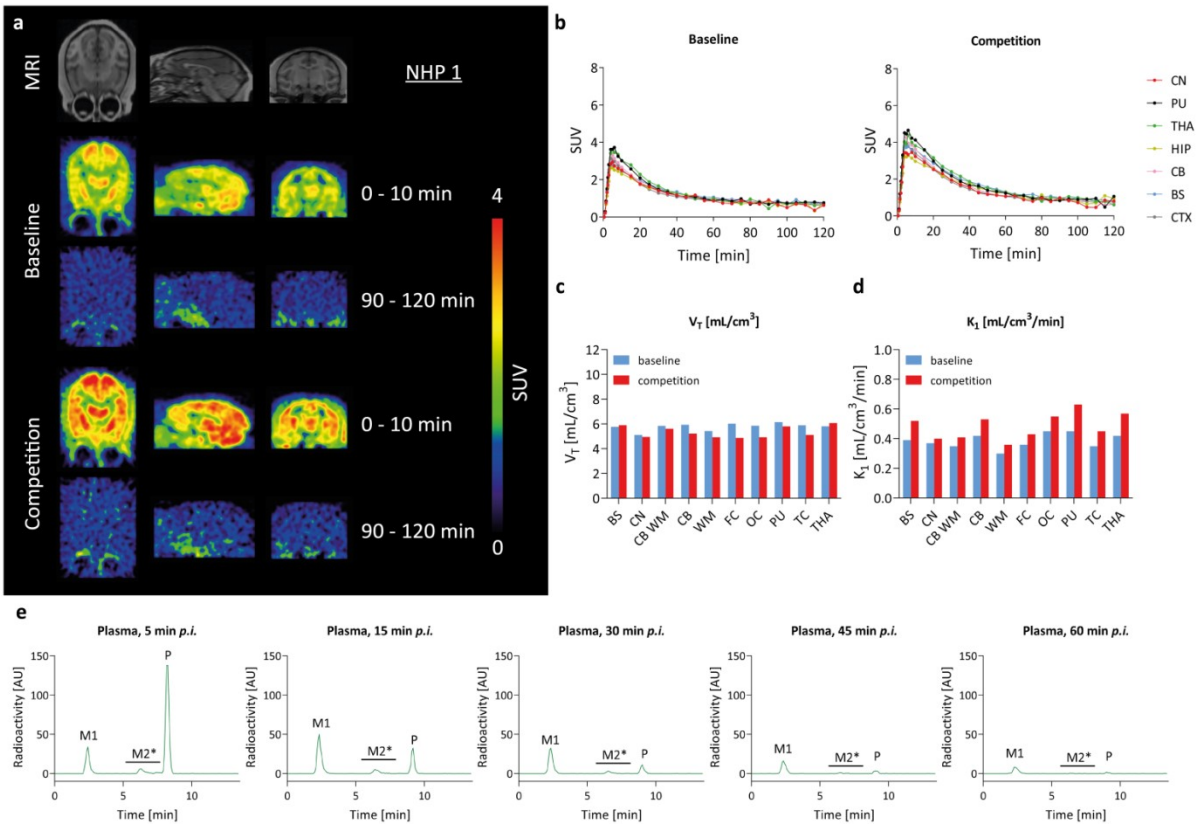

Fig. 9: *In vivo* characterization of [^{11}C]MODAG-005 in non-human primates (NHPs). a, Transversal, sagittal, and coronal (left to right) MRI of one exemplary cynomolgus monkey brain and [^{11}C]MODAG-005 PET images at baseline and after pre-injection of unlabeled MODAG-005 (sum of frame 0 to 10 and 90 to 120 minutes). **b**, TACs of different brain regions show high brain uptake with peak SUVs of 3.7 (baseline) and 4.7 (competition) followed by a fast clearance from the brain. **c**,**d**, Volume of distribution (V_T) and K_1 values estimated from a 2-tissue-compartment model at baseline and after competition with MODAG-005. **e**, Plasma radio-metabolites revealed the formation of two metabolites, with 70%, 24%, 16%, 12%, and 8% of

the parent compound remaining at 5, 15, 30, 45, and 60 minutes post tracer injection, respectively. For results in NHP2, see **Extended Data Fig. 10).**
AU, arbitrary units; BS, brainstem; CB, cerebellum; CB WM, cerebellar white matter; CN, caudate nucleus; CTX, cortex; WM, white matter; FC, frontal cortex; HIP, hippocampus; MRI, magnetic resonance imaging; M1, metabolite 1; M2*, metabolite 2*; OC, occipital cortex; P, parent compound; PET, positron emission tomography; p.i., post injection; PU, putamen; STR, striatum; SUV, standardized uptake value; TACs, time-activity curves; TC, temporal cortex; 2-TCM, two tissue compartment model; THA, thalamus.

[^{11}C]MODAG-005 - first in human

Following radiochemical development and preclinical evaluation, the radiochemical synthesis process for [^{11}C]MODAG-005 was transferred to a Good Manufacturing Practice (GMP) environment and further optimized to fulfill the requirements for a human application, in this case following the regulations of the German Medicinal Products Act ("Arzneimittelgesetz" AMG §13(2b)). After full disclosure, a first-in-human translational PET-scan with [^{11}C]MODAG-005 was performed on a high sensitive PET-scanner (Biograph Vision Quadra) in a patient diagnosed with an overlap syndrome of multiple system atrophy – parkinsonian type (MSA-P) and cerebellar type (MSA-C). The patient gave a written informed consent for both performing the PET scan with [^{11}C]MODAG-005 and further data-processing and evaluation. The diagnosis of overlapping MSA-C and MSA-P was based on clinical assessment, diagnostic MRI and Single-Photon-Emission Computed Tomography (SPECT) of the presynaptic dopamine transporter (DAT) with [^{123}I]FP-CIT.

Fig. 10a presents MRI data revealing advanced cerebellar and pontine atrophy including indication of the "Hot Cross Bun" sign, reflecting degeneration of pontocerebellar tracts. In line with these findings, [^{123}I]FP-CIT-SPECT images (**Fig. 10b**) show a strong presynaptic dopaminergic degeneration (reduced DAT availability) in the left and right striatum with a greater reduction on the right side. Notably, elevated [^{11}C]MODAG-005 retention was observed in brain regions anticipated to exhibit αSYN pathology, specifically in the caudate, putamen, thalamus, pons and cerebellar white matter. With respect to the striatum, this retention was slightly higher on the right side, mirroring the lateralization noted in the [^{123}I]FP-CIT-SPECT images. TACs of selected brain regions, including the occipital cortex as reference region due to its expected lack of pathology, are depicted in **Fig. 10c**.

The pharmacokinetic analysis, illustrated in **Fig. 10d,e**, reveals a rapid brain uptake of [^{11}C]MODAG-005 in the brain. The occipital cortex showed a peak SUV of 2.8 and a clearance half-life of 20 min. For comparison, peak SUV was 3.5 and and clearance half life was 10 min in the occipital cortex in the healthy NHP shown in **Fig. 9** and **Supplementary item 8.** In comparison to the MSA patient, no difference in tracer uptake was observed between the striatum and occipital cortex in the NHP as shown in **Fig. 9b,c**.

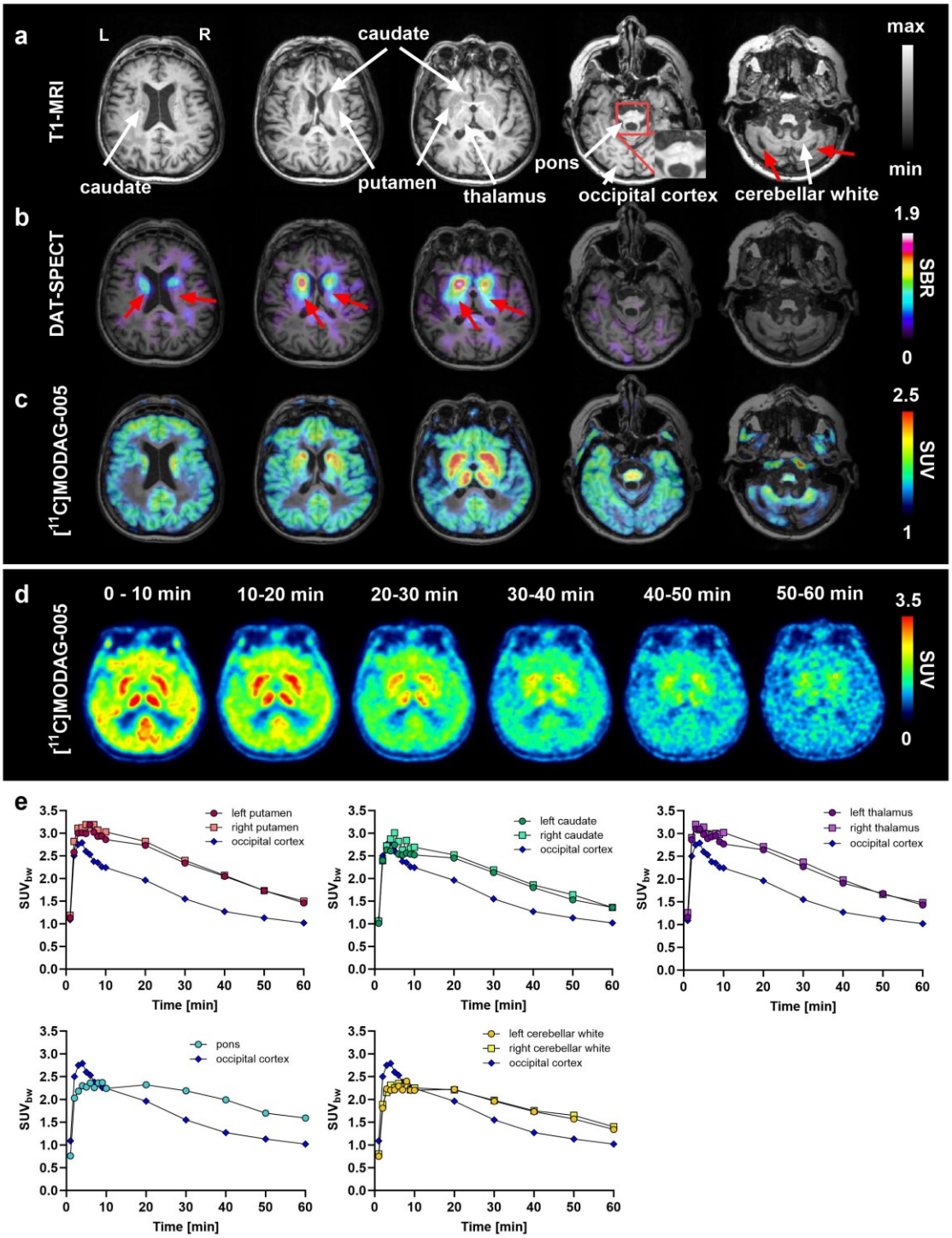

Fig. 10: [^{11}C]MODAG-005 first-in-human PET. a, Transversal MR scans of a patient clinically diagnosed with an overlap syndrome of MSA-P and MSA-C, highlighting advanced cerebellar and pontine atrophy including indication of the “Hot Cross Bun” sign reflecting degeneration of pontocerebellar tracts (indicated by red arrows and zoomed insert). White arrows indicate anatomical regions which show increased [^{11}C]MODAG-005 uptake. **b**, Dopamine transporter (DAT) SPECT images, revealing significant presynaptic dopaminergic degeneration in the bilateral striatum (caudate and putamen) with a more pronounced effect on the right side. **c**, [^{11}C]MODAG-005 PET images (sum of 20-60 min) illustrating elevated binding in the bilateral striatum. Additionally, increased binding is noted in the thalamus, pons and cerebellar white matter – regions associated with expected αSYN pathology. **d**,**e** The pharmacokinetic profile of [^{11}C]MODAG-005 in a representative slice (sum of all frames) and corresponding time-activity curves of selected brain regions, demonstrate rapid brain uptake (peak SUV: 2.8) and moderately fast clearance ($t_{1/2}$ = 20 min) from the occipital cortex, a region anticipated to be free of pathology. Conversely, regions expected to exhibit αSYN pathology show a prolonged tracer retention. MRI, magnetic resonance imaging; PET, positron emission

tomography; SBR, specific binding ratio; SUVbw, standardized uptake value (normalized to body weight); SPECT, single photon emission computer tomography; DAT, dopamine transporter.

Discussion

Pathological αSYN is the key hallmark in several major devastating neurodegenerative diseases, most prominently PD, DLB, and MSA. Its aggregation seems to be the central driver of their pathogenesis and inhibiting this process holds considerable promise as a therapeutic strategy, qualifying it as a main target for potential disease-modifying drugs, such as anle138b (emrusolmin) [11, 17], PD01A [18], BIIB054 [19] or RO7046015 [20].

Several PET radiotracers targeting neurodegeneration and their underlying metabolic processes have been successfully developed [21-23] and offer the possibility of a differential diagnosis late in the disease. However, pathology-specific early diagnosis is needed to modify and/or stop the disease and efficiently slow down its progression by therapy.
In contrast to αSYN aggregates, radiotracers for imaging the neuropathological hallmarks of AD and tauopathies have been developed [24-27]. The clinical assessment of amyloid burden using PET imaging has been playing a key role in the enrolment and outcome measurement of clinical trials to investigate the efficacy of anti-amyloid therapies [28-31].

The development of a non-invasive diagnostic tool for αSYN pathology is crucial and an αSYN PET tracer would be a game changer for basic research, early diagnosis, and therapy development. The emergence of different classes of αSYN ligands in the past decade is an encouraging reflection of the advances in αSYN PET tracer development. Yet, a tracer that combines all the desirable properties is still missing. A common challenge is the lack of detectable tracer binding to αSYN pathology in the human brain, despite their good affinity to αSYN fibrils [12, 32]. A number of recently developed αSYN ligands show promising *in vitro* binding. Yet, *in vivo* brain uptake and kinetics seems to require further optimization [33-35]. For other αSYN ligands, evaluation and data analysis in animal models was not unambiguously conclusive [36, 37]. While a few tracer candidates have been advanced to human studies, off-target binding seems to be an issue and bigger patient cohorts should be investigated for conclusive evaluation of the suitability of the tracer for human diagnosis [7, 38].

Herein, we aimed to develop an αSYN PET tracer, MODAG-005, based on the lead structure anle138b and its derivatives, anle253b and MODAG-001, and to perform a detailed evaluation to characterize its binding profile from *in vitro* with fibrils and brain tissues to *in vivo* in animal models. We demonstrated its high specificity and affinity in a subnanomolar range, which is superior to all respective published values of other tracer candidates published so far [5-7, 39, 40]. Our previous study reported [^{11}C]MODAG-001 as a new potential αSYN PET ligand [12], however, it failed to efficiently detect aggregated αSYN from human brain tissue and showed a high non-specific background binding.

Following the identification of the de-methylated MODAG-001 (MODAG-005) as a brain-penetrating metabolite, our next goal was to enhance the properties of MODAG-001 by removing a major metabolite that confounds kinetic modeling.The *in vitro* affinity of [^{3}H]MODAG-005 towards human αSYN fibrils was found to be improved by three-fold. Comparing [^{3}H]MODAG-005 to its predecessor, [^{3}H]MODAG-001, the selectivity of [^{3}H]MODAG-005 for αSYN over tau fibrils increased. Furthermore, it is >100-fold more selective for αSYN over $A\beta_{1-42}$ fibrils. MODAG-005 was further tested for potential off-target binding using the Cerep diversity panel comprising 71 target proteins (receptors, transporters, channels, enzymes) and a customized kinase panel comprising 159 different kinases. A special focus was put on MAO-B binding, as *in silico* analysis of different tau tracer candidates showed that they bind to the same region as the MAO-B inhibitor selegiline, i.e., the substrate entry site. Thus, IC_{50} values obtained in the Cerep assay should provide valid information on binding to the relevant site. The determined IC_{50} of 0.8 µM is considered to be of little relevance for MODAG-005 *in vivo* PET.

We further demonstrate the binding of [^{3}H]MODAG-005 to αSYN pathology of human brains. The ability of MODAG-005 to bind to αSYN inclusions in brain tissues of synucleinopathies, particularly with an unprecedented high affinity, indicates its potential for imaging the misfolded αSYN in human brains. Moreover, successful blocking and competition with anle138b in brain tissue from human MSA and the αSYN(A30P) mouse model provide evidence for the target engagement of anle138b as MODAG-005 competes for the same binding site. Using [^{3}H]MODAG-005, we confirmed the binding of anle138b to aggregated αSYN in human MSA brain tissue, determining a K_i of 25 nM.

Despite the presence of co-pathology in PD brain tissue, we detected a remarkable binding which correlates with αSYN immunofluorescence. A previous competition assay between MODAG-001 and SIL26 suggested that the two ligands likely target the same binding site [12, 41]. The latter was reported to bind to PD homogenates with a K_i value of 33.5 nM, pointing to the presence of a binding site for MODAG-001/MODAG-005 in αSYN aggregates from the PD brain. Further validation of tracer binding in PD brain tissue will be pursued in future work.

In line with the fibril binding assay, [^{3}H]MODAG-005 autoradiography also revealed non-selective binding in PD, AD, and PSP tissues. By nature, amyloid fibrils, such as Aβ, tau, and αSYN, share structural similarity between binding pockets as they form unique beta-sheet secondary structures [42]. Small molecule compounds might therefore bind all three amyloids to a certain extent. Even when a clean off-target profile was indicated *in vitro*, the tracer signal may still be confounded by disease-related off-target binding *in vivo*. For example, [^{18}F]ACI-12589 showed binding in other neurodegenerative diseases with an increased cortical retention in AD subjects correlated to areas of tau tracer [^{18}F]RO948 uptake despite the lack tau binding *in vitro* [7]. Hence, it is important to note that off-target binding remains a challenge for all current tracer candidates that have undergone thorough validation studies and thus merits further improvement in future development.

Our *in vitro* results showed a high concordance between binding to the type of recombinant αSYN fibrils used by us (K_d = 0.20 ± 0.03 nM) and αSYN aggregates in human brain tissue (K_d = 0.25 nM). This is particularly important for future screenings on recombinant fibrils, as screenings on tissue homogenates are challenging and the tissue is precious. A high-affinity binding site for [^{3}H]MODAG-005 remained in MSA tissue after selegiline blocking, indicating the specificity of αSYN binding.

Based on the promising *in vitro* binding in human tissues, MODAG-005 was labeled with carbon-11 for *in vivo* evaluation. *In vivo* [^{11}C]MODAG-005 PET studies in healthy mice and rats showed sufficient brain uptake and rapid clearance, which fulfils the pharmacokinetic requirements of a central nervous system PET tracer. Since [^{11}C]MODAG-005 is the de-methylated form of [^{11}C]MODAG-001, we were able to reduce the number of detectable radio-metabolites in the brain from two to one. While the presence of radiometabolite in the brain could confound kinetic modelling, analysis in human subjects will be required to confirm the metabolic profile of [^{11}C]MODAG-005, as lower species, such as rodents, have faster and more extensive metabolism compared to humans [43].

In the fibril injection model, [^{11}C]MODAG-005 was able to detect injected αSYN fibrils *in vivo.* Although αSYN fibrils are mainly located extracellularly, it is a suitable model to study and compare the binding kinetics of tracers to αSYN aggregates under physiological conditions. Despite the increase in astrogliosis and MAO-B expression which were associated with intracranial surgery and the injected fibril, immunohistochemistry revealed a different pattern of GFAP and MAO-B upregulation in the brain compared to *in vivo* [^{11}C]MODAG-005 PET images and *in vitro* [^{3}H]MODAG-005 autoradiography, thereby excluding the possibility that increased tracer signal was due to MAO-B off-target binding. A successful reduction of tracer binding after anle138b blocking indicated the binding specificity of [^{11}C]MODAG-005 and provided evidence for the *in vivo* target engagement of anle138b.

We demonstrated that [^{11}C]MODAG-005 has an improved image contrast compared to MODAG-001, showing a better signal in the fibril-injected striatum and lower background binding in the uninjected striatum. The removal of the methyl group increases the hydrophilicity of the molecule, thereby reducing its non-specific binding to the myelin/lipid-containing white matter brain structures [44] and, consequently increases the SNR of the tracer in tissue. The *in vivo* pharmacokinetics study of [^{11}C]MODAG-005 showed a good tracer uptake into the brain, demonstrating that the small increase in the hydrophilicity of MODAG-005 while improving the SNR in PET imaging, did not impair its ability to penetrate the blood-brain barrier. Taken together, one of the biggest downsides of MODAG-001 – its non-specific *in vivo* background binding – was addressed and improved with MODAG-005.

Furthermore, [^{11}C]MODAG-005 was investigated in *vivo* in the αSYN(A30P) mouse model of PD. This mouse model has intracellular Lewy body-like aggregates of the transgenic human αSYN with the A30P mutation that causes familial PD [45]. Compared to age-matched wild-type mice, enhanced binding of [^{11}C]MODAG-005 in αSYN(A30P) mice was demonstrated in brain regions with strong αSYN pathology, validated by immunohistochemistry and in line with literature reports [45, 46]. This increase in tracer binding was not caused by MAO-B, since its expression was similar in these brain regions regardless of pathology load. On the other hand, in brain regions with less αSYN pathology, [^{11}C]MODAG-005 could not distinguish between the two groups. Nevertheless, a correlation between the amounts of αSYN pSer129 and the degree

of [^{11}C]MODAG-005 binding in the brainstem indicated the tracer's potential to differentiate between individuals with different pathology loads and suggested the successful use of [^{11}C]MODAG-005 as an αSYN PET tracer for *in vivo* application.

In view of the promising results above, we proceeded to investigate the potential translation of [^{11}C]MODAG-005 to larger species by performing *in vivo* studies in healthy NHPs. Our tracer showed a rapid brain uptake and clearance, with peak SUVs of 3.7–6.1, which is high compared to tracers for Aβ ([^{11}C]PIB <2) [47] or tau (Tauvid ~2.3) [48] in their preclinical evaluation in NHPs. V_T values in NHP 1 were not reduced after competition with MODAG-005 pointing to low to no off-target binding in the healthy brains. For NHP 2, V_T was lower in competition compared to baseline values, which may be attributed to an increased heart rate observed during tracer injection at baseline affecting tracer uptake or low signal to noise in parent fraction measurements after 30 minutes for the baseline scan that may affect the arterial input function. A retest study would be helpful to assess test-retest reliability of V_T to determine if the change in V_T is meaningful. With a mean K_1 of 0.49 ± 0.12 mL/cm^3/min, the tracer exhibited excellent extraction from the plasma to the tissue. Competition increased K_1 values, which might be a result of blocked plasma protein binding, resulting in higher concentrations of [^{11}C]MODAG-005 in the brain. Radio-metabolite analysis indicates a similar metabolism in rodents and NHPs.

The first-in-human translational use of [^{11}C]MODAG-005 was performed for clinical and diagnostic investigation of a patient with the diagnosis of clinically established MSA according to the Movement Disorders Society clinical diagnostic criteria for MSA [49]. Clinically, the patient presented with an overlap syndrome of MSA-P and MSA-C. Absence of Aβ copathology was determined by analysis of cerebrospinal fluid (CSF) profiles of $A\beta_{1\_42}$, total-Tau and p181-Tau levels which were in the normal range. [^{11}C]MODAG-005 demonstrated rapid brain uptake achieving peak SUVs of 2.2-3.2, aligning with the aforementioned Aβ and tau tracers [47, 48]. Notably the tracers elimination half-life in the occipital coretex was prolonged compared to NHP, suggesting increased non-specific binding in human brain tissue. Despite this, [^{11}C]MODAG-005 exhibited pronounced retention in regions anticipated to exhibit αSYN pathology, particularly within the caudate putamen, corroborating significantly reduced DAT availability observed in earlier SPECT imaging.

The lateralization of tracer uptake, more pronounced on the right, mirrored the asymmetrical DAT loss observed in DAT imaging. Additionally, tracer accumulation in the cerebellum and pons was observed, aligning with the expected neuropathology and supporting the diagnostic accuracy of [^{11}C]MODAG-005. While the absence of a healthy control limits direct comparison, the comparison with NHP data, which showed no increased tracer uptake in analogous regions, provides indirect evidence of the tracer's specificity.

In the present study, we report a detailed *in vitro* and *in vivo* evaluation of MODAG-005. We obtained a clear macroscopic and microscopic evidence of tracer binding to glial cytoplasmic inclusions in MSA brain tissue with an unprecedented binding affinity, which is superior compared to affinities reported for other αSYN tracer candidates. Feasibility for *in vivo* imaging was consolidated through the successful identification of regions with high pathology in the αSYN(A30P) transgenic mouse model. We also presented evidence for a specific binding of MODAG-005 to αSYN pathology which was independent of MAO-B, as validated in brain tissue sections of human MSA, fibril-injected rat, and αSYN(A30P) mice. This investigation is crucial and has been discussed in αSYN tracer development [7], yet often not studied [40, 50]. We further applied MODAG-005 to confirm the target engagement of the potential therapeutic agent anle138b, both *in vitro* and *in vivo*. On the other hand, limitations of this work are the lack of an unambiguous tracer binding to LBs and LNs in human PD tissue due to the presence of concomitant pathology, as well as off-target binding to Aβ and tau aggregates. Both of these merits in-depth investigation or improvement in future work.

In conclusion, our results collectively indicate that [^{11}C]MODAG-005 is a promising tracer candidate for *in vivo* imaging of MSA patients. Its superior subnanomolar binding affinity to αSYN aggregates may provide an advantage over other tracers with lower binding. Furthermore, the present study demonstrated the potential application of [^{11}C]MODAG-005 to validate *in vivo* drug target engagement of novel αSYN-targeting therapeutic agents in clinical trials.

Methods

A competition screening of a compound library against [^{3}H]MODAG-001 was performed, which identified MODAG-005 to be a high-affinity binder to recombinant αSYN fibrils. After tritiation, the binding affinity and selectivity of [^{3}H]MODAG-005 were determined using saturation binding assays against αSYN, tau, and Aβ fibrils, and in animal and human brain slices. After ^{11}C-labeling, *in vivo* characterization of [^{11}C]MODAG-005

was performed in rodents and NHPs using PET imaging and metabolite analysis. Furthermore, *in vivo* binding was determined in rats intrastriatally injected with αSYN fibrils.

Precursor and standard synthesis of MODAG-005
The synthesis of MODAG-005 and its precursor for radiosynthesis is described in **Supplementary Item 6**. The calculated logP (clogP) and topological polar surface area (tPSA, [Å^2]) values shown in **Extended Data Fig. 1** were calculated by the Molinspiration property engine (v2021.10).

MODAG-005 tritiation
MODAG-005 was tritiated (RC Tritec AG, Teufen Switzerland), dissolved in EtOH, and stored at -80°C until further usage. The A_m was 2.96 GBq/µmol, and its radiochemical purity was > 98%, as determined via high-performance liquid chromatography (HPLC).

Fibril binding experiments
Expression, purification, and generation of sonicated human recombinant wild-type αSYN were performed using previously established protocols [12, 13]. Carrier-free recombinant human 4-repeat-tau (4R-tau) (Tau-441/2N4R-Tau), hereinafter referred as tau, was purchased lyophilized from Bio-Techne GmbH (Wiesbaden, Germany), and reconstituted in 50 mM Tris-buffer, pH 7.0. Fibrillation was induced by heparin under constant agitation and the generated fibrils were sonicated, as described previously [12, 51]. Sonicated $Aβ_{1-42}$ fibril batch 1 production was adapted from [41] and performed as described previously [12]. Sonicated $Aβ_{1-42}$ fibril batch 2 was produced analogous to batch 1 but with 96 hours incubation time and validated using thioflavin T (ThT) fluorescence assay, negative staining transmission electron microscopy, as described previously [12], as well as [^{3}H]Pittsburg compound B (PiB) saturation binding assay (**Supplementary Item 1**). Prior to binding experiments, the optimal concentration for the respective fibril type was determined by performing a concentration determination assay to prevent ligand depletion, as described in [12].

Binding experiments were conducted as previously described [12]. Briefly, for competition binding experiments, a fixed concentration of αSYN (15 nM) fibrils was incubated with 1 nM [^{3}H]MODAG-001 in low-binding plates (96-well micro test plate, ratiolab GmbH, Dreieich, Germany). Competition was induced by adding ten concentrations of a 1:4 serial dilution of unlabeled MODAG-005 (4 µM–0.02 nM) in 30 mM Tris-HCl, 10% ethanol, 0.05% Tween20, pH 7.4 (in the following referred to as EtOH-Tween buffer) in a total volume of 200 µL/well.

For [^{3}H]MODAG-005 saturation binding assays, a fixed concentration of αSYN (15 nM), tau (250 nM) or $Aβ_{1-42}$ (1 µM) fibrils was incubated with with decreasing concentrations of [^{3}H]MODAG-005 (6 nM/24 nM–0.05 nM) in EtOH-Tween buffer in a total volume of 200 µL/well. Co-incubation with 400 nM unlabeled MODAG-005 was used to determine non-specific binding of the radiotracer. For [^{3}H]PiB saturation binding assay, $Aβ_{1-42}$ (2.5 µM) fibrils was incubated with decreasing concentrations of [^{3}H]PiB (32 nM–0.06 nM) in 50 mM Tris-HCl, 10% EtOH, 0.1% BSA, 0.025% NaN_3, pH 7.4, in a total volume of 200 µL/well. Co-incubation with 400 nM unlabeled PiB was used to determine non-specific binding of the radiotracer.

Incubation at 45 rpm for two hours at 37°C was performed on a shaker (MaxQ™ 6000, orbit diameter 1.9 cm, Thermo Fisher Scientific Inc., Marietta, OH, USA). The plate was covered by removable sealing tape (PerkinElmer, Waltham, MA, USA) to prevent evaporation of the tracer solutions. A filtermat harvester (PerkinElmer, Waltham, MA, USA) was used to filter bound radioligands onto a glass fibre filtermat B (PerkinElmer, Waltham, MA, USA), which was pre-incubated with 5 mg/mL polyethyleneimine (Sigma Aldrich Chemie GmbH, Taufkirchen, Germany) only for αSYN and $Aβ_{1-42}$ fibrils. After harvesting, the filtermat was dried in the microwave, and melt-on scintillator sheets (MeltiLex™ B/HS, PerkinElmer, Waltham, MA, USA) were molten into the filtermat. After solidification at room temperature, the filter was placed in a MicroBeta sample bag (PerkinElmer, Waltham, MA, USA) and measured using the Wallac MicroBeta® TriLux liquid scintillation counter (PerkinElmer, Waltham, MA, USA). Radioactivity converted to bound pmol fibril per added nmol of total fibril was plotted against increasing [^{3}H]MODAG-005 or [^{3}H]PiB concentrations in nM. Data points were fitted using nonlinear regression analysis in GraphPad Prism (GraphPad Software, Inc., Version 7.03, La Jolla (CA), USA). Saturation binding assays were performed in triplicates and repeated in three independent experiments.

Off-target binding
A Cerep diversity panel and a customized kinase panel assay were performed by Eurofins Cerep in France with a specific focus on MAO-B binding. The compound enzyme inhibition effect was calculated as a % inhibition of control enzyme activity. Competition binding assays were performed using increasing concentrations of MODAG-005 and IC_{50} values were determined by non-linear regression analysis of the competition curves.

Human and mouse brain tissue
Post-mortem human brain tissue samples were provided as 10 µm sections by the Neurobiobank Muenchen (NBM, Munich, Germany), where cases were collected on the basis of written informed consent according to the guidelines of the ethics committee of the Ludwig-Maximilians-University Munich, Germany (# 345-13). **Extended Data Table 1** provides a summary of the subjects and controls from which brain tissues were obtained. For PD case, the disease duration was approximately 25–26 years, with the first symptoms appearing in the patient's mid-60s as tremor of the left hand. The disease progressed with exhibition of akinetic-rigid syndrome and camptocormia over time, as well as mild cognitive impairment ten years ante mortem, and dementia (PD with dementia) five years ante mortem. The use of human tissue samples for this study was approved by the ethics committee of the Faculty of Medicine at the University of Tuebingen (Ethics approval number: 813/2018BO2).

In addition, 20 µm sagittal mouse brain sections for autoradiography experiments were obtained from an αSYN(A30P) (B6.Cg-Tg(THY1-SNCA A30P)1734Sud/J) and an age-matched wild-type (male, 72 weeks) mouse. All tissues were stored at -80°C until further use.

***In vitro* (micro)autoradiography**
Post-mortem human and mouse brain sections were used for autoradiographic evaluation of [^{3}H]MODAG-005. After defrosting, the brain sections were pre-incubated in 30 mM Tris-HCl, 0.1% BSA, pH 7.4 (in the following referred to as BSA buffer) for 25 minutes at room temperature. For total binding, the sections were incubated in 3 nM [^{3}H]MODAG-005. For blocking, adjacent sections were co-incubated with 3 µM unlabeled MODAG-005 or anle138b.

For saturation binding experiments, brain sections were incubated with decreasing concentrations of [^{3}H]MODAG-005 (48 to 0.1 nM for MSA; 96 to 0.2 nM for AD). To determine non-specific binding, adjacent sections (for tracer concentrations 96 nM, 48 nM, 24 nM, and thereafter every second section) were co-incubated with 3 µM unlabeled MODAG-005. In the selegiline pre-blocking saturation experiment, MSA tissue sections were pre-incubated in 3 µM selegiline for one hour at room temperature and washed (three times for ten minutes) before tracer incubation (96 to 0.38 nM, with non-specific binding determined at every tracer concentration). For competition binding experiments, 1 nM [^{3}H]MODAG-005 was incubated with decreasing concentrations of unlabeled anle138b (2 µM to 0.03 nM).

In all experiments, brain sections were incubated at room temperature for one hour with subsequent washing in ice-cold BSA buffer (three times for ten minutes) followed by dipping for three seconds in ice-cold deionized water. The dried sections were then exposed to a phosphor imaging plate (BAS-IP TR2025, Fuji Imaging Plate, VWR, Denmark) with a tritium standard (ART-123 and ART-123A; American Radiolabelled Chemicals, St. Louis, MO, USA) for seven days and scanned in a phosphor imager (BAS 5000, FUJIFILM Life Science, Stamford, CT, USA).

For data quantification, ImageJ software (US National Institutes of Health, Bethesda, MD, USA) was used. Images were converted to 32-bit and the square math function for increasing the grey value range was applied. Regions of interest (ROIs) were drawn over the tritium standard to obtain a standard curve. ROIs were placed in the white matter of MSA, progressive supranuclear palsy (PSP), a neurodegenerative tauopathy with a predominance of 4R-tau isoforms [52], and control cases (cerebellum and frontal cortex), and in the grey matter of PD, AD, and control cases (frontal cortex). For the mouse brain sections, ROIs were placed in the midbrain, brainstem, zona incerta, cortex, and cerebellum (**Supplementary Item 3**), which are brain regions of expected αSYN pathology, and cross-validated with pSer129 αSYN immunofluorescence microscopy [45]. Specific binding was calculated by subtracting the non-specific binding from the total binding values. After interpolation from the standard curve, the specific binding values were divided by the A_m of the tracer and converted into fmol/mg.

Statistical analysis was performed using GraphPad Prism (Version 8.4.0). Comparisons were carried out using values obtained from repeated measurements in each sample (ROIs placed at different locations) to capture any difference in pathology and tracer binding across the tissue sections. Welch's t-test was used to compare the specific binding between MSA cases and controls (cerebellum - white matter), as well as PSP and control (frontal cortex – white matter). For comparison of AD and PD with control (frontal cortex – grey matter), Brown-Forsythe and Welch ANOVA with Dunnett's T3 multiple comparisons test was carried out. For the saturation binding experiment in MSA, a Scatchard plot was prepared in GraphPad Prism based on the calculated specific binding. Data points for the high-affinity binding site (0.09–1.5 nM) and the low-affinity binding site (3–48 nM) were determined by visual inspection. Subsequently, non-linear regression (saturation binding: one-site – total and non-specific binding) was performed independently for the two sites to

determine the respective K_d and B_{max} values. The lines in the Scatchard plot were drawn based on these values, where x-intercept = B_{max} and y-intercept = B_{max}/K_d. For the competition experiment with anle138b in MSA, non-linear regression (competitive binding: one-site-fit K_i) was used. For the autoradiography in mouse brain tissues, no statistical test was performed.

For microscopic investigation of tracer binding, microautoradiography was performed in two MSA cases and one control case, which were thawed and fixed in 4.5% paraformaldehyde (PFA, SAV Liquid Production GmbH, Flintsbach am Inn, Germany) for ten minutes at room temperature. Pre-incubation and washing steps were as above. Brain sections were incubated for one hour with 30 or 60 nM [^{3}H]MODAG-005. Adjacent tissue sections were additionally incubated with 30 µM unlabeled MODAG-005, anle138b, or selegiline for blocking. Subsequent procedures were performed in a safe light-illuminated dark room. The slides were dipped for five seconds into a 1:1 mixture of distilled water and Ilford K5 emulsion (Agar Scientific Ltd, Stansted, UK) molten in a 40°C water bath and left to dry in an upright position for two hours at room temperature. After drying, the slides were stored in the dark at 4°C for one to two weeks. For development, the slides were incubated for four minutes in Ilford Phenisol at 20°C, followed by one minute in Ilford Ilfostop and four minutes in Ilford Hypam (prepared according to manufacturer's instruction, Agar Scientific Ltd, Stansted, UK). The slides were then washed in running tap water for ten minutes and finally rinsed in distilled water.

Immunofluorescence

Immunofluorescence microscopy was carried out on the same brain sections after (micro)autoradiography. All sections were fixed with 4.5% PFA as above, when not performed prior to microautoradiography. For antigen retrieval, sodium citrate buffer (10 mM, pH 6.0, Sigma Aldrich Chemie GmbH, Darmstadt, Germany) was boiled and the brain sections to be stained for αSYN pSer129 and phospho-tau (pTau) were incubated at room temperature in the boiled buffer for 30 minutes; brain sections to be stained for $A\beta_{1\text{-}42}$ were incubated in 97% formic acid for ten minutes at room temperature. After washing, the sections were subsequently equilibrated in Tris-buffered saline (TBS) supplemented with 0.1% Triton X-100 and 1% BSA, pH 7.6 (in the following referred to as TBS-X) for ten minutes, before blocking in TBS supplemented with 0.3% Triton X-100 and 10% normal goat serum (Vector Laboratories, Linaris Biologische Produkte GmbH, Dossenheim, Germany) for 60 minutes at room temperature. Incubation with primary antibody was carried out overnight at 4°C with either mouse anti-phosphorylated αSYN pSer129 monoclonal antibody (1:5000 in TBS-X, pSyn#64; 015-25191, FUJIFILM Wako Chemicals Europe GmbH, Neuss, Germany), mouse anti-pTau (Ser202, Thr205) monoclonal antibody (1:500 in TBS-X, AT8, MN1020, Invitrogen, Rockford, IL, USA), or rabbit anti-$A\beta_{1\text{-}42}$ polyclonal antibody (1:200 in TBS-X, 218703, Synaptic Systems, Goettingen, Germany). After three times washing with TBS-X, the sections were incubated with secondary antibodies (1:250 in TBS-X) for one hour in the dark, using either goat anti-mouse Alexa Fluor 488 (A-11036, Invitrogen, Carlsbad, CA, USA), goat anti-mouse Alexa Fluor 647 (A32728, Invitrogen, Carlsbad, CA, USA), or goat anti-rabbit Alexa Fluor 568 (A-11036, Invitrogen, Carlsbad, CA, USA). After three washes following secondary antibody incubation, sections were stained with 3 nM 4′,6-diamidino-2-phenylindole (DAPI) (Invitrogen, Carlsbad, CA, USA) for five minutes and washed before being mounted on coverslips with ProLong Glass Antifade Mountant (Invitrogen, Carlsbad, CA, USA).

Whole-section images of the stained tissues were captured at 10 × magnification using Leica DMi8 microscope interfaced with Leica LAS X software (Leica Microsystems CMS GmbH, Wetzlar, Germany). The images were further processed with ImageJ. Background subtraction was performed with a rolling ball radius of 100 pixels for αSYN pSer129 and pTau staining, whereas a radius of 200 pixels was used for $A\beta_{1\text{-}42}$ staining.

For the correlative analysis of autoradiography and immunofluorescence microscopy in PD tissues, the immunofluorescence microscopy image was co-registered with the autoradiography image using the ImageJ plugin 'Big Warp'. Autoradiography images were processed and quantified as above. ROIs of 20 × 20 pixels were drawn covering the whole brain section. The same ROIs were applied for the co-registered immunofluorescence microscopy image. Mean grey values of the immunofluorescence microscopy image were measured and normalized by dividing them by maximum intensity. Correlation and linear regression analysis of the autoradiography and immunofluorescence microscopy were performed using GraphPad Prism software.

Immunohistochemistry

Immunohistochemistry of αSYN pS129, GFAP, and MAO-B was performed in brain tissue sections from human MSA cases, fibril-injected and non-injected rats, αSYN(A30P) and wild-type mice from *in vivo* PET study. Thawing, post-fixation (20 minutes) and antigen retrieval of the cryosections was performed as described in the immunofluorescence. Following antigen retrieval, the tissue sections underwent quenching

(1 mL quenching solution = 890 µL TBS, 100 µL methanol, and 10 µL 30% hydrogen peroxide) for 20 minutes to inhibit endogenous peroxidase. Following equilibration in buffer and one-hour blocking (0.3% Triton-X and 10% normal goat serum), mouse and rat tissues underwent an additional one-hour blocking step with goat F(ab) anti-mouse or anti-rat IgG (1:100 in TBS-X, ab6668 and ab7172, Abcam, Rozenburg, The Netherlands), respectively, to reduce background. Following F(ab) IgG blocking, tissues were washed for ten minutes in TBS-X. Incubation with primary antibody was carried out overnight at 4°C with either mouse anti-phosphorylated αSYN (pSer129) monoclonal antibody (1:5000 in TBS-X, pSyn#64; 015-25191, FUJIFILM Wako Chemicals Europe GmbH, Neuss, Germany), rabbit recombinant anti-GFAP antibody (1:1000 in TBS-X, EPR1034Y, Abcam, Rozenburg, The Netherlands) or rabbit polyclonal anti-MAO-B (1:2000 (for human tissue) or 1:2500 (for rodent tissue) in TBS-X, HPA002328, Atlas Antibodies, Bromma, Sweden). Following overnight incubation, tissues were washed three times with TBS-X and incubated with a secondary antibody (EnVision+/HRP Dual Link Rabbit/Mouse, K406189-2, Agilent, Waldbronn, Germany) for 30 minutes at room temperature. After washing, tissues were incubated with 3,3′-diaminobenzidine (1:50 in substrate buffer according to manufacturer's instruction, Agilent, Waldbronn, Germany) for up to ten minutes or NovaRED Substrate Kit (prepared according to manufacturer's instruction by Vector Laboratories, SK-4800, Biozol, Eching, Germany) for up to 20 minutes. Tissues were washed, dehydrated in an ethanol series, and cleared with Clear-Rite 3 (Epredia Netherlands B.V., DA Breda, Netherlands). Stained tissues were mounted with Eukitt quick-hardening mounting medium (Fluka Analytical, Munich, Germany) and scanned with a NanoZoomer 2.0 HT (Hamamatsu Photonics K.K., Hamamatsu, Japan) at 40 × magnification.

Semi-quantitative analysis by image thresholding was performed for the immunohistochemistry of αSYN pSer129 in the brainstem of aSYN(A30P) and wild-type mice from *in vivo* PET study. Stained tissues which presented with artifacts not feasible to be removed manually were excluded from analysis. All aSYN(A30P) mice (n = 14, 6–10 tissue sections per animal) and randomly selected wild-type mice (n = 5, 2 tissue sections per animal) were analyzed. ROI was drawn in the brainstem using QuPath (Version 0.4.2). Tissue border and any tissue artifacts were not included into the ROI to avoid staining artifacts. Images with the ROI were exported from QuPath to ImageJ with no pixel downsampling (resolution = 1) and subsequently converted to 8-bit images. A threshold of 0–120 was applied using the "Threshold" function of ImageJ to create binary images and the percentages positive area were measured. Furthermore, qualitative scoring was performed for the immunohistochemistry of MAO-B in aSYN(A30P) and wild-type mice from *in vivo* PET study. Two wild-type mice and two aSYN(A30P) mice were selected from each animal group based on the pathology load (> 5%, 1–5% and < 1% aSYN pSer129) determined by semi-quantitative analysis of aSYN pSer129 immunohistochemistry (4 tissue sections per animal). Staining in the brainstem, midbrain and hypothalamus was given a score from zero to three, where score zero depicted the absence of staining and score three represented the maximum staining which was observed across the stained tissues.

Radiosynthesis of [^{11}C]MODAG-005

Both the precursor anle190214 and the unlabeled reference compound were obtained as reported in "Precursor and Standard synthesis of MODAG-005". Radiolabeling was carried out by either reductive methylation with [^{11}C]CH_2O or direct methylation using [^{11}C]MeOTf [12, 53], to achieve highly selective labeling of the aniline nitrogen without loss of radioactivity through pyrazole-labelled side product formation, as well as a higher molar activity for *in vivo* binding experiments. All solvents and reagents were obtained by commercial suppliers with analytical grade and used without further purification.

Radiosynthesis by reductive methylation: [^{11}C]CO_2 was prepared by the bombardment of ^{14}N target gas containing 1% O_2 with 70 µA of 16.5 MeV protons on a PETtrace 890 cyclotron (GE Healthcare). No carrier added [^{11}C]CO_2 was delivered to the automatic synthesis module and [^{11}C]MeI was produced via the phase-gas conversion pathway [54]. Radiosynthesis, purification, and formulation were automated on Tracerlab FX MeI and Tracerlab FX M (GE Healthcare) radiochemical synthesizers Analytical HPLC was performed using an Infinity 1260 HPLC system (Agilent Technologies) equipped with a NaI(Tl) detector for radioactivity detection. Radiochemical and chemical purities of the radiolabeled compound as well as carrier content for calculation of molar radioactivity were determined by analytical radio-HPLC.

Briefly, [^{11}C]MeI was trapped in a solution of 1 mg anle190214 and 5 mg trimethylamine *N*-oxide in 350 µL diethyl formamide (DEF) and reacted for three minutes at 60°C. The Schiff-base intermediate was then reduced to [^{11}C]MODAG-005 by the addition of 1.2 mL 0.1 M citrate-phosphate buffer pH 5 containing 60 µL 2 M sodium cyanoborohydride in DEF and incubation for five minutes at 100°C. The product was purified by isocratic HPLC (Phenomenex Synergi Max-RP, 4 µm, 80 Å, 250 × 10 mm; 6 mL/min 55% acetonitrile in water; retention time seven minutes) and reformulated in 500 µL ethanol and 5 mL phosphate-buffered saline using a Sep-Pak Plus Light C18 cartridge (Waters, Eschborn, Germany). Radiochemical purity as well as carrier content for calculation of A_m were quantified by analytical HPLC (Phenomenex Luna Phenyl-Hexyl,

5 µm, 100 Å, 250 × 4.6 mm; 1.5 mL/min 30% acetonitrile). At the end of the synthesis (EOS), the radiochemical yield was 12.0 ± 2.2% and the A_m was 49.2 ± 11.2 GBq/μmol.

Radiosynthesis by direct methylation - method A: [^{11}C]MeI was obtained as above in "Radiosynthesis by reductive methylation". [^{11}C]MeOTf was generated by the reaction of the produced [^{11}C]MeI with silver triflate in an online flow-through process at 200°C under helium gas flow. The radiolabeling precursor anle190214 (1-2 mg, 3.17-6.35 µmoles) was dissolved in 500 µL of 2-butanone and the reaction vial was vortexed. No-carrier added [^{11}C]MeOTf was bubbled through the solution cooled to -20°C. The reaction mixture was heated to 75°C for two minutes. After cooling down to room temperature, the solution was diluted with 1.5 mL of H_2O and transferred to the HPLC system. The crude product purified by semi-preparative HPLC on a Synergi 4 µm Max-RP 80 Å, 250 × 100 mm column was eluted with an isocratic flow of 55% acetonitrile in water (flow rate: 6 mL/min) with a retention time of 6.5 minutes. Chromatograms were registered using an UV-detector (254 nm) and a Geiger-Müller tube. The HPLC fraction containing the purified product was diluted with 50 mL of water and loaded on a Sep-Pak Plus Light C18 cartridge, previously conditioned with 10 mL of ethanol and 10 mL of water. The cartridge was washed with 5 mL of water, and the product was eluted with 0.5 mL of ethanol and formulated with the addition of 5 mL of PBS. Radiochemical and chemical purities of the radiolabeled compound as well as carrier content for calculation of molar radioactivity were determined by analytical radio-HPLC.

At the EOS the radiochemical yield was 11.8 ± 2.7% and the A_m was 209 ± 44 GBq/μmol.

Another direct methylation method is presented in the **Supplementary Item 7** section.

Animals
Mouse and rat experiments were conducted in compliance with the European directives on the protection and use of laboratory animals (Council Directive 2010/63/UE) and with the German animal protection law and with the approval of the local authorities (Regierungspraesidium Tübingen (Germany), R3/19G). Nine female C57BL/6J mice (21 ± 1.7 g) and 13 female Sprague Dawley rats (307 ± 28.4 g) were obtained from Charles River Laboratories (Sulzfeld, Germany). Additionally, αSYN(A30P) transgenic mice (n = 14, 12 females and 2 males, 100 ± 10 weeks old, 30 ± 3.4 g), which express human αSYN with an A30P mutation under the Thy-1 promoter, and age-matched wild-type mice on the same C57BL/6J background (n = 14, 11 females and 3 males, 100 ± 11 weeks old, 32 ± 4.3 g), were bred in Hertie Institute for Clinical Brain Research (Tuebingen, Germany) and also kindly provided by Prof. Dr. Tiago Fleming Outeiro (University Medical Center Goettingen, Goettingen, Germany) (excluded n = 2 from each group, which died during the PET scan). All animals were maintained in our vivarium on a 12:12 hour light-dark cycle and were kept at a temperature of 22°C with 40-60% humidity with free access to a standard diet and tap water.

Macaque experiments were conducted in compliance with all applicable sections of the Final Rules of the Animal Welfare Act regulations (Code of Federal Regulations, Title 9), the Public Health Service Policy on Humane Care and Use of Laboratory Animals from the Office of Laboratory Animal Welfare, and the Guide for the Care and Use of Laboratory Animals from the National Research Council (OLAW, current edition) (NRC, current edition). Adult (> 5–6 years of age) male (n = 1, 6.0 kg, NHP 1) and female (n = 1, 6.4 kg, NHP 2) cynomolgus macaques (*Macaca fascicularis*) were maintained at Charles River Laboratories, Inc. (Mattawan, MI, USA, CRL Study No., 2579-100) on a 12:12 hour light-dark cycle. They were kept at temperatures of 18 to 29°C with 30–70% humidity with free access to a standard diet and tap water.

Patient
The first translational use of the [^{11}C]MODAG-05 was performed in a 70 year-old female patient clinically diagnosed with an overlap syndrome of MSA-P and MSA-C supported by findings on MRI and [^{123}I]FP-CIT SPECT imaging indicating advanced neurodegeneration.

The clinical syndrome of our patient was characterized by cerebellar gait and limb ataxia (unsteady gait and dysmetria), mixed hypokinetic-cerebellar dysarthria in combination with parkinsonism (left-sided bradykinesia, rigidity, marked postural instability), autonomic dysfunction (urinary urge and orthostatic hypotension) as well as lack of response to dopaminergic drug therapy, consistent with the diagnosis of clinically established MSA according to the Movement Disorder Society Criteria for the Diagnosis of Multiple System Atrophy [49].

The patient was referred to the experimental diagnostics unit since the patient presented with an overlap syndrome of MSA-P and MSA-C.

Absence of Aβ copathology was determined by cerebrospinal fluid (CSF) analysis of Aβ1-42, Aβ1-40, Aβ1-42/ Aβ1-40 ratio, phospho- and total Tau using a fully automated chemiluminescent enzyme immunoassay (CLEIA) with commercially available kits on the LUMIPULSE® G600II platform (Fujirebio Europe, Ghent, Belgium).

αSYN fibril injection into the rat brain

Stereotactic surgeries were performed as previously described [12]. Briefly, rats (n = 7) were intracranially injected with 4 µL of αSYN fibrils (30 µM) using a stereotaxic injector (Stoelting, Wood Lane, IL, USA) (0.4 µL every 60 seconds.) into the right striatum (medial-lateral = -3.4 mm, anterior-posterior = 0.0 mm, dorsoventral = -4.8 mm) according to the stereotaxic atlas of Paxinos and Watson [55]. A contralateral injection of 4 µL vehicle (50 mM Tris-buffer, 100 mM sodium chloride, 0.02% sodium azide, pH 7.0) served as negative control. PET imaging was performed either four days or between three to four days (for blocking study) post injection. Thioflavin S staining on coronal 30 µm cryosections of fibril-injected rats was performed as described in [12]. Images were captured using a Leica DMi8 microscope and FITC filter settings (excitation 460 nm–500 nm; emission 512 nm–542 nm). Autoradiography of the cryosections was performed as described above, using 3 nM [^{3}H]MODAG-005 and 3 µM unlabeled MODAG-005 for blocking.

***In vivo* PET and MRI analysis in mice and rats**

PET imaging was performed as described previously [12]. Mice and rats were anaesthetized with 1.5-1.7% isoflurane evaporated in 100% oxygen at a flow rate of 0.8 L/min. Their body temperature was maintained at 37°C using a feedback temperature control unit. Five seconds after the start of the PET acquisition, mice for the pharmacokinetic study (n = 3) were injected intravenously (i.v.) with 14 ± 0.7 MBq of [^{11}C]MODAG-005 (A_m = 37 ± 9.2 GBq/µmol at time of injection) and rats for the pharmacokinetic and fibril injection studies (four days post-injection) (n = 8) with 24 ± 3.0 MBq (A_m = 41 ± 6.8 GBq/µmol at time of injection) produced by reductive methylation. Dynamic PET data were acquired for 60 minutes and divided into 39 time frames (12×5 s, 6×10 s, 6×30 s, 5×60 s, and 10×300 s). For the blocking study in fibril-injected rats as well as the study in the αSYN(A30P) transgenic mouse model, animals were injected i.v. with 27 ± 1.6 MBq (A_m = 134 ± 33.6 GBq/µmol at time of injection) and 15 ± 0.9 MBq (A_m = 175 ± 82.4 GBq/µmol at time of injection) of [^{11}C]MODAG-005, respectively, which was produced by direct methylation method A. For the blocking study in fibril-injected rats, two PET scans between three to four days after fibril injection were performed, which consisted of a baseline measurement with vehicle injection (20% PEG-400 (Carl Roth GmbH, Karlsruhe, Germany) and 80% of 20% aqueous sulfobutyl ether β-cyclodextrin sodium (CycloLab Ltd., Budapest, Hungary)) and a blocking measurement with the administration of anle138b (1 mg/kg dose in the vehicle) as a single intravenously bolus five minutes before tracer injection. Dynamic 60-minute PET data were divided into 45 frames (10 × 2 s, 8 × 5 s, 6 ×10 s, 6 × 30 s, 5 × 60 s, 10 × 300 s). For attenuation correction, a 13-minute transmission measurement with a cobalt-57 point source was performed after the PET data acquisition.

Subsequently, animals were sacrificed under CO_2 and perfused with cold PBS. Brains were extracted and frozen immediately either in 2-methybutane cooled on dry ice (fibril-injected rats) or in TissueTek (mice). OSEM3D was used as data reconstruction algorithm. After the PET acquisition of mice in the pharmacokinetic study, whole-body anatomical magnetic resonance images were acquired on a 7T small animal magnetic resonance imaging (MRI) scanner (Bruker BioSpin GmbH, Ettlingen, Germany). Animals were kept under 1.5% isoflurane anesthesia evaporated in 100% oxygen at a flow rate of 0.8 L/min. Signal transmission and readout were performed using a linearly polarized radiofrequency coil with an inner diameter of 72 mm (Bruker BioSpin GmbH, Ettlingen, Germany). A localizer sequence was used to position the mice in the centre of the field of view. Anatomical images were acquired with a Turbo RARE T2 sequence (TR/TE 800 ms/35.1 ms, FoV 37.4 mm × 85.8 mm × 22.8 mm, Matrix 144 × 256 × 92).

Mouse PET scans were co-registered to the whole-body MRI scan. Based on the MRI anatomy, volumes of interest of the lung, liver, heart, brain, and kidneys were hand-drawn using PMOD software (version 3.2; PMOD Technologies, Zürich, Switzerland). The volumes of interest of different regions in the rat and mouse brain were extracted using the atlas provided by PMOD [56-58]. TACs were extracted and converted to SUVs, calculated as in **equation (1)**:

$$SUV\ (t) = \frac{radioactivity\ concentration\ (\frac{kBq}{mL})}{\frac{injected\ dose}{body\ weight}\ (\frac{kBq}{g})} \quad (1)$$

Additionally, the SUV ratio (SUVR) was calculated using the cerebellum or the left/sham-injected striatum as the reference region in the study in fibril-injected rats, and using the cortex as reference in the study in the αSYN(A30P) mouse model. SUVR values were calculated with **equation (2)**:

$$SUVR = \frac{radioactivity\ in\ target\ region}{radioactivity\ in\ referece\ region} \quad (2)$$

***In vivo* PET/MRI in non-human primates**

In vivo macaque experiments were performed at Charles River Laboratories, Inc. (Mattawan, MI, USA) under the sponsorship of inviCRO LLC (Needham, MA, USA). Macaques were initially sedated by intramuscularly administering 5-10 mg/kg of ketamine and maintained under 2.0% isoflurane evaporated in 100% oxygen at a flow rate of 2 L/min. Body temperature was maintained at 38°C. Heart rate (BPM), body temperature, expired CO_2, respiration/min, pulse O_2%, % anesthetic gas, and oxygen (L/min) were monitored at approximately 15-minute intervals throughout the time course of the scans. The brains were placed in the center of the FOV in a Siemens microPET Focus 220 scanner (Siemens, Knoxville, TN) in a head-first supine orientation. Macaques received a three-minute intravenous injection of either 6 mL of vehicle control at baseline or 1 mg/kg dose of MODAG-005 beginning five minutes prior to the injection of 127 MBq (m) or 57 MBq (f) of [^{11}C]MODAG-005 (A_m at time of injection = 33 ± 7 GBq/µmol) produced by direct methylation method B (**Supplementary Item 7**). Dynamic PET data were acquired for 120 minutes and divided into 33 time frames (6 × 30 s, 3 × 60 s, 2 × 120 s, and 22 × 300 s). Filtered back projection was used as data reconstruction algorithm at a 256 × 256 matrix. Following the PET acquisition, anatomical T_1-weighted images were acquired with a Philips Intera 1.5T MRI scanner using a focused-head 3D T_1FE (gradient spoiled) sequence. The PET data were rigidly co-registered to the MRI, and the MRI was normalized to the cynomolgus template; the combined transformations were used to map the PET volumes into cynomolgus template space to delineate volumes of interest (VOIs). Ten VOIs were extracted from the brain using the brain atlas in PMOD 3.802. TACs were extracted and converted to SUVs, calculated as in **equation (1)**.

Arterial blood sampling for activity measurements in blood and plasma and metabolite analysis (identified in bold italic) via a right inguinal (external iliac) or left internal iliac artery vascular access port was performed during the PET acquisition at 0.25, 0.75, 1.25, 1.75, 2.25, 3.25, 4, ***5***, ***10***, ***15***, ***30***, ***45***, ***60***, 90, and 120 minutes post tracer administration.

At least 14 days after the baseline scan, animals were re-scanned as above with 89 MBq (m) and 222 MBq (f) [^{11}C]MODAG-005 and in addition with a three-minute infusion of 1 mg/kg unlabeled MODAG-005 in the vehicle, five minutes before the start of the PET acquisition. Arterial blood sampling for metabolite analysis from the right inguinal (external iliac) or left internal iliac artery via the vascular access port was performed as above.

Volume of distribution (VT) and K1 values estimated from a 2-tissue-compartment model at baseline and after competition with MODAG-005.

***In vivo* PET, SPECT and MRI in humans**

For the diagnostic work-up of the neurodegenerative Parkinson syndrome a DAT SPECT (3 h. p.i. of 185 MBq [^{123}I]FP-CIT; Discovery 670 GE Healtcare) was performed 3 years before the patient presented again in our imaging department.

PET imaging was performed on a high sensitive Long-Field of-View PET/CT scanner (Biograph Vision Quadra Siemens Healthineers) after intravenous bolus injection of 49 MBq [^{11}C]MODAG-005 (A_m at time of injection 39 GBq/µmol). Dynamic PET data were acquired for 60 minutes and divided into 15 time frames (10 × 60 s, 5 × 600 s). OSEM 3D was used as the data reconstruction algorithm and attenuation correction was applied based on the CT. In addition, a clinical 3T-MRI (Siemens Magnetom Prisma Fit) was performed at the same day which included (T1- and T2-weighted sequences). The PET data were co-registered to the MRI, and VOIs (right and left caudate, putamen, thalamus, pons, cerebellar white matter and the occipital cortex) were drawn based on the anatomical information in the MR image. TACs were extracted and converted to SUVs, calculated as in **equation (1)**.

***Ex vivo* metabolite analysis in plasma and brain**

Metabolite analysis in mice and rats was performed as described previously [12]. Briefly, each anaesthetized mouse was injected with 204 ± 36.9 MBq of [^{11}C]MODAG-005 (A_m = 37 ± 11 GBq/µmol at time of injection), and each rat with 436 ± 2.7 MBq (A_m = 46 ± 0.8 GBq/µmol at time of injection) produced by reductive

methylation using a tail vein catheter. Five or 15 minutes post tracer injection, blood plasma samples were collected by heart puncture and the perfused brain of the mouse or right hemisphere of the rat was homogenized in phosphate-buffered saline. After sample preparation as described in [12], separation was achieved by reversed-phase radio-HPLC on a Luna C18(2) column (5 µm, 100 Å, 250 mm × 4.6 mm, Phenomenex, Aschaffenburg, Germany) with 0.1% trifluoroacetic acid in water/acetonitrile (70/30) and an isocratic flow of 1.5 mL/min. Data were decay corrected to the start-time-point of the first sample and analyzed as previously described using the peak analyzer function in Origin software (OriginLab Corporation, version 9.1G, Northampton, MA, USA) [12].

Plasma metabolite analysis in NHPs was performed from samples collected during the PET acquisition. An Agilent 1100 HPLC system, equipped with a coincidence detector for radioactivity and a diode array detector for UV that was set to 287 nm, was used. Plasma (500 µL) was diluted with a diluent solution (1.0 mL of 10 µg/mL cold MODAG-005 standard in water) and injected directly onto a Phenomenex Onyx monolithic column (10 × 100 mm), which was fitted with a 10×10 mm guard cartridge. The solvent A was 100 mM ammonium acetate, pH 8.0, and the solvent B was acetonitrile. The samples were analyzed using a gradient method. The parent compound HPLC retention time was identified by injection of 1 µL of [^{11}C]MODAG-005 mixed with 1.5 mL water containing 10 µg MODAG-005 and 5 µL DMSO. 50-200 µCi of a [^{11}C]MODAG-005 dose solution in a volume no greater than 0.25 mL was spiked into two 2.5 mL arterial blood samples, which were taken shortly before a dose injection, to measure *ex vivo* blood metabolism, and labelled as “Standard A”, and “Standard B”. Standard B was analyzed immediately post-processing from whole blood to plasma. Standard A was retained at room temperature and processed to plasma at the same time as the 120-minute post-injection sample. The *in vivo* metabolism of [^{11}C]MODAG-005 was analyzed from 3.5 mL arterial blood samples that were collected at 5, 15, 30, 45, and 60 minutes post injection. The whole blood samples were centrifuged at 1,300 × g for six minutes at 4°C to separate plasma, of which 500 µL was injected into the metabolite profiling HPLC system for analyzing the radio-metabolites.

Data were analysed as previously described [12] using the peak analyzer function in Origin software (OriginLab Corporation, version 9.1G, Northampton, MA, USA) with correction for radioactive decay within the respective run.

Reporting Summary. Further information on research design is available in the Nature Research Reporting Summary linked to this article.

Data availability

Data associated with the reported findings are available in the manuscript or **Supplementary Information**. All raw and analyzed PET and MRI datasets for the data analysis will be made available at the DRYAD repository upon publication.

References

1. Palermo, G, Del Prete, E, Bonuccelli, U, and Ceravolo, R, *Early autonomic and cognitive dysfunction in PD, DLB and MSA: blurring the boundaries between alpha-synucleinopathies.* J Neurol, 2020. **267**(12): p. 3444-3456.
2. Gomez-Tortosa, E, Newell, K, Irizarry, MC, Sanders, JL, and Hyman, BT, *alpha-Synuclein immunoreactivity in dementia with Lewy bodies: morphological staging and comparison with ubiquitin immunostaining.* Acta Neuropathol, 2000. **99**(4): p. 352-7.
3. Dupont, AC, Largeau, B, Guilloteau, D, Santiago Ribeiro, MJ, and Arlicot, N, *The Place of PET to Assess New Therapeutic Effectiveness in Neurodegenerative Diseases.* Contrast Media Mol Imaging, 2018. **2018**: p. 7043578.
4. Korat, Š, Bidesi, NSR, Bonanno, F, Di Nanni, A, Hoàng, ANN, Herfert, K, Maurer, A, Battisti, UM, Bowden, GD, Thonon, D, Vugts, D, Windhorst, AD, and Herth, MM, *Alpha-Synuclein PET Tracer Development-An Overview about Current Efforts.* Pharmaceuticals (Basel), 2021. **14**(9).
5. Matsuoka, K, Ono, M, Takado, Y, Hirata, K, Endo, H, Ohfusa, T, Kojima, T, Yamamoto, T, Onishi, T, Orihara, A, Tagai, K, Takahata, K, Seki, C, Shinotoh, H, Kawamura, K, Shimizu, H, Shimada, H, Kakita, A, Zhang, M-R, Suhara, T, and Higuchi, M, *High-Contrast Imaging of α-Synuclein Pathologies in Living Patients with Multiple System Atrophy.* 2022. **37**(10): p. 2159-2161.
6. Xiang, J, Tao, Y, Xia, Y, Luo, S, Zhao, Q, Li, B, Zhang, X, Sun, Y, Xia, W, Zhang, M, Kang, SS, Ahn, EH, Liu, X, Xie, F, Guan, Y, Yang, JJ, Bu, L, Wu, S, Wang, X, Cao, X, Liu, C, Zhang, Z, Li, D, and Ye, K, *Development of an α-synuclein positron emission tomography tracer for imaging synucleinopathies.* Cell, 2023. **186**(16): p. 3350-3367.e19.
7. Smith, R, Capotosti, F, Schain, M, Ohlsson, T, Vokali, E, Molette, J, Touilloux, T, Hliva, V, Dimitrakopoulos, IK, Puschmann, A, Jögi, J, Svenningsson, P, Andréasson, M, Sandiego, C, Russell,

DS, Miranda-Azpiazu, P, Halldin, C, Stomrud, E, Hall, S, Bratteby, K, Tampio L'Estrade, E, Luthi-Carter, R, Pfeifer, A, Kosco-Vilbois, M, Streffer, J, and Hansson, O, *The α-synuclein PET tracer [18F] ACI-12589 distinguishes multiple system atrophy from other neurodegenerative diseases.* Nat Commun, 2023. **14**(1): p. 6750.

8. Fares, MB, Jagannath, S, and Lashuel, HA, *Reverse engineering Lewy bodies: how far have we come and how far can we go?* Nature Reviews Neuroscience, 2021. **22**(2): p. 111-131.
9. Close, W, Neumann, M, Schmidt, A, Hora, M, Annamalai, K, Schmidt, M, Reif, B, Schmidt, V, Grigorieff, N, and Fändrich, M, *Physical basis of amyloid fibril polymorphism.* Nature Communications, 2018. **9**(1): p. 699.
10. Shahmoradian, SH, Lewis, AJ, Genoud, C, Hench, J, Moors, TE, Navarro, PP, Castano-Diez, D, Schweighauser, G, Graff-Meyer, A, Goldie, KN, Sutterlin, R, Huisman, E, Ingrassia, A, Gier, Y, Rozemuller, AJM, Wang, J, Paepe, A, Erny, J, Staempfli, A, Hoernschemeyer, J, Grosseruschkamp, F, Niedieker, D, El-Mashtoly, SF, Quadri, M, Van, IWFJ, Bonifati, V, Gerwert, K, Bohrmann, B, Frank, S, Britschgi, M, Stahlberg, H, Van de Berg, WDJ, and Lauer, ME, *Lewy pathology in Parkinson's disease consists of crowded organelles and lipid membranes.* Nat Neurosci, 2019. **22**(7): p. 1099-1109.
11. Wagner, J, Ryazanov, S, Leonov, A, Levin, J, Shi, S, Schmidt, F, Prix, C, Pan-Montojo, F, Bertsch, U, Mitteregger-Kretzschmar, G, Geissen, M, Eiden, M, Leidel, F, Hirschberger, T, Deeg, AA, Krauth, JJ, Zinth, W, Tavan, P, Pilger, J, Zweckstetter, M, Frank, T, Bahr, M, Weishaupt, JH, Uhr, M, Urlaub, H, Teichmann, U, Samwer, M, Botzel, K, Groschup, M, Kretzschmar, H, Griesinger, C, and Giese, A, *Anle138b: a novel oligomer modulator for disease-modifying therapy of neurodegenerative diseases such as prion and Parkinson's disease.* Acta Neuropathol, 2013. **125**(6): p. 795-813.
12. Kuebler, L, Buss, S, Leonov, A, Ryazanov, S, Schmidt, F, Maurer, A, Weckbecker, D, Landau, AM, Lillethorup, TP, Bleher, D, Saw, RS, Pichler, BJ, Griesinger, C, Giese, A, and Herfert, K, *[(11)C]MODAG-001-towards a PET tracer targeting alpha-synuclein aggregates.* Eur J Nucl Med Mol Imaging, 2020.
13. Maurer, A, Leonov, A, Ryazanov, S, Herfert, K, Kuebler, L, Buss, S, Schmidt, F, Weckbecker, D, Linder, R, Bender, D, Giese, A, Pichler, BJ, and Griesinger, C, *(11) C Radiolabeling of anle253b: a Putative PET Tracer for Parkinson's Disease That Binds to alpha-Synuclein Fibrils in vitro and Crosses the Blood-Brain Barrier.* ChemMedChem, 2019.
14. Raval, NR, Shalgunov, V, Nasser, A, Madsen, CA, Battisti, UM, Herth, MM, Jørgensen, LM, Plavén-Sigray, P, and Knudsen, GM, *Evaluation of the α-synuclein PET radiotracer (d3)-[11C]MODAG-001 in a protein deposition pig model.* Neuroscience Applied, 2022. **1**: p. 100016.
15. Harada, R, Furumoto, S, Kudo, Y, Yanai, K, Villemagne, VL, and Okamura, N, *Imaging of Reactive Astrogliosis by Positron Emission Tomography.* Front Neurosci, 2022. **16**: p. 807435.
16. Innis, RB, Cunningham, VJ, Delforge, J, Fujita, M, Gjedde, A, Gunn, RN, Holden, J, Houle, S, Huang, SC, Ichise, M, Iida, H, Ito, H, Kimura, Y, Koeppe, RA, Knudsen, GM, Knuuti, J, Lammertsma, AA, Laruelle, M, Logan, J, Maguire, RP, Mintun, MA, Morris, ED, Parsey, R, Price, JC, Slifstein, M, Sossi, V, Suhara, T, Votaw, JR, Wong, DF, and Carson, RE, *Consensus nomenclature for in vivo imaging of reversibly binding radioligands.* J Cereb Blood Flow Metab, 2007. **27**(9): p. 1533-9.
17. Levin, J, Sing, N, Melbourne, S, Morgan, A, Mariner, C, Spillantini, MG, Wegrzynowicz, M, Dalley, JW, Langer, S, Ryazanov, S, Leonov, A, Griesinger, C, Schmidt, F, Weckbecker, D, Prager, K, Matthias, T, and Giese, A, *Safety, tolerability and pharmacokinetics of the oligomer modulator anle138b with exposure levels sufficient for therapeutic efficacy in a murine Parkinson model: A randomised, double-blind, placebo-controlled phase 1a trial.* eBioMedicine, 2022. **80**: p. 104021.
18. Volc, D, Poewe, W, Kutzelnigg, A, Lührs, P, Thun-Hohenstein, C, Schneeberger, A, Galabova, G, Majbour, N, Vaikath, N, El-Agnaf, O, Winter, D, Mihailovska, E, Mairhofer, A, Schwenke, C, Staffler, G, and Medori, R, *Safety and immunogenicity of the α-synuclein active immunotherapeutic PD01A in patients with Parkinson's disease: a randomised, single-blinded, phase 1 trial.* Lancet Neurol, 2020. **19**(7): p. 591-600.
19. Lang, AE, Siderowf, AD, Macklin, EA, Poewe, W, Brooks, DJ, Fernandez, HH, Rascol, O, Giladi, N, Stocchi, F, Tanner, CM, Postuma, RB, Simon, DK, Tolosa, E, Mollenhauer, B, Cedarbaum, JM, Fraser, K, Xiao, J, Evans, KC, Graham, DL, Sapir, I, Inra, J, Hutchison, RM, Yang, M, Fox, T, Budd Haeberlein, S, Dam, T, and Investigators, S, *Trial of Cinpanemab in Early Parkinson's Disease.* N Engl J Med, 2022. **387**(5): p. 408-420.
20. Pagano, G, Taylor, KI, Anzures-Cabrera, J, Marchesi, M, Simuni, T, Marek, K, Postuma, RB, Pavese, N, Stocchi, F, Azulay, JP, Mollenhauer, B, López-Manzanares, L, Russell, DS, Boyd, JT, Nicholas, AP, Luquin, MR, Hauser, RA, Gasser, T, Poewe, W, Ricci, B, Boulay, A, Vogt, A, Boess, FG, Dukart, J, D'Urso, G, Finch, R, Zanigni, S, Monnet, A, Pross, N, Hahn, A, Svoboda, H, Britschgi, M, Lipsmeier, F, Volkova-Volkmar, E, Lindemann, M, Dziadek, S, Holiga, Š, Rukina, D, Kustermann, T, Kerchner, GA, Fontoura, P, Umbricht, D, Doody, R, Nikolcheva, T, and Bonni, A, *Trial of Prasinezumab in Early-Stage Parkinson's Disease.* N Engl J Med, 2022. **387**(5): p. 421-432.

21. Eidelberg, D, Moeller, JR, Dhawan, V, Spetsieris, P, Takikawa, S, Ishikawa, T, Chaly, T, Robeson, W, Margouleff, D, Przedborski, S, and et al., *The metabolic topography of parkinsonism.* J Cereb Blood Flow Metab, 1994. **14**(5): p. 783-801.
22. Breit, S, Reimold, M, Reischl, G, Klockgether, T, and Wüllner, U, *[(11)C]d-threo-methylphenidate PET in patients with Parkinson's disease and essential tremor.* J Neural Transm (Vienna), 2006. **113**(2): p. 187-93.
23. Volkow, ND, Ding, YS, Fowler, JS, Wang, GJ, Logan, J, Gatley, SJ, Schlyer, DJ, and Pappas, N, *A new PET ligand for the dopamine transporter: studies in the human brain.* J Nucl Med, 1995. **36**(12): p. 2162-8.
24. Klunk, WE, Engler, H, Nordberg, A, Wang, Y, Blomqvist, G, Holt, DP, Bergström, M, Savitcheva, I, Huang, GF, Estrada, S, Ausén, B, Debnath, ML, Barletta, J, Price, JC, Sandell, J, Lopresti, BJ, Wall, A, Koivisto, P, Antoni, G, Mathis, CA, and Långström, B, *Imaging brain amyloid in Alzheimer's disease with Pittsburgh Compound-B.* Ann Neurol, 2004. **55**(3): p. 306-19.
25. Jie, C, Treyer, V, Schibli, R, and Mu, L, *Tauvid™: The First FDA-Approved PET Tracer for Imaging Tau Pathology in Alzheimer's Disease.* Pharmaceuticals (Basel), 2021. **14**(2).
26. Barthel, H and Sabri, O, *Clinical Use and Utility of Amyloid Imaging.* 2017. **58**(11): p. 1711-1717.
27. Hashimoto, H, Kawamura, K, Igarashi, N, Takei, M, Fujishiro, T, Aihara, Y, Shiomi, S, Muto, M, Ito, T, Furutsuka, K, Yamasaki, T, Yui, J, Xie, L, Ono, M, Hatori, A, Nemoto, K, Suhara, T, Higuchi, M, and Zhang, MR, *Radiosynthesis, photoisomerization, biodistribution, and metabolite analysis of 11C-PBB3 as a clinically useful PET probe for imaging of tau pathology.* J Nucl Med, 2014. **55**(9): p. 1532-8.
28. Sevigny, J, Chiao, P, Bussière, T, Weinreb, PH, Williams, L, Maier, M, Dunstan, R, Salloway, S, Chen, T, Ling, Y, O'Gorman, J, Qian, F, Arastu, M, Li, M, Chollate, S, Brennan, MS, Quintero-Monzon, O, Scannevin, RH, Arnold, HM, Engber, T, Rhodes, K, Ferrero, J, Hang, Y, Mikulskis, A, Grimm, J, Hock, C, Nitsch, RM, and Sandrock, A, *The antibody aducanumab reduces Aβ plaques in Alzheimer's disease.* Nature, 2016. **537**(7618): p. 50-56.
29. Swanson, CJ, Zhang, Y, Dhadda, S, Wang, J, Kaplow, J, Lai, RYK, Lannfelt, L, Bradley, H, Rabe, M, Koyama, A, Reyderman, L, Berry, DA, Berry, S, Gordon, R, Kramer, LD, and Cummings, JL, *A randomized, double-blind, phase 2b proof-of-concept clinical trial in early Alzheimer's disease with lecanemab, an anti-Aβ protofibril antibody.* Alzheimer's Research & Therapy, 2021. **13**(1): p. 80.
30. Klein, G, Delmar, P, Kerchner, GA, Hofmann, C, Abi-Saab, D, Davis, A, Voyle, N, Baudler, M, Fontoura, P, and Doody, R, *Thirty-Six-Month Amyloid Positron Emission Tomography Results Show Continued Reduction in Amyloid Burden with Subcutaneous Gantenerumab.* The Journal of Prevention of Alzheimer's Disease, 2021. **8**(1): p. 3-6.
31. Salloway, S, Farlow, M, McDade, E, Clifford, DB, Wang, G, Llibre-Guerra, JJ, Hitchcock, JM, Mills, SL, Santacruz, AM, Aschenbrenner, AJ, Hassenstab, J, Benzinger, TLS, Gordon, BA, Fagan, AM, Coalier, KA, Cruchaga, C, Goate, AA, Perrin, RJ, Xiong, C, Li, Y, Morris, JC, Snider, BJ, Mummery, C, Surti, GM, Hannequin, D, Wallon, D, Berman, SB, Lah, JJ, Jimenez-Velazquez, IZ, Roberson, ED, van Dyck, CH, Honig, LS, Sánchez-Valle, R, Brooks, WS, Gauthier, S, Galasko, DR, Masters, CL, Brosch, JR, Hsiung, G-YR, Jayadev, S, Formaglio, M, Masellis, M, Clarnette, R, Pariente, J, Dubois, B, Pasquier, F, Jack, CR, Koeppe, R, Snyder, PJ, Aisen, PS, Thomas, RG, Berry, SM, Wendelberger, BA, Andersen, SW, Holdridge, KC, Mintun, MA, Yaari, R, Sims, JR, Baudler, M, Delmar, P, Doody, RS, Fontoura, P, Giacobino, C, Kerchner, GA, Bateman, RJ, Formaglio, M, Mills, SL, Pariente, J, van Dyck, CH, and the Dominantly Inherited Alzheimer Network–Trials, U, *A trial of gantenerumab or solanezumab in dominantly inherited Alzheimer's disease.* Nature Medicine, 2021. **27**(7): p. 1187-1196.
32. Verdurand, M, Levigoureux, E, Zeinyeh, W, Berthier, L, Mendjel-Herda, M, Cadarossanesaib, F, Bouillot, C, Iecker, T, Terreux, R, Lancelot, S, Chauveau, F, Billard, T, and Zimmer, L, *In Silico, in Vitro, and in Vivo Evaluation of New Candidates for alpha-Synuclein PET Imaging.* Mol Pharm, 2018. **15**(8): p. 3153-3166.
33. Akasaka, T, Watanabe, H, Kaide, S, Iikuni, S, Hasegawa, M, and Ono, M, *Synthesis and evaluation of novel radioiodinated phenylbenzofuranone derivatives as α-synuclein imaging probes.* Bioorg Med Chem Lett, 2022. **64**: p. 128679.
34. Kaide, S, Watanabe, H, Shimizu, Y, Iikuni, S, Nakamoto, Y, Hasegawa, M, Itoh, K, and Ono, M, *Identification and Evaluation of Bisquinoline Scaffold as a New Candidate for alpha-Synuclein-PET Imaging.* ACS Chem Neurosci, 2020. **11**(24): p. 4254-4261.
35. Kaide, S, Watanabe, H, Iikuni, S, Hasegawa, M, Itoh, K, and Ono, M, *Chalcone Analogue as New Candidate for Selective Detection of α-Synuclein Pathology.* ACS Chem Neurosci, 2022. **13**(1): p. 16-26.
36. Janssen, B, Tian, G, Lengyel-Zhand, Z, Hsieh, CJ, Lougee, MG, Riad, A, Xu, K, Hou, C, Weng, CC, Lopresti, BJ, Kim, HJ, Pagar, VV, Ferrie, JJ, Garcia, BA, Mathis, CA, Luk, K, Petersson, EJ, and Mach, RH, *Identification of a Putative α-synuclein Radioligand Using an in silico Similarity Search.* Mol Imaging Biol, 2023. **25**(4): p. 704-719.

37. Zhang, S, Zhu, R, Pan, B, Xu, H, Olufemi, MF, Gathagan, RJ, Li, Y, Zhang, L, Zhang, J, Xiang, W, Kagan, EM, Cao, X, Yuan, C, Kim, SJ, Williams, CK, Magaki, S, Vinters, HV, Lashuel, HA, Garcia, BA, James Petersson, E, Trojanowski, JQ, Lee, VM, and Peng, C, *Post-translational modifications of soluble α-synuclein regulate the amplification of pathological α-synuclein.* Nat Neurosci, 2023. **26**(2): p. 213-225.
38. Matsuoka, K, Ono, M, Takado, Y, Hirata, K, Endo, H, Ohfusa, T, Kojima, T, Yamamoto, T, Onishi, T, Orihara, A, Tagai, K, Takahata, K, Seki, C, Shinotoh, H, Kawamura, K, Shimizu, H, Shimada, H, Kakita, A, Zhang, MR, Suhara, T, and Higuchi, M, *High-Contrast Imaging of α-Synuclein Pathologies in Living Patients with Multiple System Atrophy.* Mov Disord, 2022.
39. Molette J., GE, Darmency V., *BICYCLIC COMPOUNDS FOR DIAGNOSIS AND THERAPY*, A.I. Sa, Editor. 2017.
40. Endo, H, Ono, M, Takado, Y, Matsuoka, K, Takahashi, M, Tagai, K, Kataoka, Y, Hirata, K, Takahata, K, Seki, C, Kokubo, N, Fujinaga, M, Mori, W, Nagai, Y, Mimura, K, Kumata, K, Kikuchi, T, Shimozawa, A, Mishra, SK, Yamaguchi, Y, Shimizu, H, Kakita, A, Takuwa, H, Shinotoh, H, Shimada, H, Kimura, Y, Ichise, M, Suhara, T, Minamimoto, T, Sahara, N, Kawamura, K, Zhang, M-R, Hasegawa, M, and Higuchi, M, *Imaging α-synuclein pathologies in animal models and patients with Parkinson's and related diseases.* 2023: p. 2020.10.23.349860.
41. Bagchi, DP, Yu, L, Perlmutter, JS, Xu, J, Mach, RH, Tu, Z, and Kotzbauer, PT, *Binding of the radioligand SIL23 to alpha-synuclein fibrils in Parkinson disease brain tissue establishes feasibility and screening approaches for developing a Parkinson disease imaging agent.* PLoS One, 2013. **8**(2): p. e55031.
42. Breydo, L and Uversky, VN, *Structural, morphological, and functional diversity of amyloid oligomers.* FEBS Lett, 2015. **589**(19 Pt A): p. 2640-8.
43. Pike, VW, *PET radiotracers: crossing the blood-brain barrier and surviving metabolism.* Trends Pharmacol Sci, 2009. **30**(8): p. 431-40.
44. Leung, CS, Leung, SS, Tirado-Rives, J, and Jorgensen, WL, *Methyl effects on protein-ligand binding.* J Med Chem, 2012. **55**(9): p. 4489-500.
45. Neumann, M, Kahle, PJ, Giasson, BI, Ozmen, L, Borroni, E, Spooren, W, Müller, V, Odoy, S, Fujiwara, H, Hasegawa, M, Iwatsubo, T, Trojanowski, JQ, Kretzschmar, HA, and Haass, C, *Misfolded proteinase K-resistant hyperphosphorylated alpha-synuclein in aged transgenic mice with locomotor deterioration and in human alpha-synucleinopathies.* J Clin Invest, 2002. **110**(10): p. 1429-39.
46. Schell, H, Hasegawa, T, Neumann, M, and Kahle, PJ, *Nuclear and neuritic distribution of serine-129 phosphorylated alpha-synuclein in transgenic mice.* Neuroscience, 2009. **160**(4): p. 796-804.
47. Schou, M, Varnäs, K, Sandell, J, Johnström, P, Cselenyi, Z, Svensson, S, Nakao, R, Amini, N, Bergman, L, Sumic, A, Gulyas, B, Lindström-Böö, E, Halldin, C, and Farde, L, *Synthesis, Radiolabeling, and In Vivo Pharmacokinetic Evaluation of the Amyloid Beta Radioligand [11C]AZD4694 in Nonhuman Primates.* Molecular Imaging and Biology, 2014. **16**(2): p. 173-179.
48. Drake, LR, Pham, JM, Desmond, TJ, Mossine, AV, Lee, SJ, Kilbourn, MR, Koeppe, RA, Brooks, AF, and Scott, PJH, *Identification of AV-1451 as a Weak, Nonselective Inhibitor of Monoamine Oxidase.* ACS Chemical Neuroscience, 2019. **10**(8): p. 3839-3846.
49. Wenning, GK, Stankovic, I, Vignatelli, L, Fanciulli, A, Calandra-Buonaura, G, Seppi, K, Palma, JA, Meissner, WG, Krismer, F, Berg, D, Cortelli, P, Freeman, R, Halliday, G, Höglinger, G, Lang, A, Ling, H, Litvan, I, Low, P, Miki, Y, Panicker, J, Pellecchia, MT, Quinn, N, Sakakibara, R, Stamelou, M, Tolosa, E, Tsuji, S, Warner, T, Poewe, W, and Kaufmann, H, *The Movement Disorder Society Criteria for the Diagnosis of Multiple System Atrophy.* Mov Disord, 2022. **37**(6): p. 1131-1148.
50. Xiang, J, Zhang, Z, and Ye, K, *A promising PET tracer candidate targeting α-synuclein inclusions.* Clin Transl Med, 2023. **13**(9): p. e1408.
51. Goedert, M, Jakes, R, Spillantini, MG, Hasegawa, M, Smith, MJ, and Crowther, RA, *Assembly of microtubule-associated protein tau into Alzheimer-like filaments induced by sulphated glycosaminoglycans.* Nature, 1996. **383**(6600): p. 550-3.
52. Whitwell, JL, Höglinger, GU, Antonini, A, Bordelon, Y, Boxer, AL, Colosimo, C, van Eimeren, T, Golbe, LI, Kassubek, J, Kurz, C, Litvan, I, Pantelyat, A, Rabinovici, G, Respondek, G, Rominger, A, Rowe, JB, Stamelou, M, Josephs, KA, and Group, ftMDS-ePS, *Radiological biomarkers for diagnosis in PSP: Where are we and where do we need to be?* 2017. **32**(7): p. 955-971.
53. Philippe, C, Haeusler, D, Mitterhauser, M, Ungersboeck, J, Viernstein, H, Dudczak, R, and Wadsak, W, *Optimization of the radiosynthesis of the Alzheimer tracer 2-(4-N-[11C]methylaminophenyl)-6-hydroxybenzothiazole ([11C]PIB).* Applied Radiation and Isotopes, 2011. **69**(9): p. 1212-1217.
54. Larsen, P, Ulin, J, Dahlstrøm, K, and Jensen, M, *Synthesis of [11C]iodomethane by iodination of [11C]methane.* Applied Radiation and Isotopes, 1997. **48**(2): p. 153-157.
55. Paxinos, G, Watson, CR, and Emson, PC, *AChE-stained horizontal sections of the rat brain in stereotaxic coordinates.* J Neurosci Methods, 1980. **3**(2): p. 129-49.

56. Ma, Y, Hof, PR, Grant, SC, Blackband, SJ, Bennett, R, Slatest, L, McGuigan, MD, and Benveniste, H, *A three-dimensional digital atlas database of the adult C57BL/6J mouse brain by magnetic resonance microscopy.* Neuroscience, 2005. **135**(4): p. 1203-15.
57. Mirrione, MM, Schiffer, WK, Fowler, JS, Alexoff, DL, Dewey, SL, and Tsirka, SE, *A novel approach for imaging brain-behavior relationships in mice reveals unexpected metabolic patterns during seizures in the absence of tissue plasminogen activator.* Neuroimage, 2007. **38**(1): p. 34-42.
58. Schiffer, WK, Mirrione, MM, Biegon, A, Alexoff, DL, Patel, V, and Dewey, SL, *Serial microPET measures of the metabolic reaction to a microdialysis probe implant.* J Neurosci Methods, 2006. **155**(2): p. 272-84.

Acknowledgements
We thank the technical assistants, Madhushree Pethe, Sophie Stotz and Marilena Poxleitner at the Werner Siemens Imaging Center (WSIC), University of Tuebingen for their support during experiments. We extend our appreciation to Anna Ohmayer, Gina Dunkel and the Weigelin group at the WSIC for their support with the fluorescence microscope. We further thank Prof. Dr. Tiago Fleming Outeiro from the University Medical Center Goettingen for providing us transgenic mice for the experiment.

This research project received funding from the European Union's Seventh Framework Programme (FP7/2007 2013, Multisyn) under REA grant agreement No. 602646, the European Union's Horizon 2020 Research and Innovative Programme under the Marie Skłodowska-Curie grant agreement No. 813528, the Michael J Fox Foundation for Parkinson's Research under grant No. MJFF16008, the Max Planck Society, and the Deutsche Forschungsgemeinschaft (DFG, German Research Foundation) under Germany's Excellence Strategy-EXC 2067/1-390729940.

Author contributions
R.S.S., S.H. – data acquisition and analysis, drafting of the manuscript

L.K., F.S., S.R., A.L., D.B., I.P., F.B., A.K.G. A.M.,– data acquisition and analysis, reviewed manuscript

B.J.P., C.G., A.G., K.H. - development and conceptual design, supervised experiments, drafting and reviewed manuscript

G.R. – optimization of radiochemical synthesis process to a GMP environment and optimization for human application, reviewed manuscript

C.M.S. - design, analysis, data interpretation, drafting macaque experiments

K.E.H. – design, supervision of macaque experiments, data interpretation, drafting macaque experiments and manuscript methods

V.C.R. – providing human post-mortem brain tissue, reviewed manuscript

B.R., K.B., T.G. – recruitment of the human patient, interpretation of clinical and imaging data, reviewed manuscript

C.L.F., M.R. – acquisition, analysis and interpretation of SPECT and PET clinical data, reviewed manuscirpt

B.D., P.K. – providing αSYN(A30P) and control mice, support with immunohistochemistry, reviewed manuscript

B.F., M.S. – providing electron microscopy support, reviewed manuscript

Competing interests
A patent has been filed (PCT/EP2020/082778) that includes MODAG-005.

Armin Giese, Felix Schmidt, Andrei Leonov and Sergey Ryazanov are employed by MODAG GmbH, which retains ownership of MODAG-005, Armin Giese and Christian Griesinger are shareholders of MODAG GmbH. The other authors declare no competing interests.

Inclusion and ethics

The questionnaire and methodology for this study were approved by the ethics committee of the Faculty of Medicine at the University of Tuebingen (Ethics approval number: 813/2018BO2).
All rodent experiments were conducted in compliance with the German animal protection law and with the approval of the local authorities (Regierungspräsidium Tübingen, R3/19G). Macaque experiments were conducted in compliance with all applicable sections of the Final Rules of the Animal Welfare Act regulations (Code of Federal Regulations, Title 9), the Public Health Service Policy on Humane Care and Use of Laboratory Animals from the Office of Laboratory Animal Welfare, and the Guide for the Care and Use of Laboratory Animals from the National Research Council (OLAW, current edition) (NRC, current edition).

All authors agree with the submitted version of the manuscript. The material submitted for publication has not been previously reported and is not under consideration for publication elsewhere.

Extended Data Figures

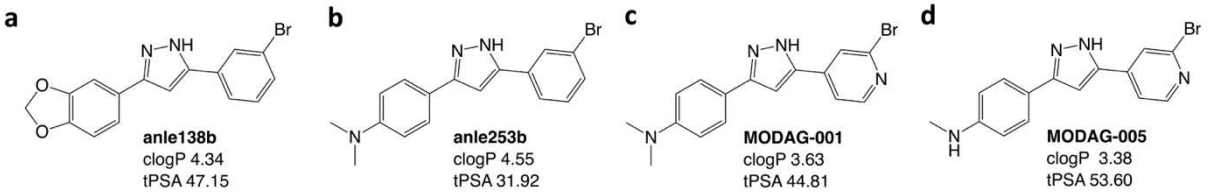

Extended Data Fig. 1: Chemical structures of anle138b (a), anle253b (b), MODAG-001 (c), and MODAG-005 (d) with their calculated logP and topological polar surface area [Å^2] values. clogP, calculated logP; tPSA, topological polar surface area.

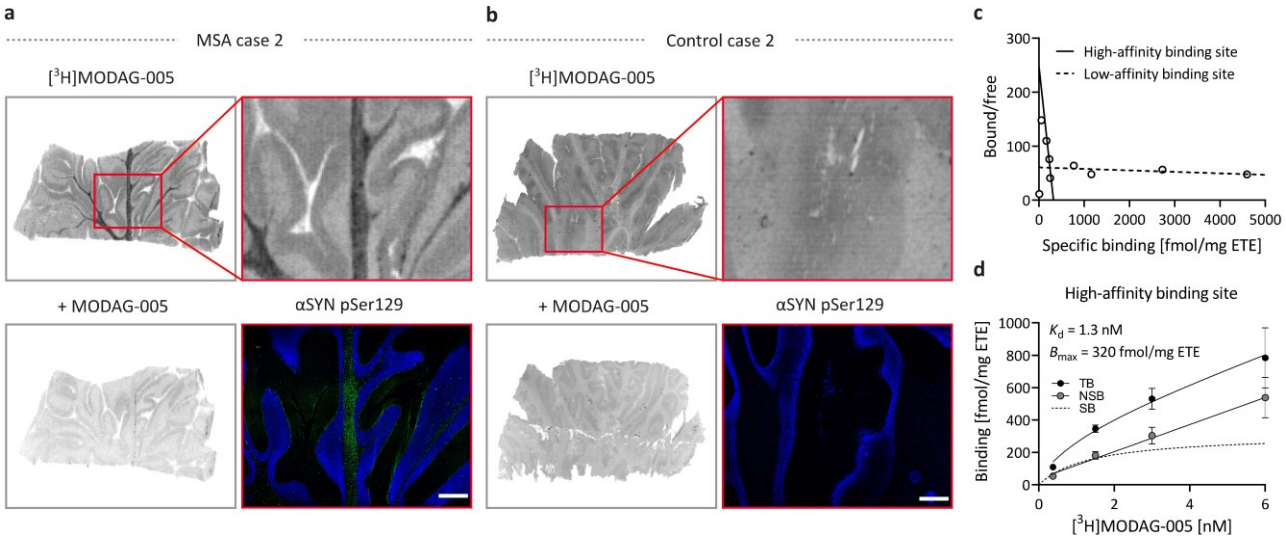

Extended Data Fig. 2: [^{3}H]MODAG-005 binding in MSA case 2 brain tissues. a, Autoradiographic images of total binding (3 nM) and after self-blocking (3 µM unlabeled MODAG-005) and immunofluorescence microscopy verification of pathology in post-mortem human cerebellar brain tissues of MSA case 2 and **b**, healthy control case 2. Red boxes show the total binding of autoradiography at higher magnification, with immunofluorescence microscopy images of αSYN pSer129 (green) and DAPI (blue). Scale bars,1 mm. **c** and **d**, A high-affinity binding site (K_d = 1.3 nM) remained after selegiline pre-blocking (3 µM for 1 hour) saturation binding autoradiography in MSA case 2 brain tissue (n = 1, repeated measurements in each sample). A K_d value of 364 nM was estimated for the low-affinity binding site (not shown). αSYN, α-synuclein; ETE, estimated tissue equivalent; MSA, multiple system atrophy; NSB, non-specific binding; SB, specific binding; TB, total binding. Data points in **d** are represented as mean ± s.d..

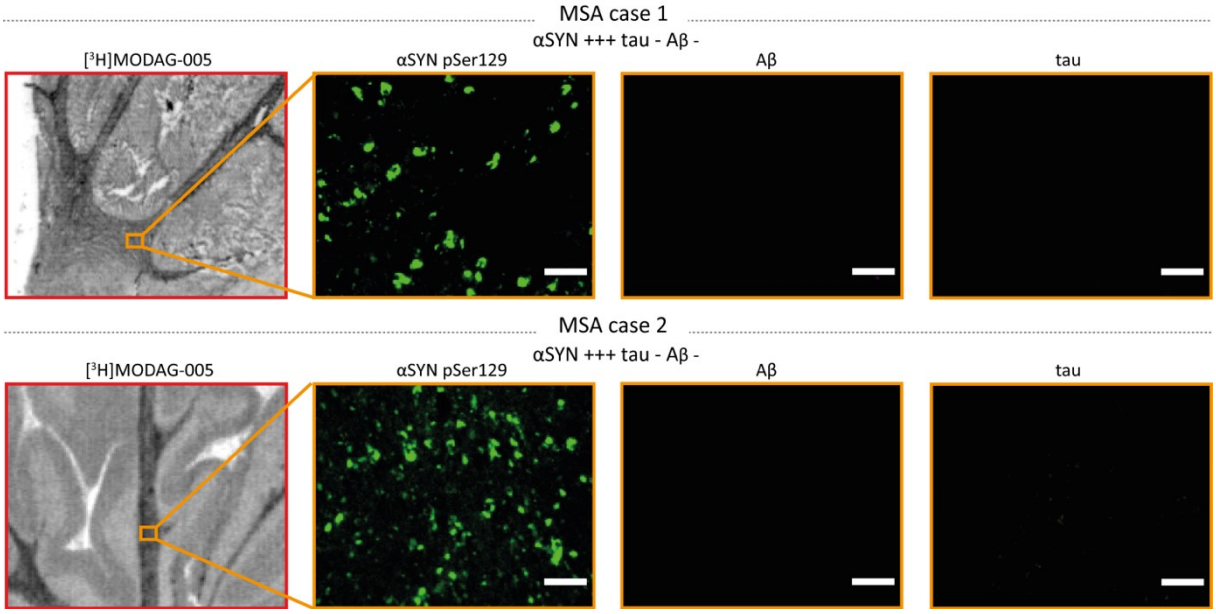

Extended Data Fig. 3: αSYN, Aβ and tau immunofluorescence microscopy on human MSA case 1 and 2 brain sections. αSYN pathology was confirmed using αSYN pSer129 staining (green). The absence of immunofluorescence microscopy for $A\beta_{1-42}$ and phosphorylated tau confirms tracer binding to αSYN in both MSA cases. The number of "+" symbols indicates an increasing degree of pathology; "-" symbolizes the absence of pathology. Scale bars, 50 µm. Aβ, β-amyloid; αSYN, α-synuclein; MSA, multiple system atrophy.

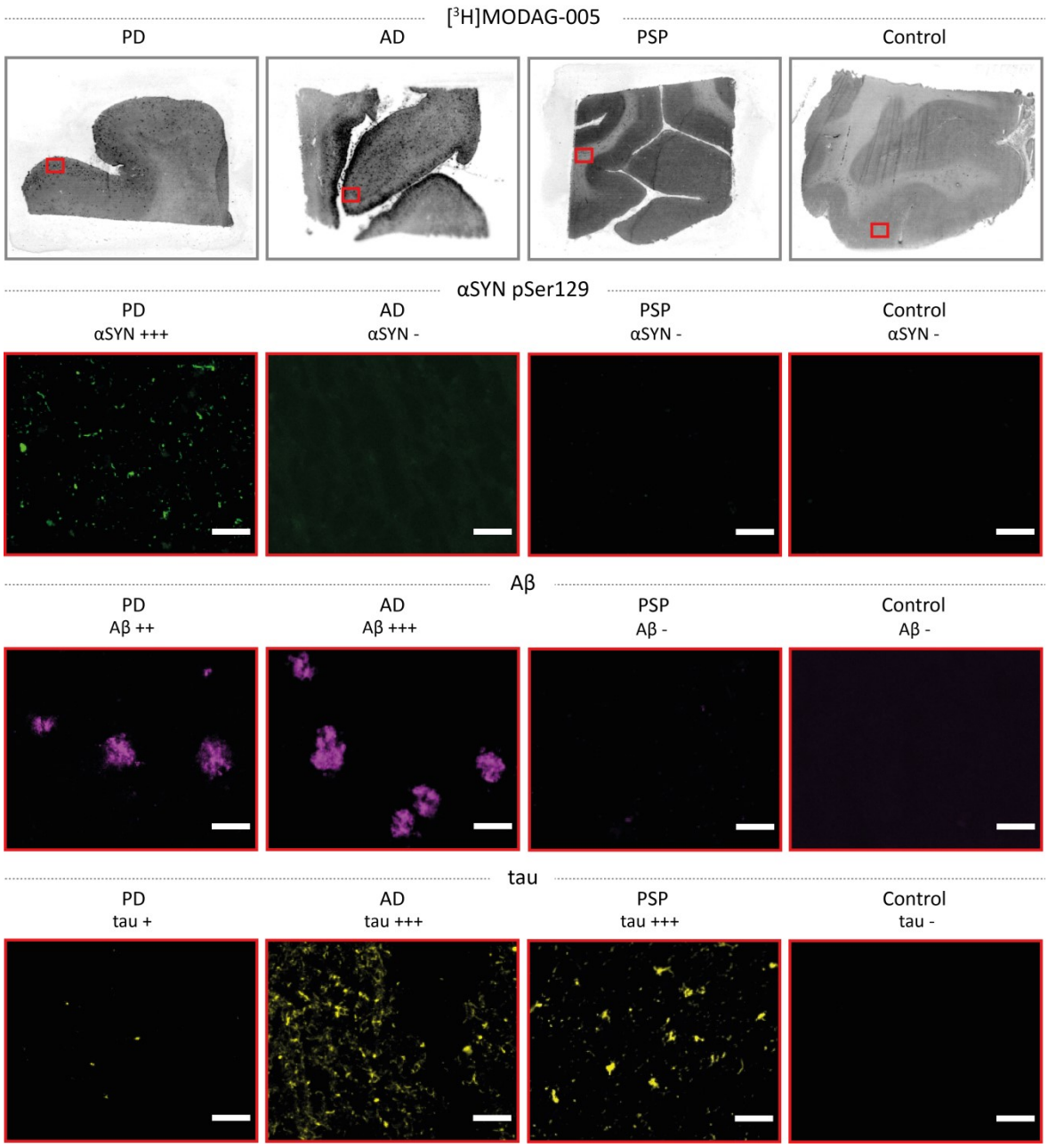

Extended Data Fig. 4: Confirmation of αSYN, Aβ and tau pathology on human brain sections using immunofluorescence microscopy. Antibodies against αSYN pSer129 (green), $Aβ_{1-42}$ (magenta) and phosphorylated tau (yellow) were used to verify the pathology. The number of "+" symbols indicates an increasing degree of pathology; "-" symbolizes the absence of pathology. Scale bars, 50 µm. AD, Alzheimer's disease; Aβ, β-amyloid; αSYN, α-synuclein; PD, Parkinson's disease; PSP, progressive supranuclear palsy.

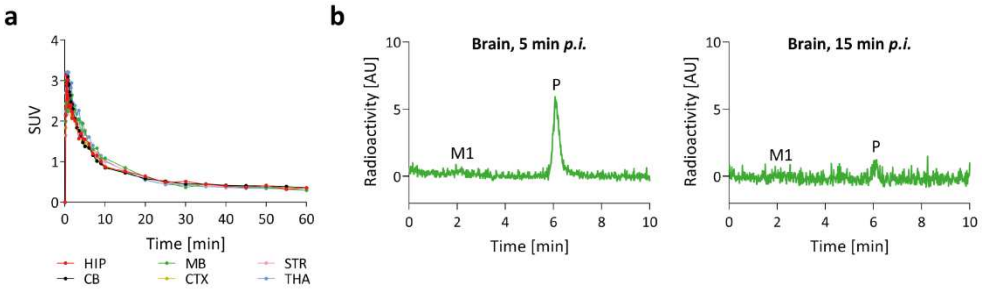

Extended Data Fig. 5: Pharmacokinetic and metabolic profile of [^{11}C]MODAG-005 in the rat brain. a, [^{11}C]MODAG-005 brain TACs show high uptake into the brain (max. SUV = 3.2) and fast clearance from the brain. **b**, Radio-metabolite analysis revealed one metabolite present in the brain with 91% and 64% of the parent compound remaining at five and 15 minutes post tracer injection, respectively. AU, arbitrary units; CB, cerebellum; CTX, cortex; HIP, hippocampus; MB, midbrain; M1, metabolite 1; P, parent compound; p.i., post injection; STR, striatum; SUV, standardized uptake value; THA, thalamus.

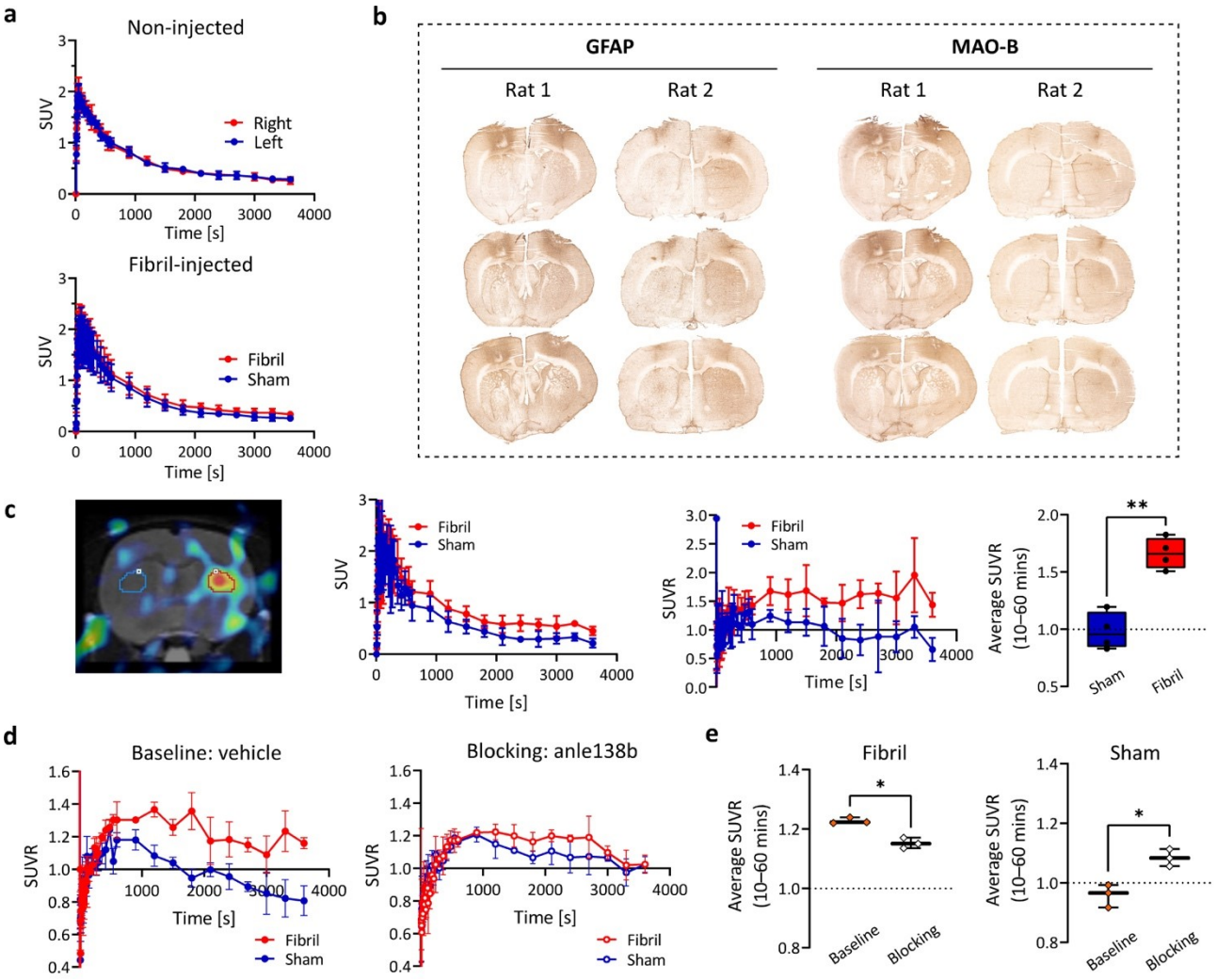

Extended Data Fig. 6: PET analysis of [^{11}C]MODAG-005 and immunohistochemistry assessment of GFAP and MAO-B expression in fibril-injected rats. a, TACs in the striatum of non-injected rats (n = 3) and fibril-injected rats (n = 4) are shown. A visible difference in [^{11}C]MODAG-005 retention between fibril-injected striatum and sham-injected striatum was detected, whereas no differences in the TACs between non-injected right and left striatum were observed. **b**, Immunohistochemistry of GFAP and MAO-B showed an increased astrogliosis and MAO-B expression in the fibril-injected striatum and, more prominently, along the injection trajectory in the cortex of both hemispheres (n = 2). **c**, PET analysis using VOI based on isocontour automatic detection set to 70%. An example PET/MR image is shown with VOI which were created surrounding the hotspot in the fibril-injected striatum (red) and subsequently mirror-reflected into the contralateral, sham-injected striatum (blue). TACs and time-SUVR curves as well as average SUVR with the cerebellum as the reference region revealed a higher tracer retention in the fibril-injected striatum compared to the non-injected striatum (average SUVR = 1.66 ± 0.137 vs. 0.98 ± 0.163, p = 0.0021). **d**, **e**, Fibril-injected rats underwent a baseline scan with vehicle administration and a blocking scan with anle138b administration. The cerebellum was used as the reference region for SUVR calculation. SUVR values over time showed a smaller difference between the fibril-injected and sham-injected striatum when blocked with anle138b. Average SUVR was decreased by anle138b blocking (from 1.23 ± 0.010 to 1.15 ± 0.018, p = 0.038) in the fibril-injected striatum, but increased in the sham-injected striatum (from 0.96 ± 0.038 to 1.08 ± 0.029, p = 0.019). GFAP, glial fibrillary acid protein; MAO-B, monoamine oxidase B; SUV, standardized uptake value; SUVR, standardized uptake value ratio; VOI, volume of interest. Data are presented as mean ± s.d.. Box plots extend from the 25th to 75th percentiles with the median indicated in the middle of the box and the minimum to maximum values shown by the whiskers. An unpaired two-tailed t-test was used in **c** and **e**. In **a** and **c**, n = 3 for non-injected rats and n = 4 for fibril-injected rats. In **d** and **e**, fibril-injected rats underwent both baseline and blocking scans (n = 3).

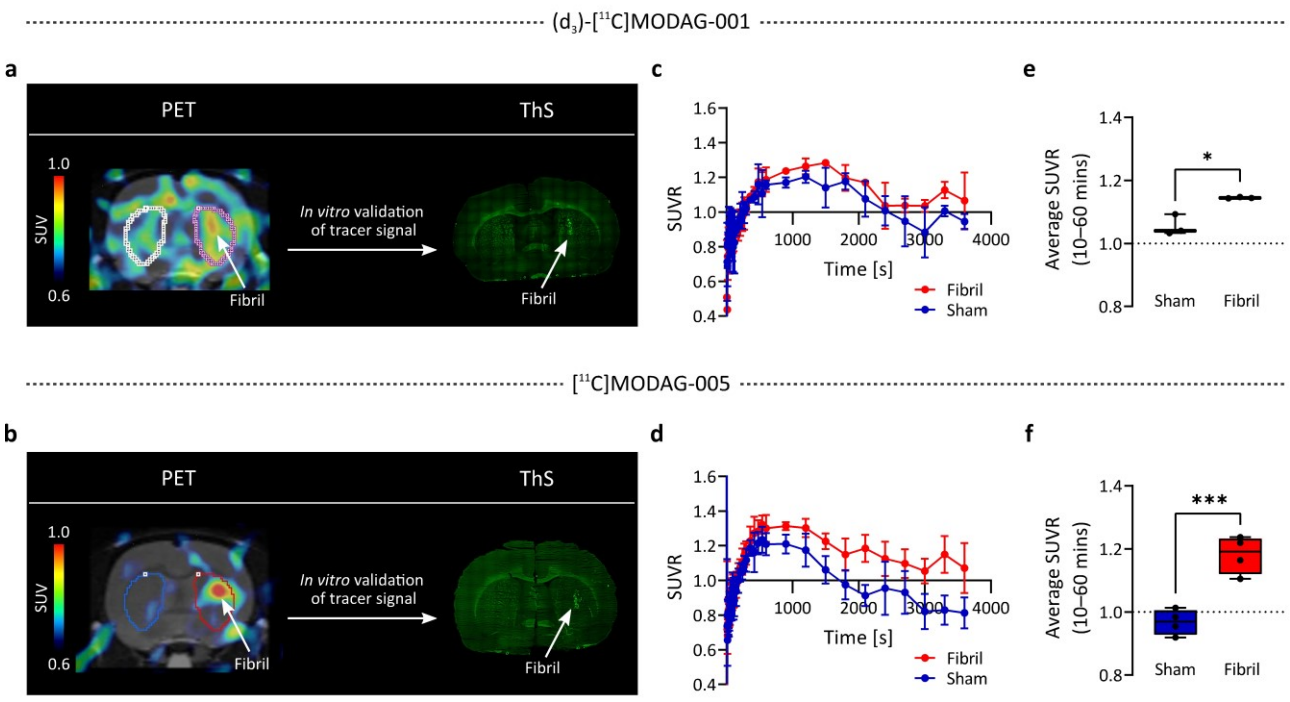

Extended Data Fig. 7: Comparison of (d_3)-[^{11}C]MODAG-001 and [^{11}C]MODAG-005 *in vivo*. **a**,**b**, (d_3)-[^{11}C]MODAG-001 and [^{11}C]MODAG-005 PET images (sum of 2.5 to 60 min) of exemplary αSYN fibril-injected rats four days post injection into the brain. **a-f**, Increased tracer binding was observed in the fibril-injected right striatum compared to the vehicle-injected left striatum for both tracers. **e**,**f**, An improved target-to-background ratio was observed for [^{11}C]MODAG-005 (1.18 ± 0.059 vs. 0.97 ± 0.041, p = 0.0003, n = 4) compared to (d_3)-[^{11}C]MODAG-001 (1.15 ± 0.002 vs. 1.06 ± 0.033, p = 0.0454, n = 3), via comparison of the average SUVR between the fibril-injected and sham-injected striatum. αSYN, α-synuclein; PET, positron emission tomography; SUV, standardized uptake value; SUVR, standardized uptake value ratio; ThS, thioflavin S. Data in **c**, **d**, **e** and **f** are represented as mean ± s.d.. In **e** and **f**, Shapiro-Wilk test indicated normal distribution and two-tailed paired t-tests were used for the comparisons.

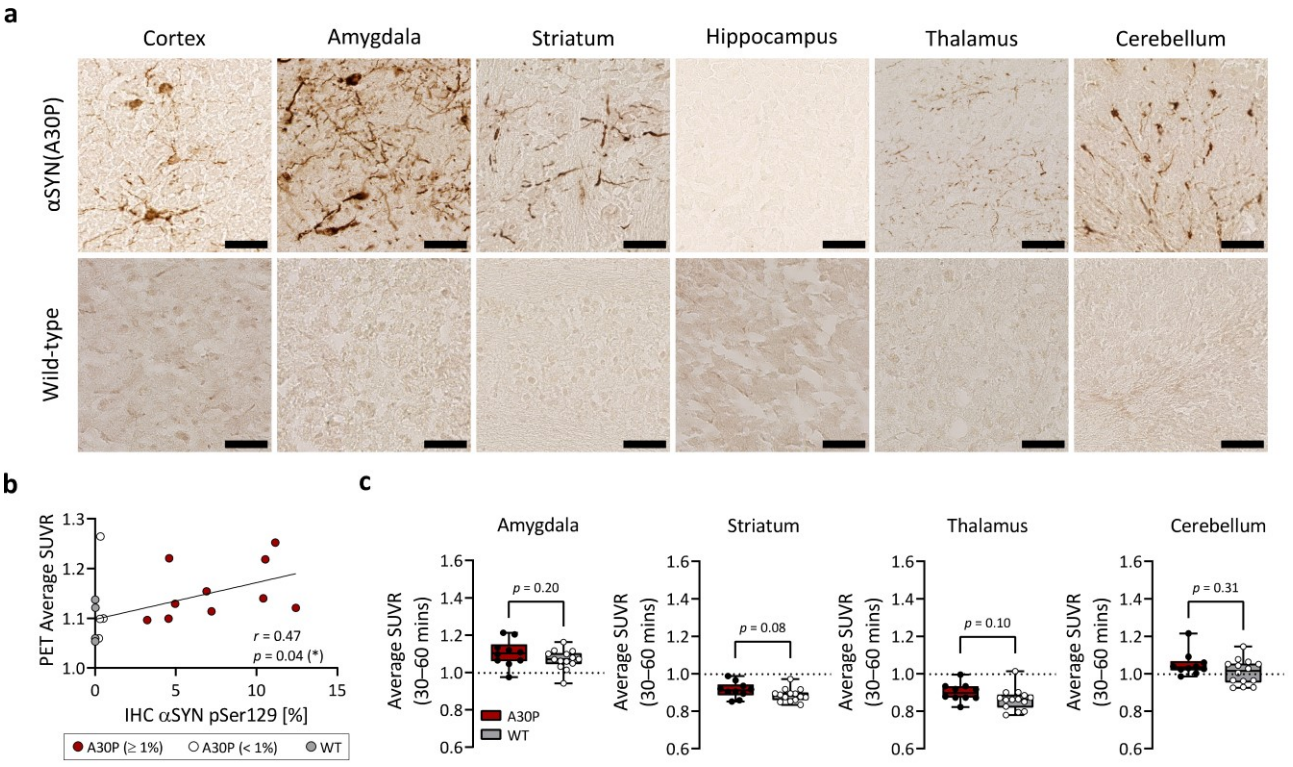

Extended Data Fig. 8: Evaluation of [^{11}C]MODAG-005 in the αSYN(A30P) transgenic mouse model and immunohistochemical validation. a, Immunohistochemistry of αSYN pS129 showed the presence of αSYN pathology in αSYN(A30P) mice in the cortex, amygdala, striatum, thalamus and cerebellum, but not in the hippocampus. No pathology was detected in wild-type mice. Scale bar, 50 µm. **b**, Data on the percentage of positive αSYN pSer129 immunohistochemistry (x-axis) in the brainstem of αSYN(A30P) mice revealed a large interindividual variation, ranging from 0.2% to 12.4%. Only αSYN(A30P) mice with ≥ 1% percentage of positive staining (red circles) were included in the main PET analysis, while αSYN(A30P) mice with < 1% (white circles) were excluded due to the lack of pathology. Wild-type mice (gray circles) showed no staining with a negligible positive signal in thresholded images (< 0.04%). Taking into account both groups, αSYN(A30P) mice (n = 14) and randomly selected wild-type mice (n = 5), a moderate positive correlation between αSYN pSer129 immunohistochemistry and [^{11}C]MODAG-005 PET binding in the brainstem was detected (r = 0.47, p = 0.043). **c**, Comparison of [^{11}C]MODAG-005 PET average SUVR calculated from 30 to 60 minutes showed no differences between the both groups in the amygdala (p = 0.20), striatum (p = 0.08), thalamus (p = 0.10) and cerebellum (p = 0.31). A30P, αSYN(A30P) mice; αSYN, α-synuclein; IHC, immunohistochemistry; PET, positron emission tomography; SUVR, standardized uptake value ratio; WT, wild-type mice. In **b**, data points are presented as the mean value of individual animals in immunohistochemistry pathology quantification from all A30P αSYN mice (n = 14, 6–10 tissue sections per animal) and randomly selected wild-type mice (n = 5, 2 tissue sections per animal). Only the wild-type mice with immunohistochemical quantification were included in the correlation analysis with PET imaging data. In **c**, box plots extend from the 25th to 75th percentiles with the median indicated in the middle of the box and the minimum to maximum values shown by the whiskers. Shapiro-Wilk test was used to test for normal distribution. An unpaired two-tailed t-test was performed to compare the average SUVR values between the two animal groups for all brain regions except in the cerebellum. Mann-Whitney test was performed for the cerebellum due to non-Gaussian distribution.

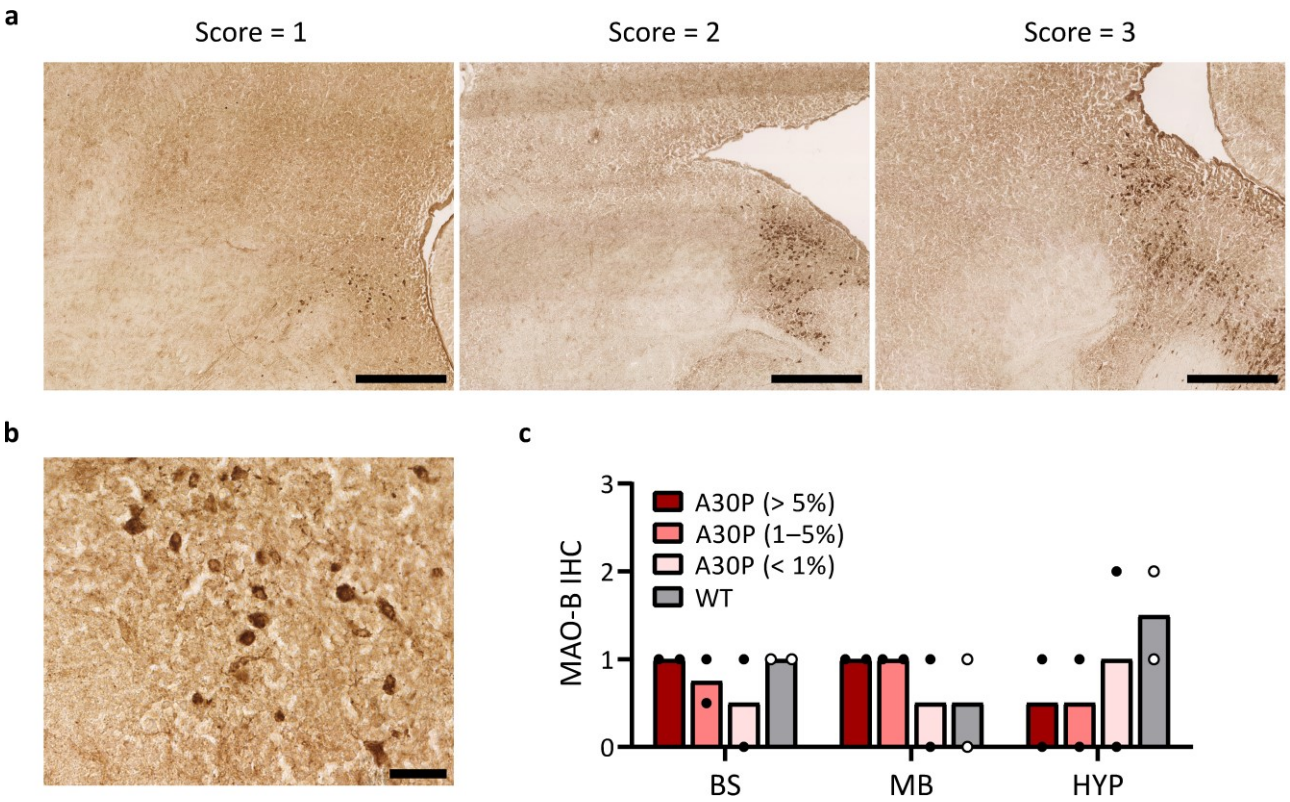

Extended Data Fig. 9: Immunohistochemistry analysis of MAO-B expression in αSYN(A30P) and wild-type mouse brain sections. αSYN(A30P) mice were assessed in three groups based on their αSYN pSer129 pathology load as determined previously (A30P > 5%, A30P = 1–5%, A30P < 1%). Qualitative scoring (score 0–3) was performed for the brainstem, midbrain and hypothalamus. **a**, Example of MAO-B immunohistochemistry images with their respective given score. Scale bar, 500 µm. **b**, MAO-B immunohistochemistry showed a staining diameter of approximately 10 µm. Scale bar, 50 µm. **c**, Analysis by qualitative scoring indicated a similar average scoring of MAO-B staining between score 0 to score 2 for all αSYN(A30P) and wild-type mouse groups (n = 2 per animal group, 4 tissue sections per animal). A30P, αSYN(A30P) mice; BS, brainstem; HYP, hypothalamus; IHC, immunohistochemistry; MB, midbrain.

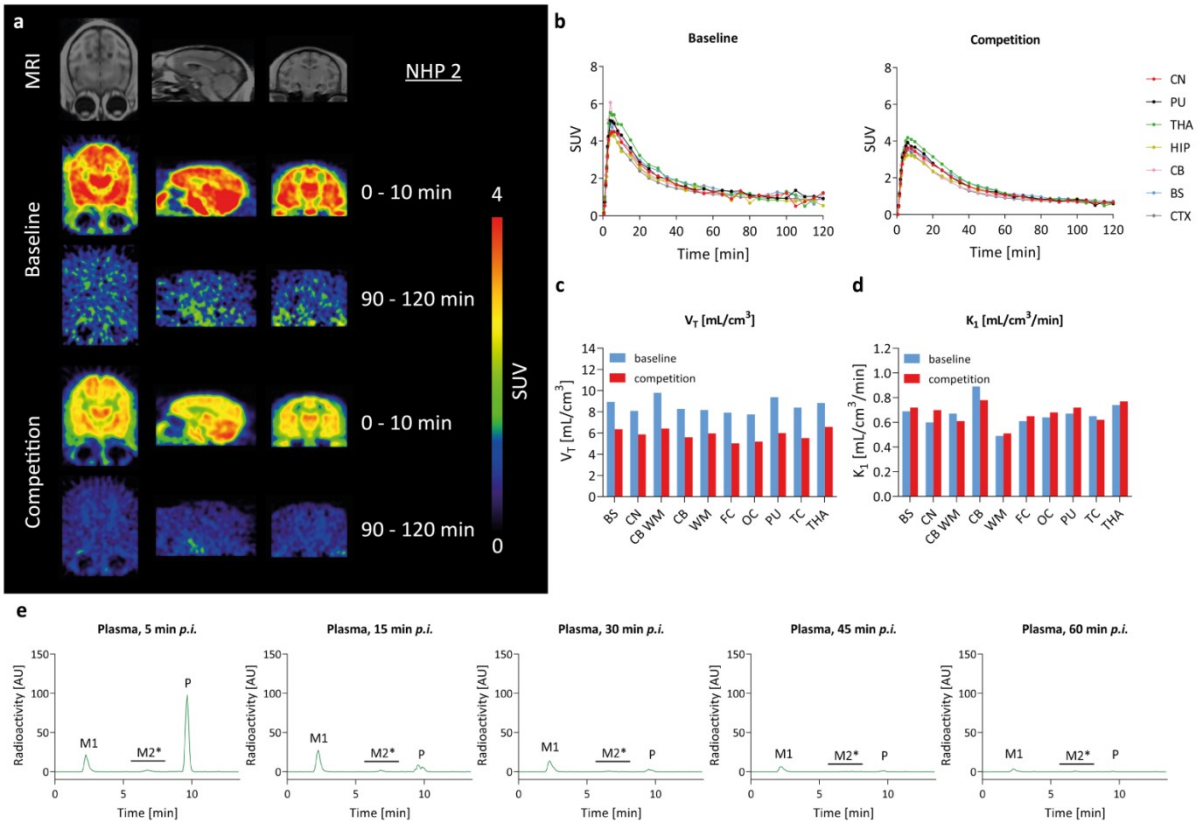

Extended Data Fig. 10: *In vivo* characterization of [^{11}C]MODAG-005 in non-human primates (NHPs). a, Transversal, sagittal and coronal (left to right) MRI of one exemplary cynomolgus monkey brain and [^{11}C]MODAG-005 PET images at baseline and after pre-injection of MODAG-005 (sum of frame 0 to 10 and 90 to 120 minutes). **b**, TACs of different brain regions show high brain uptake with peak SUVs of 6.1 (baseline) and 4.2 (competition) followed by a fast clearance from the brain. **c**,**d**, Volume of distribution (V_T) and K_1 values estimated from a 2-tissue-compartment model at baseline and after competition with MODAG-005. **e**, Plasma radio-metabolites revealed the formation of two metabolites, with 71%, 24%, 13%, 9% and 5% of the parent compound remaining at 5, 15, 30, 45, and 60 minutes post tracer injection, respectively. AU, arbitrary units; BS, brainstem; CB, cerebellum; CB WM, cerebellar white matter; CN, caudate nucleus; CTX, cortex; WM, white matter; FC, frontal cortex; HIP, hippocampus; MRI, magnetic resonance imaging; M1, metabolite 1; M2*, metabolite 2*; OC, occipital cortex; P, parent compound; PET, positron emission tomography; p.i., post injection; PU, putamen; STR, striatum; SUV, standardized uptake value; TACs, time-activity curves; TC, temporal cortex; 2-TCM, two tissue compartment model; THA, thalamus.

Extended Data Table 1: Overview of the human brain sections used in the autoradiography experiments and immunofluorescence microscopy validation.

Cases	Region	Age at death (years)	Sex	PMI (hour)	LBD (Braak)	AD (Braak & Braak)	AD (Thal)	Pathology		
								αSYN	Aβ	pTau
MSA1	CB	64	F	52	0	I	1	+++	-	-
MSA2	CB	54	M	71	0	0-I	0	+++	-	-
Control 1	CB	76	F	26	0	III	3	-	-	-
Control 2	CB	66	F	27-39	0	I	3	-	-	-
PD	FC	79	F	26	6	IV	3	+++	++	+
AD	FC	70	M	24	0	VI	5	-	+++	+++
PSP	FC	66	M	7	0	0	0	-	-	+++
Control 3	FC	64	F	39	0	0	0	-	-	-

The number of “+” symbols indicates an increasing degree of pathology in the particular region analyzed from low (+), moderate (++) to severe (+++) pathology; “-” symbolizes the absence of pathology. Aβ, β-

amyloid; αSYN, α-synuclein; AD, Alzheimer's disease; CB, cerebellum; Ctrl, control; F, female; FC, frontal cortex; LBD, Lewy body dementia; M, male; MSA, multiple system atrophy; PD, Parkinson's disease; PMI, post-mortem interval; PSP, progressive supranuclear palsy; pTau, phospho-Tau.

Extended Data Table 2: [^{11}C]MODAG-005 radio-metabolite quantification of brain and plasma samples at five and 15 minutes after injection in mice (n = 3 per time-point) and rats (n = 1 per time-point).

	M1 (t_R 2.0 min)		*M2* (t_R 3.9 min)*		*P (t_R 6.1 min)*	
Mice	***%***	***%ID/volume or weight***	***%***	***%ID/volume or weight***	***%***	***%ID/volume or weight***
Brain, 5 min	4.1 ± 1.1	0.5 ± 0.1$^{\#}$			96 ± 1.1	13 ± 6.0$^{\#}$
Brain, 15 min	21 ± 3.1	1.0 ± 0.2$^{\#}$			79 ± 3.1	4.3 ± 1.6$^{\#}$
Plasma, 5 min	40 ± 2.9	1.1 ± 0.4^{+}	32 ± 1.5	0.9 ± 0.4^{+}	29 ± 3.1	0.9 ± 0.4^{+}
Plasma, 15 min	44 ± 11	1.2 ± 0.4^{+}	33 ± 3.7	1.0 ± 0.4^{+}	22 ± 7.6	0.6 ± 0.2^{+}
Rats						
Brain, 5 min	9.0	0.3$^{\#}$			91	3.0$^{\#}$
Brain, 15 min	36	0.2$^{\#}$			64	0.3$^{\#}$
Plasma, 5 min	28	0.3^{+}	36	0.4^{+}	36	0.4^{+}
Plasma, 15 min	34	0.4^{+}	47	0.5^{+}	20	0.2^{+}

M1, metabolite 1; M2*, mixture of various metabolites; P, parent compound; t_R, retention time; %ID, % injected dose; $^{\#}$, per g brain tissue; $^{+}$, per plasma in one mL blood. Data are represented as mean ± s.d..

Extended Data Table 3: [^{11}C]MODAG-005 radio-metabolite quantification of plasma samples at 5, 15, 30, 45 and 60 minutes after injection in cynomolgus monkey (n = 2).

	M1 (t_R 2.3 min)	***M2* (t_R 6.6 min)***	***P (t_R 9.2 min)***
Cynomolgus monkey	***%***	***%***	***%***
Plasma, 5 min	19 ± 0.7	3.9 ± 1.0	74 ± 1.3
Plasma, 15 min	61 ± 1.6	6.9 ± 2.1	29 ± 0.3
Plasma, 30 min	70 ± 1.7	7.1 ± 0.9	18 ± 1.7
Plasma, 45 min	70 ± 1.4	7.5 ± 1.3	14 ± 1.0
Plasma, 60 min	67 ± 8.3	7.7 ± 3.2	8.6 ± 1.0

M1, metabolite 1; M2*, mixture of various metabolites; P, parent compound; t_R, retention time.

Supplementary Information

Supplementary Item 1

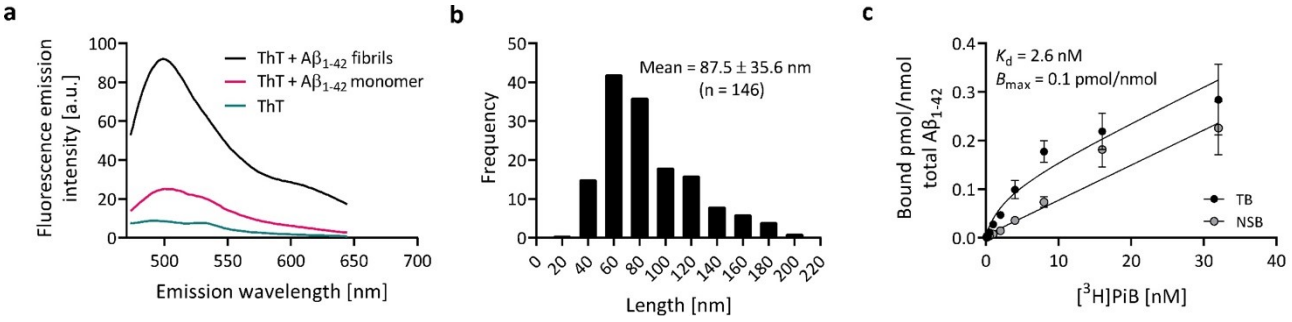

Characterization of Aβ$_{1-42}$ fibrils. a, Increase in ThT fluorescence emission spectrum in the presence of Aβ$_{1-42}$ fibrils compared to in the presence of monomers or ThT only. **b**, Length measurement and distribution of Aβ$_{1-42}$ fibrils were assessed from the negative stain electron microscopy images (mean length = 87.5 ± 35.6 nm). **c**, [^{3}H]PiB saturation binding assay confirmed good binding to Aβ$_{1-42}$ fibrils, with a K_d of 2.6 nM and a B_{max} of 0.1 pmol/nmol. Aβ$_{1-42}$, β-amyloid$_{1-42}$; NSB, non-specific binding; SB, specific binding; TB, total binding; ThT, thioflavin T. The points in **c** are presented as mean ± s.d..

Supplementary Item 2

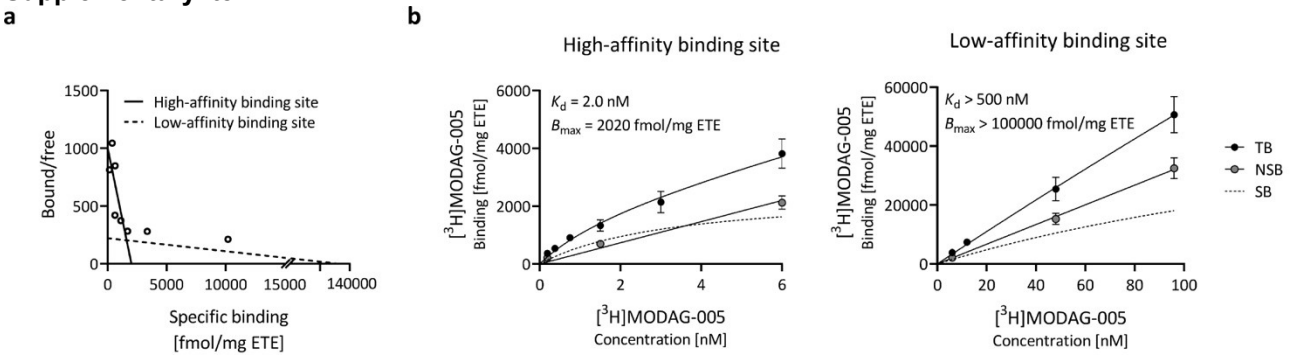

[^{3}H]MODAG-005 binding in AD brain tissue. Saturation binding autoradiography was performed in AD brain tissue (n = 1, repeated measurements in each sample). **a**, Scatchard plot revealed two binding sites in AD tissue. **b**, Saturation binding curves of high-affinity binding site and low-affinity binding site show K_d values of 2 nM and > 500 nM, respectively. ETE, estimated tissue equivalent; NSB, non-specific binding; SB, specific binding; TB, total binding. Data points in **b** are represented as mean ± s.d..

Supplementary Item 3

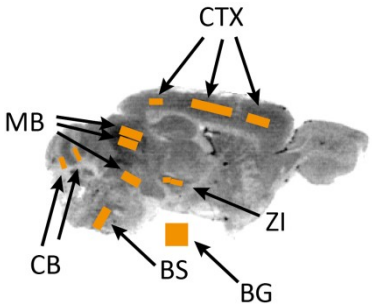

ROI definition for [^{3}H]MODAG-005 quantification in the αSYN(A30P) mouse model of PD. Abbreviations: BG, background; BS, brainstem; CB, cerebellum; CTX, cortex; MB, midbrain; ROI, region of interest; ZI, *zona incerta.*

Supplementary Item 4

^{11}C-labeling of MODAG 005

The radiolabeling of MODAG-005 was first approached by reductive methylation We observed the formation of [^{11}C]MODAG-005 with decay-corrected radiochemical yields of 12.0 ± 2.2% (from trapped MeI to formulated tracer) in a total synthesis time of 27.6 ± 0.9 minutes (from end of MeI trapping to end of

formulation) (**Fig. 6a**). The obtained A_m at the end of the synthesis was relatively low (49.2 ± 11.2 GBq/µmol). The synthesis thus required further optimization for successful imaging of low-abundant targets such as αSYN aggregates for *in vivo* studies.

To obtain a higher A_m, the radiosynthesis of [^{11}C]MODAG-005 was performed by direct methylation with [^{11}C]MeOTf. We achieved a decay-corrected radiochemical yield of 11.8 ± 2.7% (from trapped MeI to formulated tracer) and a A_m of 209 ± 44 GBq/*µ*mol. The radiolabeling of [^{11}C]MODAG-005 with higher A_m was used for follow-up rodent studies not presented in this study (method A).

For the *in vivo* studies in macaque, the direct methylation synthesis route, established in the Department of Preclinical Imaging and Radiopharmacy (Tuebingen, Germany), was adapted at Invicro-London and further adapted at Charles River. The direct methylation method B achieved a decay-corrected radiochemical yield of 3.7 ± 2.3% (from trapped MeI to formulated tracer) and a A_m of 89.3 ± 14 GBq/µmol.

Supplementary Item 5

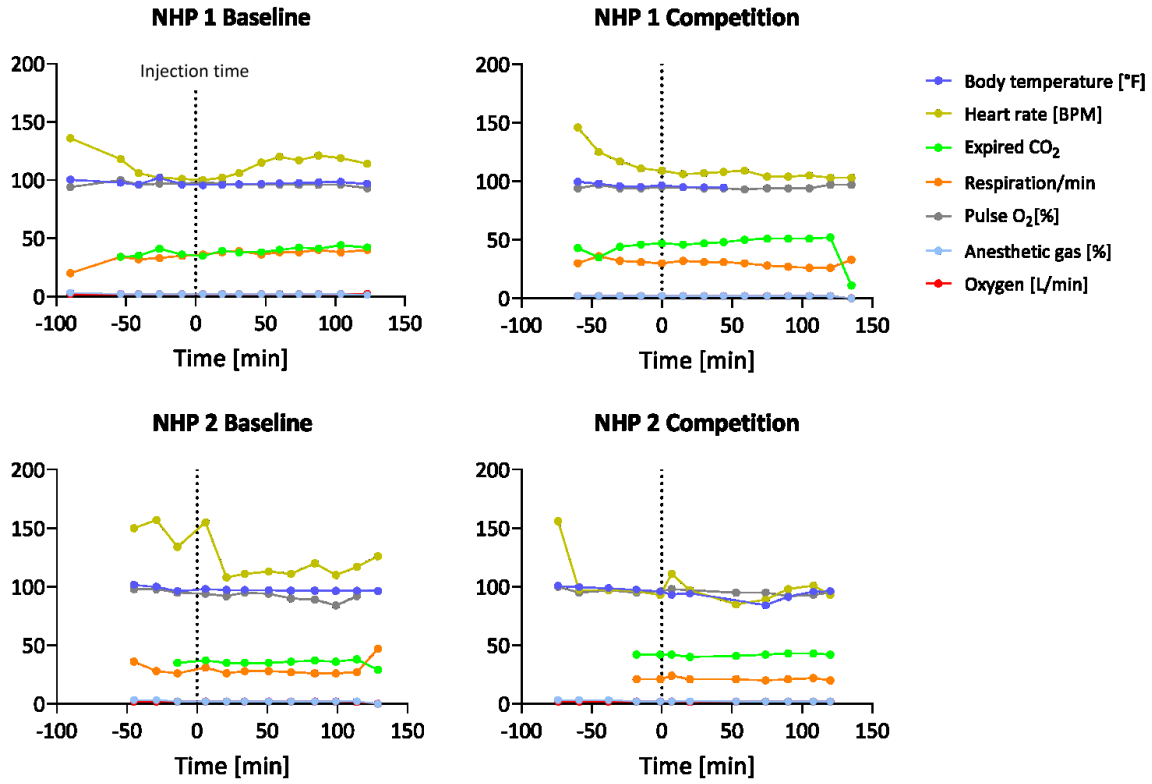

Macaque vitals. Monitoring of heart rate (BPM), body temperature (°F), expired CO_2, respiration/min, pulse O_2 (%), anesthetic gas (%), and oxygen (L/min) throughout the NHP PET scans.

Supplementary Item 6
Compound synthesis
All starting materials and solvents were of commercial grade and used as received unless noted otherwise. Thin layer chromatography (TLC): Macherey-Nagel precoated sheets, 0.25 mm ALUGRAM® SIL G/UV254 plates, detection with UV and/or by charring with 10% w/w ethanolic phosphomolybdic acid reagent followed by heating at 200°C. Flash column chromatography was performed by using Merck silica gel 60 (0.063-0.100 mm). Analytical HPLC was performed by using a Waters HPLC system with a Waters 996 Photodiode Array Detector. All separations involved a mobile phase of 0.1% trifluoroacetic acid (TFA) (v/v) in water and 0.1% TFA in acetonitrile. Unless otherwise specified, a gradient of 50% CH_3CN /50% H_2O → 100% CH_3CN in 30 minutes was used. HPLC was performed by using a reversed-phase (RP) column Eurospher RP 18, 100 Å, 5 µm, 250 × 4.6 mm at a flow rate of 1 mL/min. Electrospray ionization mass spectrometry (ESI-MS) and liquid chromatography/mass spectrometry (LC/MS) analyses were obtained by using a Waters Micromass ZQ 4000 mass spectrometer in conjunction with the Waters HPLC apparatus described above. NMR spectra were recorded by using a 400 MHz Bruker Avance spectrometer (Bruker AG, Rheinstetten, Germany) equipped with a TXI HCN z-gradient probe. All spectra were processed by using TOPSPIN 3.1 (Bruker AG, Karlsruhe, Germany). ^{1}H-NMR chemical shifts (δ) are reported in parts per million (ppm) relative to DMSO-d_5

as an internal standard. Data are reported as follows: chemical shift, multiplicity (s = singlet, bs = broad singlet, d = doublet, dd = doublet of doublets, ddd = doublet of doublet of doubletts), coupling constants (J, given in Hz), integration. ^{13}C-NMR chemical shifts (δ) are reported in parts per million (ppm) relative to DMSO-d_6 as an internal standard. The following experiments were used to record the resonances of the compounds: ^{1}H-1D, ^{13}C-1D-NMR spectra and ^{13}C-APT (attached proton test with a single J-evolution time of 1/145 seconds, spectra are processed such that quaternary and methylene groups have positive sign and methyl and methine groups negative sign). To resolve the overlap of resonances and recover undetectable resonances in ^{1}H and APT spectra, 2D-[^{13}C,^{1}H]-HSQC (heteronuclear single quantum coherence), 2D-[^{13}C, ^{1}H]-HMBC (heteronuclear multiple bond correlation) and 2D-NOESY were recorded for some compounds. The synthesis of the precursor anle190214 is depicted in the following figure.

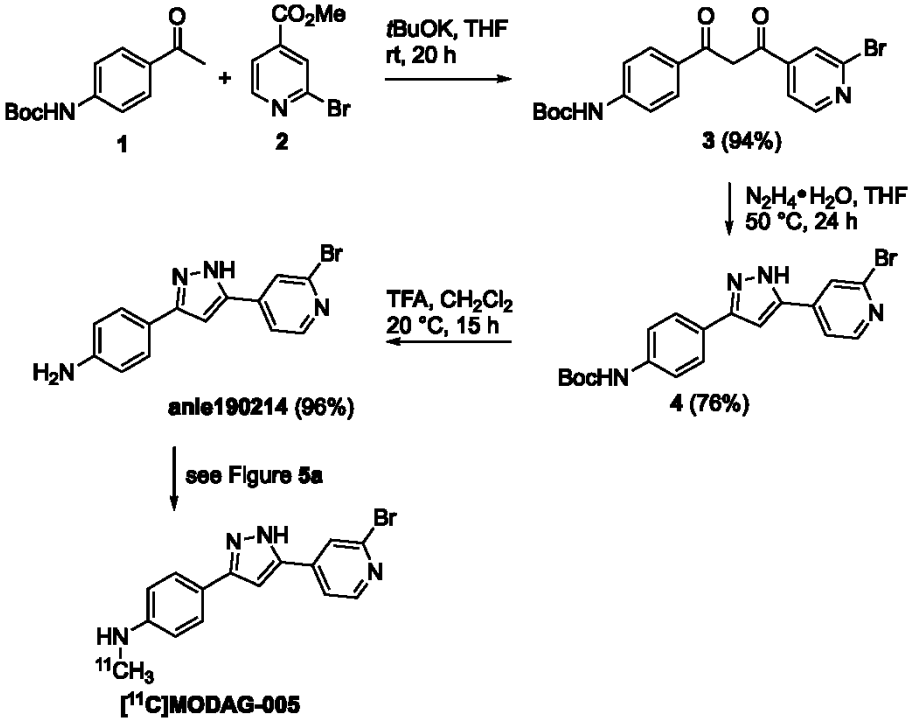

Experimental procedures and characterization data of compounds

MODAG-005: 4-[5-(2-Bromopyridin-4-yl)-1*H*-pyrazol-3-yl]-*N*-methylaniline was synthesized as described previously [12].

tert-Butyl {4-[3-(2-bromopyridin-4-yl)-3-oxopropanoyl]phenyl}carbamate **3**
A solution of potassium *tert*-butoxide (FW 112.21, 583 mg, 5.2 mmol) in THF (10.4 mL) was added to a stirred solution of *tert*-butyl *N*-(4-acetylphenyl)carbamate **1** (FW 235.28, 941 mg, 4 mmol) and methyl 2-bromopyridine-4-carboxylate **2** (FW 216.03, 1.04 g, 4.8 mmol) in THF (15 mL). The reaction mixture was stirred for 20 h. A 10 µL aliquot was sampled, quenched with 1M phosphate buffer pH 7, extracted with EtOAc and analyzed by TLC and LC-MS. About 95% conversion of ketone was observed. The mixture was poured into 1M phosphate buffer pH 7 (15 mL) and ice water (15 mL), and stirred at 0°C for 30 min. The resulting yellow solid was filtered off, washed with water (3 × 10 mL) and air dried to give 1.57 g (3.74 mmol, 94%) of crude product, which was used for the next step w/o purification. LC-MS: sample 0.5 mg/mL in CH_3CN; 10 µL injection volume; column: Eurospher RP18 100 Å, 5µm, 250 × 4.6 mm, solvents: water (+0.1% TFA, A) and CH_3CN (+0.1% TFA, B), gradient: B 50% → 100% in 30 min, detector UV 260 nm, peak RT 22.9 min, mass 419.2 (100%), 421.2 (98%), $[M+H]^+$). TLC (SiO_2, *n*-hexane:EtOAc = 2:1), R_f = 0.7.

tert-Butyl {4-[5-(2-bromopyridin-4-yl)-1*H*-pyrazol-3-yl]phenyl}carbamate **4**
To a solution of the *tert*-butyl {4-[3-(2-bromopyridin-4-yl)-3-oxopropanoyl]phenyl}carbamate **3** (1.57 g, 3.74 mmol) in THF (20 mL) was added hydrazine monohydrate (388 µL, 400 mg, 8 mmol). After being stirred at 50°C for 24 h the reaction mixture was cooled to room temperature and concentrated under reduced pressure. A mixture *n*-hexane/EtOAc = 2/1 (16 mL) was added, the mixture was stored 2 h at room temperature, then 15 h at 4°C. The resulting solid was filtered off, washed with *n*-hexane and vacuum dried. The crude product was purified by flash chromatography on silica gel (*n*-hexane/EtOAc = 1/1) to afford 1.18 g (2.84 mmol, 76%) of title product as beige solid. ^{1}H NMR (400 MHz, DMSO-d6, two rotamers, main form) δ

= 13.63 (bs, 1H), 9.53 (s, 1H), 8.41 (d, *J* = 5.1 Hz, 1H), 8.02 (s, 1H), 7.86 (d, *J* = 5.1, Hz, 1H), 7.69 (d, *J* = 8.6 Hz, 2H), 7.57 (d, *J* = 8.6 Hz, 2H), 7.35 (s, 1H), 1.49 (s, 9H). ^{13}C NMR (100.6 MHz, DMSO-d6, two rotamers, main form) δ = 152.8, 150.9, 147.6, 144.2, 142.3, 139.2 (2C), 125.8 (2C), 123.2, 122.6, 119.2, 118.4 (2C),100.6, 79.4, 28.2 (3C). LC MS (RP18-100 Å, gradient 50% CH_3CN /50% H_2O → 100% CH_3CN in 30 min), RT 14.6 min and mass 415.3 (100%), 417.3 (98%), $[M+H]^+$. TLC (SiO_2, *n*-hexane/EtOAc = 1/1) R_f 0.56, m.p.: 230-235°C (dec).

4-[5-(2-bromopyridin-4-yl)-1*H*-pyrazol-3-yl]aniline **anle190214**
To a suspension of *tert*-butyl {4-[5-(2-bromopyridin-4-yl)-1*H*-pyrazol-3-yl]phenyl}carbamate **4** (FW 415.28, 1.18 g, 2.84 mmol) in CH_2Cl_2 (21 mL) trifluoroacetic acid (2.8 mL, 4.14 g, 36.4 mmol) was added. The mixture was stirred at room temperature for 15 h and concentrated in vacuum. 1M phosphate buffer pH 7 (20 mL) was added, the resulting precipitate was filtered off, washed with water (2×10 mL) and air dried to give 859 mg (2.73 mmol, 96%) of product as a yellow-orange colored solid. ^{1}H NMR (400 MHz, DMSO-d6) δ = 13.22 (bs, 1H), 8.39 (d, *J* = 5.2 Hz, 1H), 8.01 (d, *J* = 0.8 Hz, 1H), 7.83 (dd, *J* = 5.2, 1.4 Hz, 1H), 7.47 (ddd, *J* = 7.5, 1.7, 0.9 Hz, 2H), 7.19 (s, 1H), 6.64 (ddd, *J* = 7.5, 1.7, 0.9 Hz, 2H), 5.49 (bs, 2H). ^{13}C NMR (100.6 MHz, DMSO-d6) δ = 150.8, 149.2, 146.4, 146.1, 143.8, 142.2, 126.3 (2C), 123.0, 119.0, 116.8, 113.9 (2C), 99.2. LC MS (RP18-100Å, gradient 0% CH_3CN /100% H_2O → 100% CH_3CN in 30 min), RT 14.8 min and mass 315.2 (98%), 317.2 (100%), $[M+H]^+$. TLC (SiO_2, *n*-hexane/EtOAc = 1/1) R_f 0.25, m.p.: >300°C.

Supplementary Item 7
Radiosynthesis by direct methylation - method B
$[^{11}C]CO_2$ was produced via a $^{14}N[p,\alpha]^{11}C$ nuclear reaction on a Siemens RDS-111 cyclotron, using 1% O_2 in N_2 as the target gas, using a Havar HP target.

No carrier-added $[^{11}C]CO_2$ was delivered to Tracerlab FX_2MeI (GE Healthcare) and $[^{11}C]MeI$ was produced *via* the phase-gas conversion pathway [54]. $[^{11}C]MeI$ passed through a silver triflate column, packed with a mixture of silver triflate and Carbosphere, at 200°C to generate $[^{11}C]MeOTf$, which bubbled into a reactor vessel pre-charged with a solution of anle190214 (2–3 mg) in anhydrous acetone (500 µL) held at -20°C. Radiosynthesis, purification and formulation were automated on EZ Modular Lab radiochemical synthesizers (Eckert & Ziegler GmbH).

The reaction mixture was heated to 50°C for three minutes, and then diluted with 1.7 mL of the preparative HPLC eluent. $[^{11}C]$MODAG-005 was purified by semi-preparative HPLC on an Agilent SB-phenyl column (5 µm, 9.4 × 250 mm) with 55% of 95/5 of acetonitrile/H_2O and 45% 50 mM aqueous ammonium acetate solution at a flow rate of 8 mL/min, which was eluted at seven minutes. The quality control of a dose solution was performed with an analytical HPLC on an Agilent SB-phenyl column (5 µm, 4.6 × 150 mm) with acetonitrile/50 mM aq. ammonium acetate (45/55) at a flow rate of 1.5 mL/min $[^{11}C]$MODAG-005 was eluted at 4.3 minutes, which was confirmed by co-injection of a MODAG-005 standard solution, and the radiochemical purity of a dose solution was >98%. At the end of the synthesis the radiochemical yield (decay-corrected) was 3.7 ± 2.3% and the molar activity (A_m) was 89.3 ± 14 GBq/μmol (End of synthesis).

Supplementary item 8

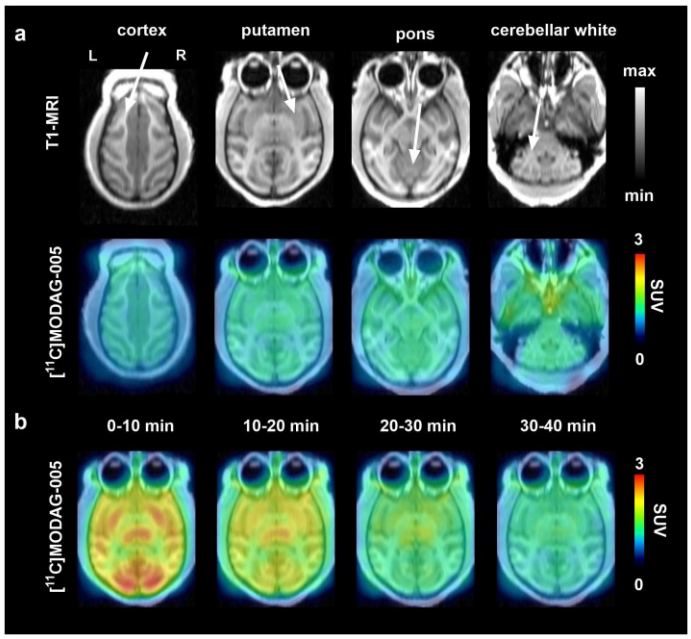

[^{11}C]MODAG-005 pharmacokinetic profile in the non-human primate brain. a, T1-weigthed MR images of a healthy cymologous monkey and corresponding [^{11}C]MODAG-005 PET images (sum of all frames) illustrating homogeneous tracer distribution in all brain regions. **b**, The pharmacokinetic profile of [^{11}C]MODAG-005 in a representative slice demonstrates fast tracer clearence and no tracer retention in any brain regions. MRI, magnetic resonance imaging; SUV, standardized uptake value (normalized to body weight).

References

1. Kuebler, L., *et al*., [^{11}C]MODAG-001-towards a PET tracer targeting alpha-synuclein aggregates. *Eur. J. Nucl. Med. Mol. Imaging*, 2020.
2. Larsen, P., Ulin, J., Dahlstrom, K. and Jensen, M., Synthesis of [11C]iodomethane by iodination of [11C]methane. *Appl. Radiat. Isot.*, 1997. **48**(2): p. 153-157.